

**NEUTRAL AND CATIONIC MAIN GROUP LEWIS ACIDS - SYNTHESIS,
ANION COMPLEXATION AND REDOX PROPERTIES**

A Dissertation

by

CHRISTOPHER LANE DORSEY

Submitted to the Office of Graduate Studies of
Texas A&M University
in partial fulfillment of the requirements for the degree of

DOCTOR OF PHILOSOPHY

May 2009

Major Subject: Chemistry

**NEUTRAL AND CATIONIC MAIN GROUP LEWIS ACIDS - SYNTHESIS,
ANION COMPLEXATION AND REDOX PROPERTIES**

A Dissertation

by

CHRISTOPHER LANE DORSEY

Submitted to the Office of Graduate Studies of
Texas A&M University
in partial fulfillment of the requirements for the degree of

DOCTOR OF PHILOSOPHY

Approved by:

Chair of Committee,
Committee Members,

Head of Department,

François P. Gabbaï
Marcetta Y. Darensbourg
David E. Bergbreiter
Jean-Philippe Pellois
David H. Russell

May 2009

Major Subject: Chemistry

ABSTRACT

Neutral and Cationic Main Group Lewis Acids - Synthesis, Anion Complexation and Redox Properties. (May 2009)

Christopher Lane Dorsey, B.S., Texas Lutheran University

Chair of Advisory Committee: Dr. François P. Gabbaï

The primary goal of this research concerns the synthesis and characterization of hybrid main group Lewis acids. Initially, the focus of this work was on the synthesis of derivatives possessing unusual bonding interactions enforced by a rigid 1,8-naphthalenediyl scaffold. After discovering a route to a new dilithio reagent, silicon based derivatives featuring $R_3Si-F \rightarrow CR_3^+$ and $R_3C-H \rightarrow SiFR_3$ interactions of 2.703(2) and 2.32(2) Å respectively were successfully synthesized and fully characterized. Another hybrid Lewis acid based on the 1,8-naphthalenediyl scaffold that was studied was a trinuclear B_2/Hg Lewis acid. This molecule has been shown to bind two fluoride anions sequentially, and the binding events can be followed by differential pulsed voltammetry.

The final part of this work concerns the reactivity and redox behavior of main group systems. It has been shown that the *p*-phenylene linker in 4-dimesitylboryl-1-diarylmethylbenzenes effectively reduces electrochemical communication between the carbocation and borane moieties when compared to systems without the linker. Reduction of these species produces a derivative whose EPR signal is only slightly influenced by the ^{11}B center. These findings have been further substantiated by theoretical calculations. Finally, the redox properties of α -phosphonio- and α -

phosphonyl-carbocations have been studied. Chemical reduction of both species leads to a predominately carbon centered radical with coupling to the ^{31}P center of 18 and 19.7 G respectively. The α -phosphonio carbocations, however, also undergo ligand exchange reactions with pyridine derivatives suggesting that these species can also be referred to as ligand stabilized carbocations.

DEDICATION

For my parents

ACKNOWLEDGMENTS

I would first like to thank my undergraduate research advisors Dr. W. Preston Reeves and Dr. David A. Wasmund for their constant encouragement and nagging during my undergraduate career which profoundly influenced my decision to pursue graduate studies. I will never forget the advice and knowledge that they conveyed to me regarding both chemistry and life. I would also like to acknowledge Dr. Marcetta Y. Darensbourg, Dr. David E. Bergbreiter and Dr. Jean-Philippe Pellois for sitting on my committee.

There are not enough words to describe how helpful the Gabbai research group has been in completing my Ph.D. In particular, I would like to thank Dr. Todd Hudnall and Casey Wade who spent numerous hours discussing ideas and whose friendship and support throughout the past five years will always be remembered and valued. I would also like to thank Dr. Mohand A. Melaimi and Dr. Huadong Wang for their guidance during my first year as a graduate student; and the entire Gabbai group: Dr. Ching-Wen Chiu, Dr. Mieock Kim, Youngmin Kim, Dr. Min Hyung Lee, Dr. Thomas Taylor, Dr. Charlotte Burress, Dr. Takeshi Matsumoto, Dr. Chammi Gamage, Haiyan Zhao, Tzu-Pin Lin, Iou-Sheng Ke, Pawel Jewula, Dan Gardner Bryan Carroll, Sirinan Kulchat and James Bondi.

To my parents Tommy and Patricia, your undying love, support and encouragement over the past twenty seven years has been truly appreciated, and there is no way I could ever repay you for everything you have sacrificed to get me to this point in my life.

I would like to acknowledge the NSF, the Welch Foundation, the U.S. Army Institute for Chemical Defense for research funding, the Department of Chemistry and Office of Graduate Studies for travel grants.

Finally, I would like to thank my research advisor, Professor François P. Gabbaï for his guidance and the countless hours spent discussing my research. I can not thank you enough for giving me the opportunity to work in your research lab, and the enthusiasm with which you approach chemistry will forever influence my career.

TABLE OF CONTENTS

	Page
ABSTRACT	iii
DEDICATION	v
ACKNOWLEDGMENTS.....	vi
TABLE OF CONTENTS	viii
LIST OF FIGURES.....	xi
LIST OF TABLES	xxiv
 CHAPTER	
I INTRODUCTION AND RESEARCH OBJECTIVES.....	1
1.1 Overview	1
1.2 Synthesis of compounds displaying unusual bonding.....	1
1.2.1 Introduction	1
1.2.2 Objectives.....	4
1.3 Synthesis and redox properties of borata-alkenes	6
1.3.1 Introduction	6
1.3.2 Objective	8
1.4 Synthesis of phosphorus containing radicals	9
1.4.1 Introduction	9
1.4.2 Objectives.....	10
II A $R_3C-H \rightarrow SiFR_3$ AGOSTIC INTERACTION.....	12
2.1 Background	12
2.1.1 C-X \rightarrow C bridged cations	12
2.1.2 Bridged disilanes	14
2.1.3 Bridged hybrid Lewis acids.....	19
2.2 Introduction	21
2.3 Synthesis, structure and properties of mercury derivatives.....	21
2.4 Synthesis, structure and properties of silicon derivatives	33
2.5 Conclusions	53
2.6 Experimental	53
III SYNTHESIS AND REDOX PROPERTIES OF BORATA-ALKENES	60
3.1 Background	60

CHAPTER	Page
3.1.1 Carbon centered radicals	60
3.1.2 Triarylboryl radicals	61
3.1.3 Alkenyl radicals.....	63
3.1.4 Borata-alkenes and their radicals	64
3.2 Synthesis and structure.....	66
3.3 Electrochemistry.....	71
3.4 Other extended radical systems.....	77
3.5 Conclusion.....	82
3.6 Experimental	82
IV SYNTHESIS AND REDOX PROPERTIES OF α -PHOSPHONIO- AND α -PHOSPHONYL-CARBOCATIONS	85
4.1 Background	85
4.1.1 Phosphorus ylids	85
4.1.2 Imminium and Imidizolium phosphonium species	87
4.1.3 α -phosphoryl radicals	88
4.1.4 Reduction of 9,9-bipyridinium derivatives	89
4.2 Synthesis and structure.....	91
4.3 Electrochemistry.....	105
4.4 Synthesis and structure of α -phosphonyl-carbocations.....	107
4.5 Electrochemistry of α -phosphonyl-carbocations.....	110
4.6 Conclusions	111
4.7 Experimental	112
V FLUORIDE ION COMPLEXATION BY A B ₂ /Hg HETERONUCLEAR TRIDENTATE LEWIS ACID	116
5.1 Background	116
5.1.1 Diboranes as anion complexation agents	116
5.1.2 Diboranes for the selective binding of fluoride.....	118
5.1.3 Hybrid boron/mercury systems for selective fluoride binding.....	119
5.2 Introduction	121
5.3 Synthesis and spectroscopic characterization	122
5.4 Structure of 70.....	123
5.5 Calculations.....	126
5.6 Electrochemistry.....	127
5.7 Fluoride anion binding	129
5.8 Comparative studies	133
5.9 Conclusion.....	141
5.10 Experimental	142

CHAPTER	Page
VI SUMMARY	146
6.1 Synthesis of compounds displaying unusual bonding.....	146
6.2 Fluoride anion complexation by a B ₂ /Hg heteronuclear tridentate Lewis acid	148
6.3 Synthesis and redox properties of borata-alkenes	149
6.4 Synthesis and redox properties of α -phosponio and α - phosphonyl carbocations	150
6.5 Conclusion.....	153
REFERENCES.....	154
VITA	161

LIST OF FIGURES

		Page
Figure 1.	Anion chelate complexes formed by 1,8-diborylnaphthalenes.	1
Figure 2.	Structure of the fluoride adduct of the 1,8-bis(diphenylmethylium)naphthalenediyl dication showing the unsymmetrical C-F→C bridge.	2
Figure 3.	Structures of the hydride adducts of 1,8-bis(diarylmethylium)naphthalenediyl dications showing the unsymmetrical C-H→C bridges.	3
Figure 4.	General bridging interactions in silanes.	3
Figure 5.	Synthesis of 1.	4
Figure 6.	Predicted reaction of 1 with electrophiles.	5
Figure 7.	Proposed reaction of A with anions.	5
Figure 8.	Boron centered radical anions.	7
Figure 9.	One and two electron reduction processes of [2] ⁺	7
Figure 10.	General approach for the synthesis of 4-boryl-1-diarylmethylium derivatives.	8
Figure 11.	General approach for the reduction of 4-boryl-1-diarylmethylium derivatives.	8
Figure 12.	Different oxidation states of P-C double bonds.	9
Figure 13.	General structures of α-phosphonyl- and α-phosphonio-carbocations to be studied	10
Figure 14.	Reduction of α-phosphonyl-carbocations.	11
Figure 15.	Reduction of α-phosphonio-carbocations.	11
Figure 16.	Isoelectronic relationship between diboranes and dimethylium cations.	12
Figure 17.	Synthesis of 4.	13

	Page
Figure 18. Examples of hydride bridged dimethanes 5, 6 and 7.	14
Figure 19. Müller's hydride 8 and fluoride 9 bridged disilyl cations.	15
Figure 20. Polyagostic Si-H---Si interactions.	17
Figure 21. Structure of bridging species 12 and 13.	18
Figure 22. Reaction of 14 with fluoride.	19
Figure 23. Synthesis of B-F---Si bridge.	20
Figure 24. Kawachi's Si-X-B bridging derivatives 18 and 19.	20
Figure 25. Structures of various bridging species.	21
Figure 26. Deuterium quenching of 1.	22
Figure 27. Stacked ¹ H NMR spectra showing the resonance corresponding to the 8-position of the naphthalene backbone of 20 (top) and 21 (bottom).	22
Figure 28. Synthesis of 22 and 23.	23
Figure 29. Crystal structure of 22 (50% ellipsoid, H-atoms omitted for clarity); selected bond lengths (Å) and angles (deg). Hg(1)-C(1) 2.061(8), Hg(1)-Cl(1) 2.324(2), Hg(1)-C(12) 3.021(8), C(8)-C(11) 1.559(11), O(2)-C(11), 1.436(10), C(11)-C(23) 1.533(11), C(11)-C(12) 1.503(11), C(12)-C(17) 1.387(11), C(12)-C(13) 1.398(10), C(1)-Hg(1)-Cl(1) 173.4(3), C(1)-Hg(1)-C(12) 83.8(3), Cl(1)-Hg(1)-C(12) 102.63(16), C(2)-C(1)-Hg(1) 109.3(6), C(9)-C(1)-Hg(1) 130.2(6), O(2)-C(11)-C(12) 105.1(6), O(2)-C(11)-C(23) 108.0(6), C(12)-C(11)-C(23) 109.7(7), O(2)-C(11)-C(8) 108.2(6), C(12)-C(11)-C(8) 112.6(6), C(23)-C(11)-C(8) 112.9(6), C(7)-C(8)-C(11) 116.2(7), C(9)-C(8)-C(11) 124.9(7).	25

Figure 30.	Crystal structure of 23 (50% ellipsoid, H-atoms omitted for clarity); selected bond lengths (Å) and angles (deg). Hg(1)-C(1) 2.058(8), Hg(1)-C(24) 2.096(9), Hg(1)-C(12) 2.940(8), F(1)-C(25) 1.346(12), F(2)-C(26) 1.38(2), F(3)-C(27) 1.339(15), F(4)-C(28) 1.330(16), F(5)-C(29) 1.355(16), O(2)-C(11) 1.474(11), C(8)-C(11) 1.524(11), C(11)-C(23) 1.509(13), C(11)-C(12) 1.517(12), C(1)-Hg(1)-C(24) 168.1(4), C(1)-Hg(1)-C(12) 87.3(3), C(24)-Hg(1)-C(12) 99.2(3), C(2)-C(1)-Hg(1) 111.5(7), C(9)-C(1)-Hg(1) 128.5(6), C(7)-C(8)-C(11) 117.9(8), C(9)-C(8)-C(11) 122.5(8).....	27
Figure 31.	Synthesis of 24.	30
Figure 32.	Crystal structure of 24 (50% ellipsoid, H-atoms omitted for clarity); selected bond lengths (Å) and angles (deg). C(1)-C(24) 1.473(4), O(2)-C(24) 1.348(3), O(2)-C(11) 1.495(3), O(3)-C(24) 1.210(3), C(8)-C(11) 1.511(3), C(11)-C(12) 1.513(4), C(11)-C(23) 1.514(4), C(24)-O(2)-C(11) 125.64(19), C(2)-C(1)-C(24) 119.5(2), C(9)-C(1)-C(24) 120.2(2), O(3)-C(24)-O(2) 117.7(2), O(3)-C(24)-C(1) 124.2(2), O(2)-C(24)-C(1) 118.1(2), O(2)-C(11)-C(8) 113.1(2), O(2)-C(11)-C(12) 103.31(19), C(8)-C(11)-C(12) 112.9(2), O(2)-C(11)-C(23) 104.09(19), C(8)-C(11)-C(23) 112.7(2), C(12)-C(11)-C(23) 109.9(2).....	31
Figure 33.	Crystal structure of 25 (50% ellipsoid, H-atoms omitted for clarity); selected bond lengths (Å) and angles (deg). Si(1)-O(2) 1.6325(13), Si(1)-C(24) 1.853(2), Si(1)-C(1) 1.8494(18), Si(1)-C(25) 1.853(2), O(2)-C(11) 1.4408(19), C(11)-C(23) 1.520(2), C(11)-C(12) 1.521(2), C(11)-C(8) 1.546(2), O(2)-Si(1)-C(24) 110.13(9), O(2)-Si(1)-C(1) 105.02(7), C(24)-Si(1)-C(1) 112.54(9), O(2)-Si(1)-C(25) 110.45(9), C(24)-Si(1)-C(25) 109.22(12), C(1)-Si(1)-C(25) 109.43(9), C(23)-C(11)-C(12) 109.80(13), O(2)-C(11)-C(8) 114.90(13), C(23)-C(11)-C(8) 109.36(13), C(12)-C(11)-C(8) 109.14(13), O(2)-C(11)-C(23) 106.11(13), O(2)-C(11)-C(12) 107.42(13).....	34
Figure 34.	Synthesis of 25 and [26][BF ₄].	36

Figure 35.	Crystal structure of $[26]^+$ in $[26][BF_4]$ (50% ellipsoid, H-atoms omitted for clarity); selected bond lengths (Å) and angles (deg). C(11)-C(8) 1.473(2), F(1)-C(11) 2.703(2), C(12)-C(11) 1.417(2), C(23)-C(11) 1.417(2), Si(1)-F(1) 1.6086(12), Si(1)-C(25) 1.839(2), Si(1)-C(24) 1.850(2), Si(1)-C(1) 1.8893(19), F(1)- Si(1)-C(25) 107.75(9), F(1)-Si(1)-C(24) 104.56(9), C(25)-Si(1)- C(24) 112.76(10), F(1)-Si(1)-C(1) 111.01(7), C(25)-Si(1)-C(1) 112.58(9), C(24)-Si(1)-C(1) 107.91(9), Si(1)-F(1)-C(11) 101.41(6), C(23)-C(11)-C(12) 118.30(14), C(23)-C(11)-C(8) 121.13(14), C(12)-C(11)-C(8) 120.48(13), C(23)-C(11)-F(1) 78.23(10), C(12)-C(11)-F(1) 89.79(11), C(8)-C(11)-F(1) 104.71(10), C(9)-C(1)-Si(1) 133.69(12), C(9)-C(8)-C(11) 123.92(15).	38
Figure 36.	Overlays of the experimental (yellow) and calculated (blue) structures of $[26]^+$	40
Figure 37.	Top: AIM contour plot of the electron density of $[26]^+$ shown in the Si-F-C plane along with bond paths and critical points. Bottom: NBO contour plot showing the $lp_{(F)} \rightarrow p_{z(C)}$ interaction.	41
Figure 38.	Synthesis of 27.	42
Figure 39.	Crystal structure of 27 (50% ellipsoid, non-pertinent H-atoms omitted for clarity); selected bond lengths (Å) and angles (deg). Si(1)-F(1) 1.6229(14), Si(1)-C(24) 1.846(2), Si(1)-C(25) 1.847(2), Si(1)-C(1) 1.896(2), Si(1)-H(1) 2.32(2), C(11)-H(1) 1.11(2), C(11)-C(8) 1.519(3), C(11)-C(23) 1.520(3), C(11)-C(12) 1.524(3), F(1)-Si(1)-C(24) 102.47(10), F(1)-Si(1)-C(25) 102.67(9), C(24)-Si(1)-C(25) 114.69(11), F(1)-Si(1)-C(1) 103.85(8), C(24)-Si(1)-C(1) 116.66(10), C(25)-Si(1)-C(1) 113.92(10), F(1)-Si(1)-H(1) 177.0(5), C(24)-Si(1)-H(1) 75.3(5), C(25)-Si(1)-H(1) 76.8(5), C(1)-Si(1)-H(1) 79.0(5), H(1)-C(11)- C(8) 110.0(10), H(1)-C(11)-C(23) 108.0(10), C(8)-C(11)-C(23) 111.69(17), H(1)-C(11)-C(12) 105.5(10), C(8)-C(11)-C(12) 110.94(16), C(23)-C(11)-C(12) 110.56(16), C(9)-C(1)-Si(1) 132.55(15), C(9)-C(8)-C(11) 124.56(19).	44
Figure 40.	Overlay of the experimental (yellow) and calculated (blue) structures of 27.	47

	Page
Figure 41. Top: AIM contour plot of the electron density of 27 shown in the F(1)-Si(1)-H(1)-C(11) plane along with bond paths and critical points. Bottom: NBO contour plot showing the $\sigma_{\text{C-H}} \rightarrow p_{\text{z}}(\text{Si})$ interaction.....	47
Figure 42. NBO contour plot showing the donor acceptor interactions between the fluoride lone pairs and the silicon empty p orbitals in $[\text{PhMe}_2\text{SiF}_2]^-$	48
Figure 43. Synthesis of 29.	50
Figure 44. Crystal structure of 29 (50% ellipsoid, non-pertinent H-atoms omitted for clarity); selected bond lengths (Å) and angles (deg). Si(1)-C(25) 1.866(3), Si(1)-C(24) 1.870(3), Si(1)-C(1) 1.896(3), Si(1)-H(2) 1.46(2), C(8)-C(11) 1.533(4), C(11)-H(1) 1.02(2), C(25)-Si(1)-C(24) 109.41(15), C(25)-Si(1)-C(1) 110.57(14), C(24)-Si(1)-C(1) 110.22(15), C(25)-Si(1)-H(2) 109.8(8), C(24)-Si(1)-H(2) 104.0(8), C(1)-Si(1)-H(2) 112.7(8), C(2)-C(1)-Si(1) 111.7(2), C(9)-C(1)-Si(1) 130.5(3), C(23)-C(11)-C(12) 111.2(3), C(23)-C(11)-C(8) 112.8(3), C(12)-C(11)-C(8) 110.8(3), C(23)-C(11)-H(1) 108.5(13), C(12)-C(11)-H(1) 104.7(13), C(8)-C(11)-H(1) 108.5(14), C(7)-C(8)-C(11) 114.7(3), C(9)-C(8)-C(11) 124.9(3).	50
Figure 45. NMR spectra of 30.	52
Figure 46. Synthesis of 30.	53
Figure 47. Dimerization of 31	60
Figure 48. Chichibabin's hydrocarbon 32 and Thiele's hydrocarbon 33	61
Figure 49. Synthesis of 34	62
Figure 50. One and two electron reduction processes of 35	63
Figure 51. Oxidation processes of 36	64
Figure 52. Synthesis of $[\text{37}]^-$	64
Figure 53. Synthesis of $[\text{38}]^-$	65
Figure 54. One and two electron reduction processes of $[\text{2}]^+$	65

Figure 55.	Synthesis of [39][BF ₄] and [40][BF ₄]	66
Figure 56.	Crystal structure of [39] ⁺ in [39][BF ₄] (50% ellipsoid, H-atoms omitted and mesityl groups represented by thin lines for clarity). Selected distances [Å] and angles [deg]: C(1)-C(6) 1.384(4), C(1)-C(2) 1.396(4), C(1)-C(7) 1.476(4), B(1)-C(4) 1.566(4), B(1)-C(20) 1.574(4), B(1)-C(29) 1.578(4), O(1)-C(13) 1.346(3), O(1)-C(14) 1.358(3), C(6)-C(1)-C(2) 119.8(2), C(6)-C(1)-C(7) 117.7(2), C(2)-C(1)-C(7) 122.5(2), C(4)-B(1)-C(20) 120.6(3), C(4)-B(1)-C(29) 118.0(2), C(20)-B(1)-C(29) 121.4(2), C(13)-O(1)-C(14) 121.0(2), C(19)-C(7)-C(8) 118.7(2), C(19)-C(7)-C(1) 119.8(2), C(8)-C(7)-C(1) 121.4(2).....	67
Figure 57.	Crystal structure of [40] ⁺ in [40][BF ₄] (50% ellipsoid, H-atoms omitted and mesityl groups represented by thin lines for clarity). Selected distances [Å] and angles [deg]: N(1)-C(13) 1.366(4), N(1)-C(14) 1.379(4), N(1)-C(20) 1.470(4), C(1)-C(6) 1.388(5), C(1)-C(2) 1.390(5), C(1)-C(7) 1.490(5), B(1)-C(4) 1.561(5), B(1)-C(21) 1.567(5), B(1)-C(30) 1.570(5), C(13)-N(1)-C(14) 122.1(3), C(13)-N(1)-C(20) 118.2(3), C(14)-N(1)-C(20) 119.7(3), C(6)-C(1)-C(2) 119.2(3), C(6)-C(1)-C(7) 117.8(3), C(2)-C(1)-C(7) 123.0(3), C(4)-B(1)-C(21) 120.7(3), C(4)-B(1)-C(30) 117.1(3), C(21)-B(1)-C(30) 122.3(3).....	69
Figure 58.	One and two electron reduction products of [39] ⁺ and [40] ⁺	71
Figure 59.	CV of [39] ⁺ in CH ₂ Cl ₂ , and [40] ⁺ in THF with a glassy carbon working electrode; scan rate 100 mV s ⁻¹ , 0.1 M NBu ₄ PF ₆	72
Figure 60.	Reduction of [39] ⁺	72
Figure 61.	Experimental and simulated EPR spectra of 39 [•] (left) and hyperfine coupling parameters (right).....	73
Figure 62.	Calculated spin density map of 39 [•] (isovalue 0.0006).	73
Figure 63.	Synthesis of 41	74

Figure 64.	Crystal structure of 41 (50% ellipsoid, H-atoms omitted and mesityl groups represented by thin lines for clarity). Selected distances [Å] and angles [deg]: O(1)-C(14) 1.393(10), O(1)-C(13) 1.398(10), C(1)-C(6) 1.348(11), C(1)-C(2) 1.397(12), C(1)-C(7) 1.553(11), B(1)-C(29) 1.551(14), B(1)-C(4) 1.552(13), B(1)-C(20) 1.563(13), O(2)-C(51) 1.378(10), O(2)-C(50) 1.382(9), B(2)-C(57) 1.567(14), B(2)-C(66) 1.569(14), B(2)-C(41) 1.604(13), O(3)-C(7) 1.436(10), O(3)-O(4) 1.490(7), O(4)-C(44) 1.461(9), C(14)-O(1)-C(13) 116.3(7), C(29)-B(1)-C(4) 116.9(8), C(29)-B(1)-C(20) 123.0(8), C(4)-B(1)-C(20) 120.0(9), C(51)-O(2)-C(50) 118.0(7), C(57)-B(2)-C(66) 125.6(8), C(57)-B(2)-C(41) 115.2(9), C(66)-B(2)-C(41) 119.2(8), C(7)-O(3)-O(4) 103.7(5), C(44)-O(4)-O(3) 105.0(5).....	75
Figure 65.	Synthesis of [42][BF ₄] ₂	77
Figure 66.	Crystal structure of [42] ²⁺ in [42][I ₃] ₂ (50% ellipsoid, H-atoms omitted for clarity) . Put in bond lengths etc. Selected distances [Å] and angles [deg]: O(1)-C(11) 1.366(10), O(1)-C(13) 1.391(10), O(2)-C(23) 1.364(10), O(2)-C(22) 1.376(11), O(3)-C(35) 1.343(11), O(3)-C(36) 1.360(10), C(4)-C(16) 1.463(12), C(5)-C(29) 1.514(11), C(16)-C(17) 1.407(12), C(16)-C(28) 1.434(12), C(29)-C(30) 1.399(12), C(29)-C(41) 1.417(12), C(11)-O(1)-C(13) 120.5(7), C(23)-O(2)-C(22) 118.9(7), C(35)-O(3)-C(36) 121.4(7), C(17)-C(16)-C(28) 117.2(8), C(17)-C(16)-C(4) 121.6(8), C(28)-C(16)-C(4) 121.0(8), C(30)-C(29)-C(41) 120.2(8), C(30)-C(29)-C(5) 121.2(7), C(41)-C(29)-C(5) 118.6(8).	79
Figure 67.	Cyclic voltammogram of [42][BF ₄] ₂ in MeCN with a Pt working electrode; scan rate 50 mV/sec, 0.1 M nBu ₄ NPF ₆ (vs. Fc/Fc ⁺).....	81
Figure 68.	Oxidation of 43 to [43] ⁺ and proposed dication [43] ²⁺	86
Figure 69.	Dimerization of [43] ⁺	86
Figure 70.	Reduction of [44] ²⁺	87
Figure 71.	Reduction of [45] ²⁺	87
Figure 72.	Synthesis and reduction of [46] ²⁺	88
Figure 73.	Synthesis and reduction of 47 [•]	88

	Page
Figure 74. Electrochemical series of 48	89
Figure 75. Reduction of $[49]^{2+}$	90
Figure 76. Different oxidation states of P-C double bonds.	90
Figure 77. Synthesis of $[50][OTf]_2$, $[51][OTf]_2$ and $[52][OTf]_2$	92
Figure 78. Crystal structure of $[50]^{2+}$ in $[50][OTf]_2$ (50% ellipsoid, H-atoms omitted for clarity); selected bond lengths (Å) and angles (deg). P(1)-C(15) 1.789(4), P(1)-C(27) 1.802(4), P(1)-C(21) 1.799(4), P(1)-C(9) 1.835(4), N(1)-C(11) 1.354(6), N(1)-C(13) 1.363(6), N(1)-C(14) 1.483(5), C(10)-C(9) 1.403(6), C(9)-C(12) 1.410(6), C(15)-P(1)-C(27) 112.8(2), C(15)-P(1)-C(21) 111.9(2), C(27)- P(1)-C(21) 104.8(2), C(15)-P(1)-C(9) 108.3(2), C(27)-P(1)-C(9) 108.2(2), C(21)-P(1)-C(9) 110.8(2), C(11)-N(1)-C(13) 121.5(4), C(11)-N(1)-C(14) 118.8(4), C(13)-N(1)-C(14) 119.7(4), C(10)- C(9)-C(12) 119.6(4), C(10)-C(9)-P(1) 120.9(3), C(12)-C(9)-P(1) 119.6(3).	93
Figure 79. Crystal structure of $[51]^{2+}$ in $[51][OTf]_2$ (50% ellipsoid, H-atoms omitted for clarity); selected bond lengths (Å) and angles (deg). P(1)-C(21) 1.764(7), P(1)-C(15) 1.795(7), P(1)-C(27) 1.807(7), P(1)-C(9) 1.827(7), N(1)-C(11) 1.360(8), N(1)-C(13) 1.378(8), N(1)-C(14) 1.470(8), C(9)-C(12) 1.400(9), C(9)-C(10) 1.418(9), C(21)-P(1)-C(15) 113.0(3), C(21)-P(1)-C(27) 111.6(3), C(15)- P(1)-C(27) 104.8(3), C(21)-P(1)-C(9) 110.5(3), C(15)-P(1)-C(9) 107.3(3), C(27)-P(1)-C(9) 109.4(3), C(11)-N(1)-C(13) 121.5(5), C(11)-N(1)-C(14) 118.2(6), C(13)-N(1)-C(14) 120.3(5), C(12)- C(9)-C(10) 119.8(6), C(12)-C(9)-P(1) 119.8(5), C(10)-C(9)-P(1) 120.2(5).	95
Figure 80. Crystal structure of $[52]^{2+}$ in $[52][OTf]_2$ (50% ellipsoid, H-atoms omitted for clarity); selected bond lengths (Å) and angles (deg). P(1)-C(22) 1.782(6), P(1)-C(15) 1.790(5), P(1)-C(21) 1.803(6), P(1)-C(9) 1.827(6), N(1)-C(11) 1.359(8), N(1)-C(13) 1.365(7), N(1)-C(14) 1.477(9), C(9)-C(12) 1.401(7), C(9)-C(10) 1.414(8), C(22)-P(1)-C(15) 110.8(3), C(22)-P(1)-C(21) 112.9(4), C(15)- P(1)-C(21) 101.1(3), C(22)-P(1)-C(9) 106.0(3), C(15)-P(1)-C(9) 115.0(3), C(21)-P(1)-C(9) 111.2(3), C(11)-N(1)-C(13) 122.2(5), C(11)-N(1)-C(14) 117.4(6), C(13)-N(1)-C(14) 120.4(6), C(12)- C(9)-C(10) 119.4(5), C(12)-C(9)-P(1) 118.5(4), C(10)-C(9)-P(1) 122.1(4).	97

Figure 81.	Synthesis of [53][OTf] ₂ and [54][OTf] ₂	99
Figure 82.	Representations of forms b and c of ligand stabilized carbocations.....	100
Figure 83.	Crystal structure of [53] ²⁺ in [53][OTf] ₂ (50% ellipsoid, H-atoms omitted for clarity); selected bond lengths (Å) and angles (deg). N(1)-C(13) 1.360(3), N(1)-C(11) 1.366(3), N(1)-C(14) 1.500(3), N(2)-C(15) 1.344(3), N(2)-C(19) 1.346(3), N(2)-C(9) 1.462(3), C(9)-C(10) 1.383(3), C(9)-C(12) 1.386(3), C(13)-N(1)-C(11) 122.45(19), C(13)-N(1)-C(14) 119.4(2), C(11)-N(1)-C(14) 117.9(2), C(15)-N(2)-C(19) 121.76(19), C(15)-N(2)-C(9) 118.51(18), C(19)-N(2)-C(9) 119.52(18), C(10)-C(9)-C(12) 123.56(19), C(10)-C(9)-N(2) 117.42(19), C(12)-C(9)-N(2) 119.0(2).	101
Figure 84.	Crystal structure of [54] ²⁺ in [54][OTf] ₂ (50% ellipsoid, H-atoms omitted for clarity); selected bond lengths (Å) and angles (deg). N(1)-C(13) 1.375(6), N(1)-C(11) 1.382(6), N(1)-C(14) 1.484(6), N(2)-C(15) 1.366(6), N(2)-C(19) 1.376(6), N(2)-C(9) 1.445(6), N(3)-C(17) 1.316(6), N(3)-C(20) 1.462(6), N(3)-C(21) 1.465(6), C(9)-C(10) 1.391(6), C(9)-C(12) 1.393(6), C(13)-N(1)-C(11) 121.8(4), C(13)-N(1)-C(14) 117.7(4), C(11)-N(1)-C(14) 120.4(4), C(15)-N(2)-C(19) 119.2(4), C(15)-N(2)-C(9) 121.2(4), C(19)-N(2)-C(9) 119.7(4), C(17)-N(3)-C(20) 121.0(4), C(17)- N(3)-C(21) 120.8(4), C(20)-N(3)-C(21) 118.0(4), C(10)-C(9)- C(12) 122.4(4), C(10)-C(9)-N(2) 118.8(4), C(12)-C(9)-N(2) 118.8(4).	103
Figure 85.	CV of [50] ²⁺ , [53] ²⁺ and [54] ²⁺ in CH ₃ CN with a glassy carbon working electrode; scan rate 100 mV s ⁻¹ , 0.1 M NBu ₄ PF ₆	106
Figure 86.	Eperimental and simulated EPR spectra of [50] ⁺ (left) and hyperfine coupling parameters (right).....	106
Figure 87.	Synthesis of [56] ⁺	107

Figure 88.	Crystal structure of $[56]^+$ in $[56][OTf]$ (50% ellipsoid, H-atoms omitted for clarity); selected bond lengths (Å) and angles (deg). P(1)-O(1) 1.458(5), P(1)-O(3) 1.562(5), P(1)-O(2) 1.569(5), P(1)-C(9) 1.826(7), O(2)-C(15) 1.452(9), N(1)-C(11) 1.365(8), N(1)-C(13) 1.368(8), N(1)-C(14) 1.479(8), O(3)-C(17) 1.469(8), O(1)-P(1)-O(3) 116.1(3), O(1)-P(1)-O(2) 114.1(3), O(3)-P(1)-O(2) 103.5(3), O(1)-P(1)-C(9) 115.7(3), O(3)-P(1)-C(9) 99.8(3), O(2)-P(1)-C(9) 105.9(3), C(15)-O(2)-P(1) 120.5(5), C(11)-N(1)-C(13) 121.4(6), C(11)-N(1)-C(14) 117.7(5), C(13)-N(1)-C(14) 120.9(5), C(17)-O(3)-P(1) 120.4(5), C(10)-C(9)-C(12) 119.2(6), C(10)-C(9)-P(1) 120.9(5), C(12)-C(9)-P(1) 119.9(5).	108
Figure 89.	CV of $[56]^+$ in CH_3CN with a glassy carbon working electrode; scan rate 100 mV s^{-1} , 0.1 M NBu_4PF_6	110
Figure 90.	Experimental and simulated EPR spectra of 56^+ (left) and hyperfine coupling parameters (right)	111
Figure 91.	Bridged diboranes 58, 59 and 60	117
Figure 92.	Bridging in <i>o</i> -phenylene derivatives	118
Figure 93.	Fluoride binding of 62 and 63	119
Figure 94.	Fluoride binding of 64	120
Figure 95.	Fluoride binding of 66	121
Figure 96.	Previously synthesized derivatives 68 and 69	122
Figure 97.	Synthesis of 70	122

- Figure 98. ORTEP view of 70 (50% ellipsoid), H atoms are omitted and the mesityl groups are represented by thin lines. Selected distances [Å] and angles [deg]: Hg(1)-C(31) 2.036(10), Hg(1)-C(1) 2.172(12), Hg(1)-C(41) 3.132(12), Hg(1)-C(21) 3.156(12), Hg(1)-B(1) 3.462(15), Hg(1)-B(2) 3.463(14), B(1)-C(21) 1.549(19), B(1)-C(8) 1.612(19), B(1)-C(11) 1.63(2), B(1)-B(2) 6.139(17), C(1)-C(9) 1.375(17), C(1)-C(2) 1.380(17), C(2)-C(3) 1.438(18), B(2)-C(51) 1.55(2), B(2)-C(38) 1.580(18), B(2)-C(41) 1.589(18), C(31)-Hg(1)-C(1) 168.1(4), C(21)-B(1)-C(8) 125.7(12), C(21)-B(1)-C(11) 119.3(11), C(8)-B(1)-C(11) 114.1(11), C(51)-B(2)-C(38) 113.6(11), C(51)-B(2)-C(41) 121.2(11), C(38)-B(2)-C(41) 124.6(12)..... 124
- Figure 99. Optimized geometry and LUMO of 68, 69 and 70 (isodensity value = 0.04)..... 127
- Figure 100. Cyclic voltammograms of 68 (top) 69 (middle) and 70 (bottom) in THF with a glassy-carbon working electrode (0.3 M $n\text{Bu}_4\text{NPF}_6$). Scan rates: $\nu = 100 \text{ mV s}^{-1}$ 128
- Figure 101. Changes in the differential pulsed voltammogram of 69 (top) and 70 (bottom) observed upon the addition of $n\text{Bu}_4\text{NF}$ to a THF solution (0.3 M)..... 130
- Figure 102. Equilibrium between 69 and $[\text{69-}\mu_2\text{-F}]^-$ 130
- Figure 103. Equilibrium between 70, $[\text{70-}\mu_2\text{-F}]^-$ and $[\text{70-}(\mu_2\text{-F})_2]^{2-}$ 131
- Figure 104. Top: Changes in the UV-vis absorption spectra of a solution of 70 (3 mL, $5.5 \times 10^{-5} \text{ M}$ in THF) upon addition of a TBAF solution ($4.7 \times 10^{-3} \text{ M}$ in THF). Bottom; Binding isotherm obtained by monitoring the absorbance at 360 nm. 132
- Figure 105. (left): Changes in the UV-vis absorption spectrum of 68 (3.0 mL, $5.1896 \times 10^{-5} \text{ M}$, in chloroform) upon addition of a TBAF solution ($1.90 \times 10^{-2} \text{ M}$, in chloroform). (right): 1:1 binding isotherm for the formation of $[\text{68-}\mu_2\text{-F}]^-$ 134
- Figure 106. (left): Changes in the UV-vis absorption spectrum of 69 (3.0 mL, $5.00 \times 10^{-5} \text{ M}$, in chloroform) upon addition of a TBAF solution ($3.02 \times 10^{-2} \text{ M}$, in chloroform). (right): 1:1 binding isotherm for the formation of $[\text{69-}\mu_2\text{-F}]^-$ 134

Figure 107. (left): Changes in the UV-vis absorption spectrum of 70 (3.0 mL, 2.525×10^{-5} M, in chloroform) upon addition of a TBAF solution (3.02×10^{-2} M, in chloroform). (right): 1:1 binding isotherm for the formation of [70- μ_2 -F].	135
Figure 108. ORTEP view of [68- μ_2 -F] ⁻ in [S(NMe ₂) ₃][68- μ_2 -F] (50% ellipsoid). H atoms are omitted and the mesityl groups are represented by thin lines. Selected distances [Å] and angles [deg]: B(1)-F(1) 1.596(5), B(2)-F(1) 1.604(5), B(1)-C(1) 1.612(6), B(1)-C(11) 1.633(6), B(1)-C(21) 1.663(6), B(1)-B(2) 2.922(7), B(2)-C(8) 1.614(7), B(2)-C(31) 1.598(7), B(2)-C(32) 1.602(7); B(1)-F(1)-B(2) 126.0(3), C(1)-B(1)-F(1) 103.8(3), C(8)-B(2)-F(1) 105.2(3), C(1)-B(1)-C(11) 110.1(3), C(1)-B(1)-C(21) 117.4(3), C(11)-B(1)-C(21) 117.7(3), C(8)-B(2)-C(31) 112.1(4), C(8)-B(1)-C(32) 113.4(4), C(31)-B(2)-C(32) 114.2(4).	136
Figure 109. ORTEP view of [70- μ_2 -F] ⁻ in [S(NMe ₂) ₃][70- μ_2 -F] (50% ellipsoid). H atoms are omitted and the mesityl groups are represented by thin lines. Selected distances [Å] and angles [deg]: Hg(1)-C(1) 2.079(14), Hg(1)-C(31) 2.119(12), Hg(1)-F(1) 2.576(4), B(1)-F(1) 1.487(10), B(1)-C(11) 1.672(14), B(1)-C(8) 1.655(12), B(1)-C(21) 1.685(16), B(2)-C(41) 1.567(14), B(2)-C(38) 1.592(13), B(2)-C(51) 1.576(16), C(1)-Hg(1)-C(31) 169.0(4), C(1)-Hg(1)-F(1) 86.4(3), C(31)-Hg(1)-F(1) 104.3(3), F(1)-B(1)-C(11) 104.8(6), F(1)-B(1)-C(8) 106.4(6), C(11)-B(1)-C(8) 116.1(7), F(1)-B(1)-C(21) 105.7(7), C(11)-B(1)-C(21) 113.2(8), C(8)-B(1)-C(21) 109.6(7), C(41)-B(2)-C(38) 116.6(9), C(41)-B(2)-C(51) 119.5(9), C(38)-B(2)-C(51) 122.9(8), B(1)-F(1)-Hg(1) 104.7(4).	139
Figure 110. Equations depicting how fluoride ion affinities were calculated.	144
Figure 111. Synthesis of [26][BF ₄].	147
Figure 112. Synthesis of 27	147
Figure 113. Synthesis of 30.	148

	Page
Figure 114. Changes in the differential pulsed voltammogram of 69 (top) and 70 (bottom) observed upon the addition of $n\text{Bu}_4\text{NF}$ to a THF solution (0.3 M).....	149
Figure 115. Eperimental and simulated EPR spectra of $[50]^{2+}$ (left) and hyperfine coupling parameters (right).....	150
Figure 116. Representations of forms b and c of ligand stabilized carbodications.....	151
Figure 117. Eperimental and simulated EPR spectra of $[56]^+$ (left) and hyperfine coupling parameters (right).....	152

LIST OF TABLES

	Page
Table 1. Crystal Data, Data Collection, and Structure Refinement for 22·THF.	26
Table 2. Crystal Data, Data Collection, and Structure Refinement for 23·2THF.	28
Table 3. Crystal Data, Data Collection, and Structure Refinement for 24-0.5(CH ₂ Cl ₂).	32
Table 4. Crystal Data, Data Collection, and Structure Refinement for 25.	35
Table 5. Crystal Data, Data Collection, and Structure Refinement for [26][BF ₄].	39
Table 6. Crystal Data, Data Collection, and Structure Refinement for 27.	45
Table 7. Computed metrical parameters and electron density for molecules 27 and 28X.	49
Table 8. Crystal Data, Data Collection, and Structure Refinement for 29.	51
Table 9. Crystal Data, Data Collection, and Structure Refinement for [39][BF ₄].	68
Table 10. Crystal Data, Data Collection, and Structure Refinement for [40][BF ₄].	70
Table 11. Crystal Data, Data Collection, and Structure Refinement for 41-2(CH ₂ Cl ₂).	76
Table 12. Crystal Data, Data Collection, and Structure Refinement for [42][I ₃] ₂	80
Table 13. Crystal Data, Data Collection, and Structure Refinement for [50][OTf] ₂ -CH ₃ CN.	94
Table 14. Crystal Data, Data Collection, and Structure Refinement for [51][OTf] ₂ -Et ₂ O.	96
Table 15. Crystal Data, Data Collection, and Structure Refinement for [52][OTf] ₂	98

	Page
Table 16. Crystal Data, Data Collection, and Structure Refinement for [53][OTf] ₂ -CH ₃ CN.....	102
Table 17. Crystal Data, Data Collection, and Structure Refinement for [54][OTf] ₂ -CH ₃ CN.....	104
Table 18. Crystal Data, Data Collection, and Structure Refinement for [56][OTf].....	109
Table 19. Crystal Data, Data Collection, and Structure Refinement for 70-0.5(CHCl ₃).....	125
Table 20. Crystal Data, Data Collection, and Structure Refinement for [S(NMe ₂) ₃][68-μ ₂ -F].	137
Table 21. Crystal Data, Data Collection, and Structure Refinement for [S(NMe ₂) ₃][70-μ ₂ -F].	140

CHAPTER I

INTRODUCTION AND RESEARCH OBJECTIVES

1.1 Overview

Due to the broad scope of the research presented in this dissertation, this introduction has been divided into three separate sections to more clearly convey the individual ideas and goals.

1.2 Synthesis of compounds displaying unusual bonding

1.2.1 Introduction

Diboranes based on a rigid naphthalene backbone have been extensively studied in the context of anion complexation.¹⁻⁵ These diboranes readily bind fluoride and hydride to produce complexes featuring symmetrical B-F-B and B-H-B bridges respectively (Figure 1).

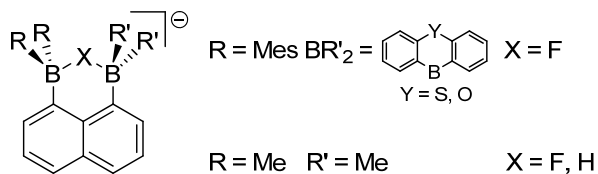


Figure 1. Anion chelate complexes formed by 1,8-diborylnaphthalenes.

This dissertation follows the style and format of the *Journal of the American Chemical Society*.

Triarylmethyl cations are the isoelectronic analogs of triarylboranes. Because of this isoelectronic relationship, it could, in principle, be expected that 1,8-bis(methylium)naphthalenediyl dications will have properties similar to those of their 1,8-bis(boryl)naphthalene counterparts. However, reaction of 1,8-bis(diphenylmethylium)naphthalenediyl dication with fluoride, leads to the formation of an unsymmetrical C-F→C bridge where the fluoride is preferentially bound to one of the former methylium centers (Figure 2).⁶

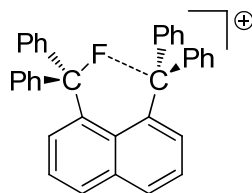
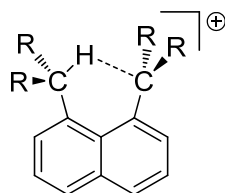


Figure 2. Structure of the fluoride adduct of the 1,8-bis(diphenylmethylium)naphthalenediyl dication showing the unsymmetrical C-F→C bridge.

Related results have been independently obtained by the groups of McMurry and Suzuki who have investigated the formation C-H-C 3c-2e bonds (Figure 3). All spectroscopic and structural evidence obtained by these two groups point to the formation of unsymmetrical C-H---C bridges.⁷⁻¹⁰ When compared to boron, carbon seems reluctant to form symmetrical C-F-C or C-H-C interactions. This reluctance can be correlated to the increased covalency of C-F and C-H bonds which disfavor the formation of more ionic $C^{\delta+}-X^{\delta-}-C^{\delta+}$ symmetrical bridges.¹¹



$R_2C^+ = 10\text{-methyl-9-acridinium}$

$R = C_6H_5$

$R = p\text{-C}_6\text{H}_4\text{OMe}$

Figure 3. Structures of the hydride adducts of 1,8-bis(diarylmethylium)naphthalenediyl dications showing the unsymmetrical C-H→C bridges.

In fact, recent results obtained in the chemistry of 1,8-bis(silylium)naphthalenediyl cations seem to confirm this assumption. Indeed, Müller and coworkers reported disilyl cations featuring symmetric Si-F-Si and Si-H-Si bridges respectively (Figure 4).¹² The formation of these symmetrical bridges can be correlated to the lower electronegativity of silicon which results in a greater polarity of the Si-X bonds allowing for a more ionic and thus symmetrical $Si^{\delta+}\text{-X}^{\delta-}\text{-Si}^{\delta+}$ bridge.

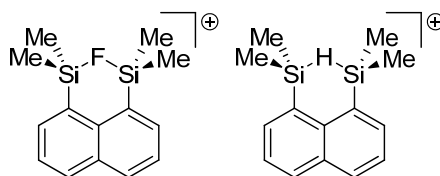


Figure 4. General bridging interactions in silanes.

In an effort to further our understanding of multicenter bonding interactions, we set out to investigate the formation of derivatives in which a hydride or fluoride anion bridges a carbon atom and a Lewis acidic main group element.

1.2.2 Objectives

Aim 1: Synthesis of compounds featuring proximal carbocationic and Lewis acidic centers

In an attempt to synthesize 1,8-bis(diarylmethanol)naphthalenediyl diols, a former graduate student in our group, Dr. Huadong Wang, noted that the reaction of 1,8-dilithionaphthalene with 2 equivalents of diarylketone does not always proceed to completion and often affords after quenching the corresponding 1-naphthyl-diarylmethanol. A similar reaction was observed upon treatment of 1,8-dilithionaphthalene with xanthone (Figure 5). This observation suggests the intermediacy of a dilithio-reagent (**1**), which upon quenching affords the corresponding alcohol.

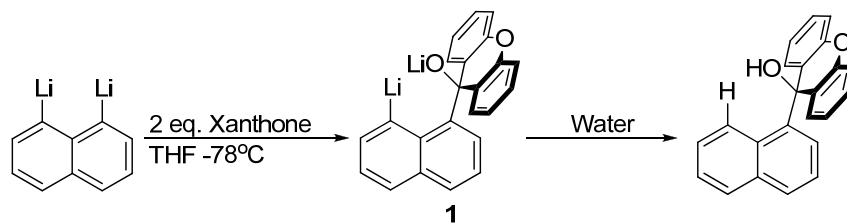


Figure 5. Synthesis of **1**.

Realizing that the putative dilithio derivative **1** may serve as a useful reagent for the synthesis of unsymmetrically substituted 1,8-naphthalene derivatives, it became the first

objective of this dissertation to ascertain its formation and study its reaction with various main group electrophiles to ultimately afford derivatives of type **A** (Figure 6).

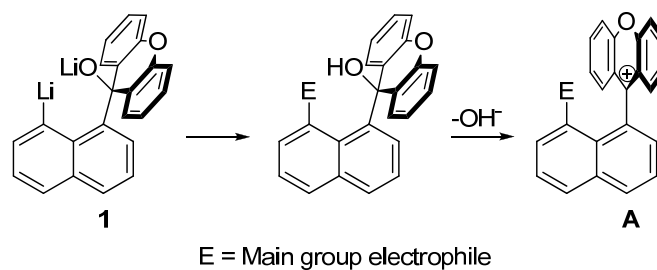


Figure 6. Predicted reaction of **1** with electrophiles.

Aim 2: Synthesis of compounds displaying unusual bridging interactions

Once isolated, these derivatives (type **A**, Figure 7) will be allowed to react with various small anions including fluoride and hydride. Because of the proximity of the carbocationic center and Lewis acidic main group element, it is expected that the added fluoride or hydride will form a bridge between the former carbocationic center and the Lewis acidic main group element.

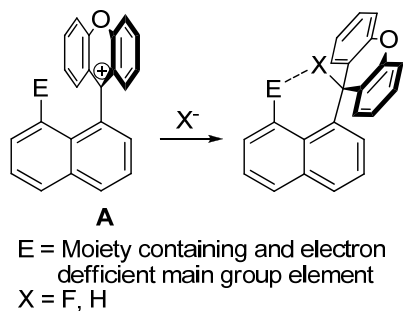


Figure 7. Proposed reaction of **A** with anions.

The presence of these bridges will be ascertained by a combination of theoretical and experimental methods. In addition to allowing for the characterization of new multicentered interactions, these studies may serve to model intermediates involved in the activation of C-H and C-F bonds by electrophiles.

1.3 Synthesis and redox properties of borata-alkenes

1.3.1 Introduction

Owing to their isoelectronic relationship to neutral methyl radicals, the chemistry of stable boron-centered radical anions $\text{Ar}_3\text{B}^{\cdot-}$ (**B**, Ar = aryl) has been intensively investigated (Figure 8).^{3,13} These compounds are usually prepared by chemical or electrochemical reduction of neutral tris(aryl)boranes.¹⁴ Although delocalization of the radical over the aryl rings accounts for the stability of such systems,¹⁵⁻²⁵ both X-ray and EPR studies show that, in some instances, the unpaired electron can be mainly localized at boron.²⁶ The reduction chemistry of organoboranes has been extended to diboranes of type **C** and **D** which can be reduced by one electron to produce derivatives featuring a one-electron σ ²⁷⁻³⁰ or π -bond,^{1,31,32} respectively. While the structural characterization of complexes of types **B** and **C** has been achieved, the identity of radicals of type **D** has been inferred from EPR spectroscopy and DFT calculations.

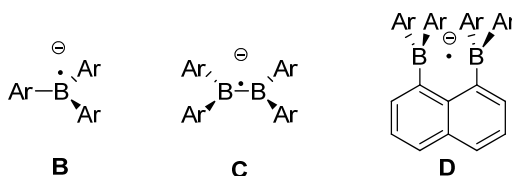


Figure 8. Boron centered radical anions.

A common feature uniting radicals **B-D** is their highly reducing nature. Because of this property, such radicals are very reactive which complicates their isolation and structural characterization. In an effort to increase the stability of such radicals, the Gabbaï group recently investigated the reduction of $[2]^+$ (Figure 9).^{33 34} In addition to isolating the radical 2^\bullet as the one-electron reduction product, this investigation also revealed that 2^+ can be reduced by two electrons to afford $[2]^-$. Thus, derivatives $[2]^+$, 2^\bullet and $[2]^-$ represent one of the rare main group series which can be isolated in three separate redox states.

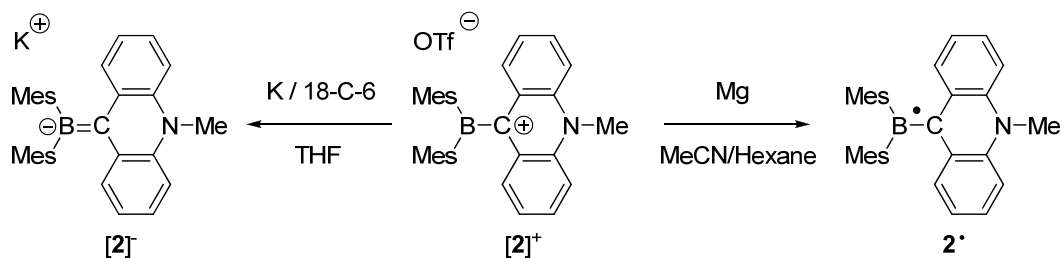


Figure 9. One and two electron reduction processes of $[2]^+$.

1.3.2 Objective

Aim: Synthesis and redox properties of extended cationic boranes

Hoping to verify if other boron containing compounds could be used for similar redox chemistry, we have decided to investigate analogs of **2** in which the boron and methylum center are connected by phenylene linkers. The cationic boron containing derivatives will be synthesized from their corresponding alcohols (Figure 10).

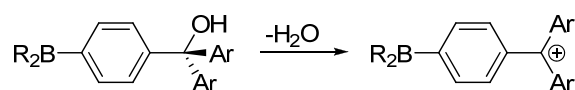


Figure 10. General approach for the synthesis of 4-boryl-1-diarlylmethyl derivatives.

Once isolated, the reduction of these cationic boranes will be studied. Efforts to isolate and/or characterize the reduction products will also be considered (Figure 11).

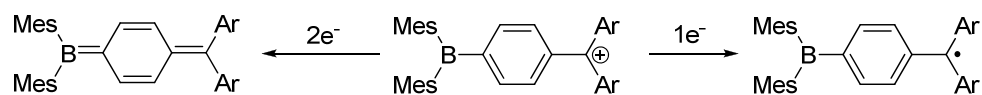


Figure 11. General approach for the reduction of 4-boryl-1-diarlylmethyl derivatives.

1.4 Synthesis of phosphorus containing radicals

1.4.1 Introduction

Phosphorus ylids (type **E**, Figure 12) have been widely investigated in organic chemistry and main group chemistry. Surprisingly, very little is known about their redox behavior.³⁵⁻³⁸ While a few reports indicate that they can be oxidized to produce radical cations of type **E^{•+}**,^{35,37,38} their double oxidation into α -phosphonio-carbocations of type **E²⁺** has been claimed³⁷ but not firmly demonstrated. As a result, the structural and spectroscopic changes accompanying this possible process have never been experimentally studied.

Although radicals of type **E^{•+}** have been detected, their isolation in the condensed state has never been reported. A possible factor which may complicate isolation of such species is their cationic character and associated high electrophilicity. On the basis of this argument, the study of neutral α -phosphonyl-methyl radicals (type **F[•]**) may provide an appealing alternative.³⁹

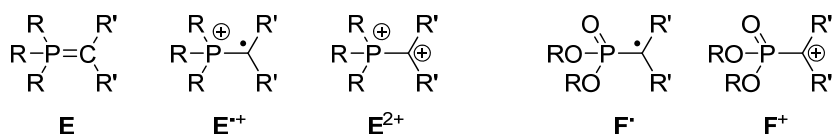


Figure 12. Different oxidation states of P-C double bonds.

1.4.2 Objectives

Aim: Synthesis and reduction of α -phosphonyl and α -phosphonio-carbocations

The α -phosphonyl- and α -phosphonio-carbocations studied herein will be synthesized employing the acridine scaffold. The carbocationic nature of these derivatives can be understood by considering the Lewis structures shown in Figure 13.

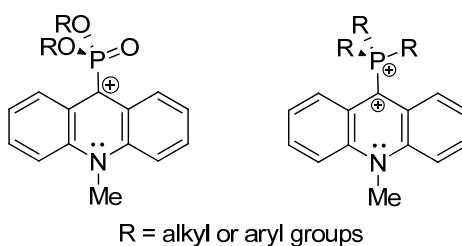


Figure 13. General structures of α -phosphonyl- and α -phosphonio-carbocations to be studied

Once isolated, all α -phosphonyl-carbocations will be studied by cyclic voltammetry. The reversibility of the reduction processes will serve to assess the stability of the resulting radicals. If the cyclic voltammogram indicates that the compounds are stable toward reduction, we will attempt to isolate the neutral radicals (Figure 14).

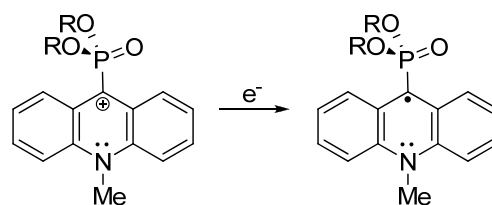


Figure 14. Reduction of α -phosfonyl-carbocations.

The α -phosphonio carbocations can be regarded as the doubly oxidized version of phosphorus ylids.³⁷ In order to confirm this view, we will study their redox behavior using cyclic voltammetry. We expect that the dication will exhibit two reversible reduction waves corresponding to the sequential population of the P-C π -orbital. If this is indeed the case, we will attempt to isolate both the radical cations and the neutral ylids (Figure 15). Such studies are important because few main group molecules have been shown to be stable in three distinct redox states.^{28-30,40-43}

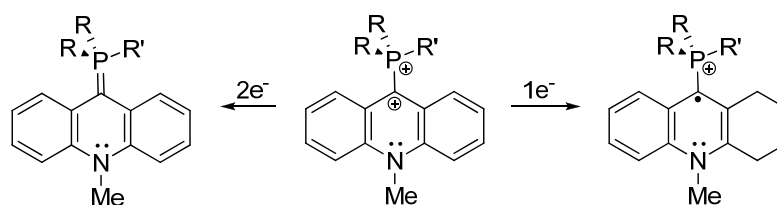


Figure 15. Reduction of α -phosphonio-carbocations.

CHAPTER II

A $R_3C-H \rightarrow SiFR_3$ AGOSTIC INTERACTION*

2.1 Background

2.1.1 C-X \rightarrow C bridged cations

It has been shown that the diboranes mentioned in section 1.2.1 readily bind fluoride. Owing to their isoelectronic relationship with boranes, methylium cations have also been studied as anion receptors. Placement of two diarylmethyl cations on the 1,8-naphthalene scaffold would constitute the carbon analog of the aforementioned 1,8-bis(diarylboryl)naphthalenediyl diboranes (Figure 16).

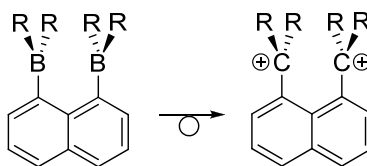


Figure 16. Isoelectronic relationship between diboranes and dimethylium cations.

Though they bind fluoride like their diborane counterparts, these 1,8-bis(diarylmethyl cation)naphthalenediyl dication, however, are reluctant to form symmetrical bridges similar to that observed for the borane derivatives. In 2004, the

* Reprinted in part with permission from, "A $R_3C-H \rightarrow SiFR_3^+$ Agostic Interaction"; C. L. Dorsey, F. P. Gabbaï; *Organometallics*, **2008**, 27, 3065-3069, Copyright 2008 by the American Chemical Society.

Gabbaï group successfully synthesized and structurally characterized the first example of a C-F→C bridged cation.⁶ Starting from 1,8-bis(diphenylmethylium)naphthalene **3**, **4** was isolated upon the addition of fluoride (Figure 17). This derivative displays unsymmetrical bridging of the former methylium centers by the fluoride anion with C-F distances of 1.4243(17) and 2.4444(17) Å, respectively. DFT calculations, however, reveal a weak interaction between the fluoride and the second methylium center. This interaction can be quantified using AIM calculations that show an electron density at the C→F bond critical point of $2.16 \times 10^{-2} \text{ e bohr}^{-3}$. Despite its weakness, this interaction affects the dynamic properties of the molecule which displays rapid exchange of the fluoride between the two former methylium centers with an activation energy of $52(\pm 3) \text{ KJ mol}^{-1}$ as determined by VT $^1\text{H NMR}$ studies.

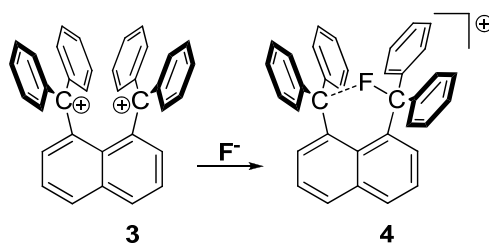


Figure 17. Synthesis of **4**.

Suzuki and co-workers have also studied bridging interactions involving 1,8-bis(diarylmethylium)naphthalene dication units similar to **4**. In 2005, they synthesized the hydride bridged derivative **5** (Figure 18).^{9 10 44} This compound displays similar properties to the fluoride bridged derivative **4**. The bridging hydride readily undergoes a

1,5-hydride shift at room temperature to give a ^1H NMR spectrum representative of a C_s symmetrical molecule. More recently, the Suzuki group has successfully synthesized the hydride bridged derivatives **6** and **7**. Compound **6** is the hydride analog of **4** which proved to be difficult to obtain by addition of hydride to dication **3**. These derivatives all feature C-H bond lengths of 1.01 Å av. and 2.25 Å av. for the covalent and dative interactions respectively.

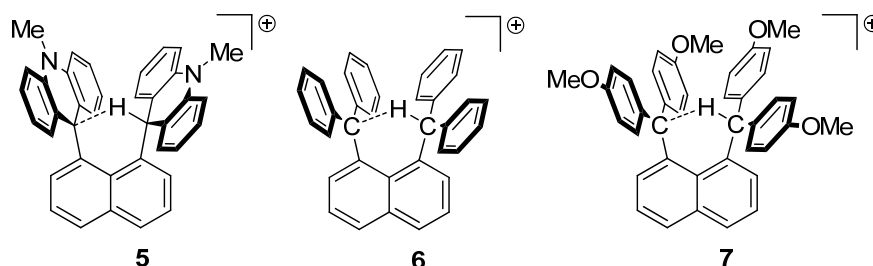


Figure 18. Examples of hydride bridged dimethanes **5**, **6** and **7**.

2.1.2 Bridged disilanes

Silicon based systems similar to the $C-X\rightarrow C$ species discussed in section 2.1.1 have been reported by Müller and co-workers who have synthesized the first examples of cationic bridged disilicon species based on the 1,8-naphthalenediyl scaffold (Figure 19).

¹² Derivative **8** features a 3c-2e hydride bridge. The geometry about the bridging hydride is consistent with equal sharing of the hydride between two silicon centers. With Si-H bond lengths of 1.583 and 1.677 Å and an Si-H-Si angle of 132°, the mutual sharing is clear. The naphthalene backbone is slightly twisted to allow room for the

bridging hydride, and the geometry of the silicon centers are both distorted between tetrahedral and trigonal planar ($\Sigma_{(C-Si-C)} = 345.5^\circ$ and 346.7°). Derivative **9** can be obtained from **8** by simply treating a solution of **8** with fluorocarbons (i.e. fluorodecane or benzyl trifluoride). The resulting fluoride bridged species **9** shows a remarkable resemblance to **8** with Si-F bond lengths of 1.755 and 1.763 Å.

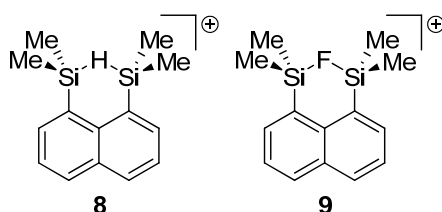


Figure 19. Müller's hydride **8** and fluoride **9** bridged disilyl cations.

Previously, the Nikonov group had synthesized **10** by the hydride abstraction reaction shown in Figure 20.⁴⁵ Indeed, the ^1H NMR of **10** is indicative of a D_{6h} symmetrical molecule with single resonance corresponding to the Si-H at 4.60 ppm and a methyl resonance at 0.78 ppm. Both resonances are observed as singlets indicating fast hydride exchange on the NMR timescale also referred to as a “hydride current.” Examination of the solid state structure shows the presence of a hydride that bridges two silicon atoms reminiscent to that observed for **8**. The formal silylium centers are essentially planar ($\Sigma_{\angle C-Si-C} = 358.9^\circ$) with two equivalent elongated bonds of 1.686 Å to a single bridging hydride. These silylium centers are stabilized by two β -hydride agostic interactions of 1.980 Å originating from neighboring Me_2SiH units. In order to better elucidate the

bonding observed in **10**, derivative **11** was synthesized. By simply replacing one of the dimethylsilane units with a methyl group, the “hydride current” observed in **10** was effectively “insulated.” In **11**, the methyl and hydride ^1H NMR signals are clearly resolved with the resonances for β -hydrides at 4.28 ppm shifted upfield from the free Si-H resonances observed at 4.53 ppm which is indicative of agostic bonding. When compared to the β -methyl resonances observed at 0.89 ppm, those for the silylium methyl groups appear downfield at 1.02 ppm owing to the cationic nature of the silicon center. ^{29}Si NMR reveals three distinct resonances for the various silicon centers. The free silane moieties appear at -4.5 ppm as doublets of septets. The β -silicon resonances appear at 33.5 ppm as doublets of septets with approximately an 80 Hz decrease (166.2 Hz to 87.2 Hz) in the Si-H coupling constant when compared to the free silane moieties. Finally, the silylium resonances appear at 34.3 ppm as multiplets. Upon selective decoupling of the methyl resonances, the silylium resonances appear as triplets with Si-H coupling of 16.1 Hz providing clear evidence for the diagnostic stabilization of the silylium centers.

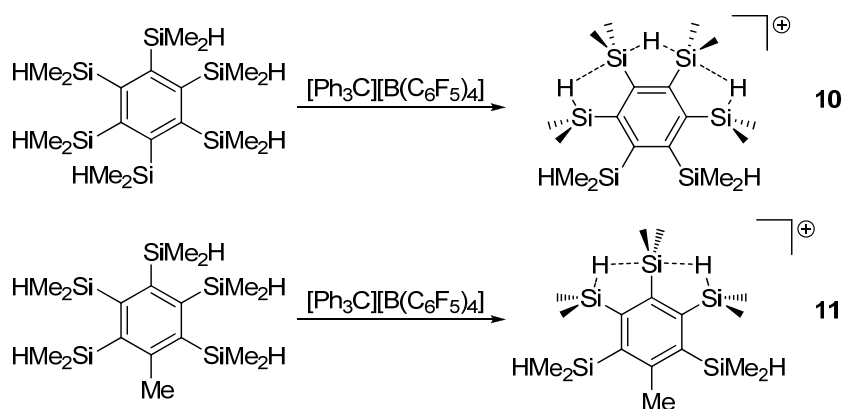


Figure 20. Polyagostic Si-H---Si interactions.

Low lying σ^* orbitals on silicon allow for neutral silane moieties to display Lewis acidity as well. In 1994, Ebata and co-workers synthesized the neutral derivatives **12** and **13** which illustrate the ability of the Si-X (X = F, OMe) σ^* orbital to enhance the Lewis acidity of the silicon center (Figure 21).⁴⁶ In **12**, all fluorine atoms appear to be shared between at least two silicon centers based on ^{29}Si NMR. In fact, at 273 K, the ^{29}Si NMR signal is observed as a triplet, but upon warming to 328 K, the signal is transformed into a septet indicating rapid dynamic exchange on the NMR timescale. Similarly, the ^1H NMR splitting patterns for the methyl groups show the same trend. This indicates that at low temperatures, each silicon atom only samples two fluorine atoms at a time, but at high temperatures, all fluorine atoms are shared equally resulting in the observed splitting patterns. Interestingly, examination of the solid state geometry of **12** reveals an Si-F bond length of 1.63 Å (av.) and an Si-F---Si interaction of 2.39 Å (av.) suggesting that the fluorine atoms are positioned to maximize interaction with only one silicon center rather than two. By simply substituting the fluorine atoms in **12** for

methoxy groups in **13**, however, mutual sharing of the X groups was observed in the solid state. In fact, the geometry adopted by the molecule exactly mimics that calculated for a molecule with D_{6h} symmetry. The Si-O bond distances are all 1.88 Å with the O-Si-O units arranged in a linear fashion and the C-Si-C bond angles are all 120°.

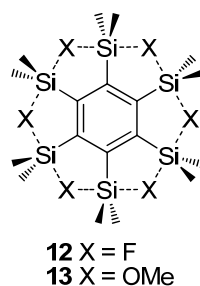


Figure 21. Structure of bridging species **12** and **13**

Silanes have also been investigated for their fluoride binding properties. Several groups have reported symmetrical fluoride chelation by disilanes. The Tamao group has shown that 1,2-bis(phenyldifluorosilyl)benzene **14** readily chelates fluoride (Figure 22).^{47 48} Addition of fluoride to a THF solution of **14** results in the formation of the symmetrically bridged species **15**. The small variation of the Si-F bond lengths (1.898(4) and 2.065(4) Å) for **15** confirm this fact. Furthermore, the F-Si-F bond angles to the fluorine atoms opposite the bridge are 172.6(2) and 174.5(2)° while the F-Si-F angles to the remaining fluorine atoms are 82.3(2) and 80.9(2)° suggesting a trigonal bipyramidal geometry about the silicon atoms. Further evidence indicating equal sharing of the bridging fluorine can be obtained by examining the ^{19}F and ^{29}Si NMR spectra. At RT, a single resonance is detected at -117.3 ppm in the ^{19}F NMR indicating

equal sharing of the fluorine atoms, and a significant upfield shift of the ^{29}Si NMR resonance from -30.21 ppm to -90.03 ppm is observed which is consistent with the formation of 5-coordinate silicon centers.

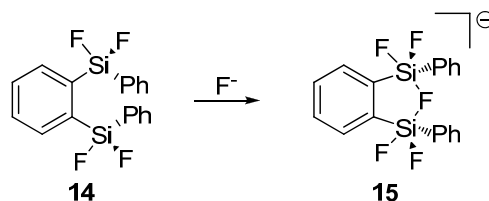


Figure 22. Reaction of **14** with fluoride

2.1.3 Bridged hybrid Lewis acids

Katz has also developed new approaches for the synthesis of polyfunctional systems on the naphthalene scaffold.^{2,49} Included in these examples is **16** which upon addition of fluoride produces the corresponding fluoroborate **17** with a novel B-F---Si bridge (Figure 23). An interaction between the fluorine and silicon centers is apparent upon examination of the solid state structure. The F-Si separation of 2.714(7) Å is well within the sum of the van der Waals radii indicating a substantial interaction. Also, the silicon center adopts a distorted trigonal bipyramidal geometry ($\Sigma_{\angle\text{C-Si-C}} = 343.2^\circ$ for the equatorial carbons and $\Sigma_{\angle\text{F-Si-C}} = 177.5^\circ$ for the axial carbon). Fluorine coupling ($^1J_{\text{Si-F}} = 13.2$ Hz) to the silicon center is also observed in the ^{29}Si NMR further substantiating the presence of an interaction.

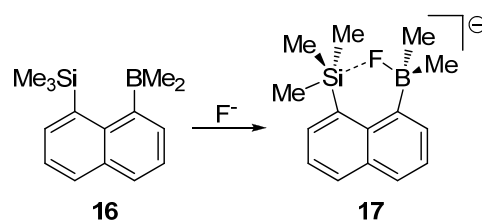


Figure 23. Synthesis of B-F---Si bridge

In 2008, Kawachi and co-workers synthesized a series of bidentate hybrid boron/silicon Lewis acids on the *o*-phenylene backbone that display bonding similar to that observed by Katz for his hybrid derivatives.^{50,51} Kawachi's derivatives display a wide array of hydride and fluoride bonding motifs. Derivative **18** displays a long Si-F interaction with the bridging fluoride of 2.2481(13) Å, while **19** features a bridging hydride with a long B-H distance of 3.22(2) Å and a Si-H distance of 1.47(2) Å (Figure 24). It is worthwhile to note that **18** is more stable than its non-silylated monofunctional fluoroborate analogue.

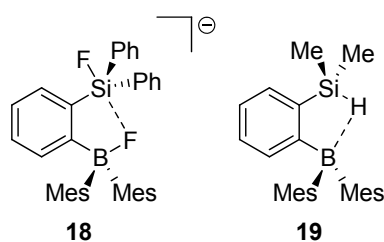


Figure 24. Kawachi's Si-X-B bridging derivatives **18** and **19**.

2.2 Introduction

As shown in the preceding section, the naphthalene backbone has often been used as a scaffold for the stabilization of unusual bridging interactions. In particular, species featuring $[\text{R}_3\text{C-H}\rightarrow\text{CR}_3]^+$ (**[5]**⁺, **[6]**⁺, **[7]**⁺),^{10,44} $[\text{R}_3\text{C-F}\rightarrow\text{CR}_3]^+$ (**[4]**⁺),⁶ $[\text{R}_3\text{Si-H-SiR}_3]^+$ (**[8]**⁺),¹² and $[\text{R}_3\text{Si-F-SiR}_3]^+$ (**[9]**⁺)¹² bridging motifs have been described (Figure 25). We now report the synthesis and characterization of a *peri*-substituted naphthalene derivative which features an agostic $\text{R}_3\text{C-H}\rightarrow\text{SiFR}_3$ σ -interaction.

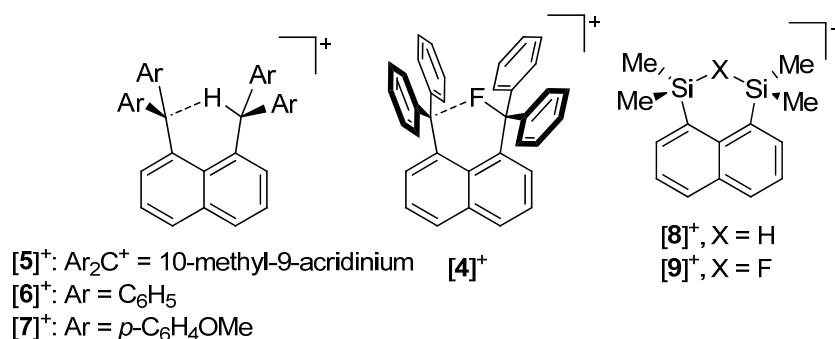


Figure 25. Structures of various bridging species.

2.3 Synthesis, structure and properties of mercury derivatives

When two equivalents of xanthone were allowed to react with one equivalent of 1,8-dilithionaphthalene, the mono-alcohol **20** was produced after aqueous work up (Figure 26). This observation suggests that the bulk of the reagent prevents attachment of a second xanthone unit. This observation also confirms that the reaction stops after the addition of one xanthone, again suggesting the intermediacy of the dilithio reagent **1**. In order to confirm this hypothesis, the reaction was repeated and quenched with methanol-

d_4 to yield **21** (Figure 26). ^1H NMR showed the absence of a single proton resonance corresponding to the 8-position of the naphthalene backbone (Figure 27). This experiment provides strong evidence for the intermediacy of **1** as an active dilithio-reagent.

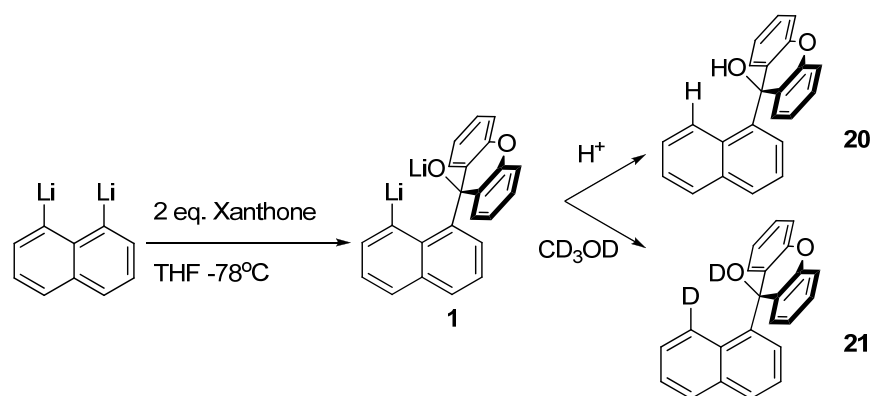


Figure 26. Deuterium quenching of **1**.

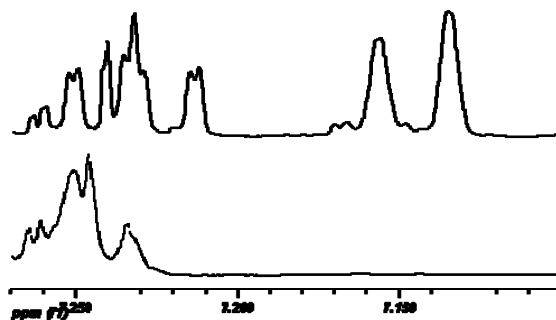


Figure 27. Stacked ^1H NMR spectra showing the resonance corresponding to the 8-position of the naphthalene backbone of **20** (top) and **21** (bottom).

To determine the ability of the dilithio intermediate **1** to produce unsymmetrical derivatives, it was generated in situ as before and allowed to react with excess HgCl_2 . Aqueous work up afforded the chloromercurio derivative **22** as a white solid (Figure 28). The appearance of a singlet at -1074 ppm in the ^{199}Hg NMR is diagnostic for mono-substituted chloromercurio derivatives such as PhHgCl (-1192 ppm in THF). Also, the ^1H NMR displays clearly resolved resonances for both the xanthenol moiety and six resonances for the unsymmetrical naphthalene backbone. Single crystals of **22** were obtained by the slow evaporation of a THF solution, and the structure was confirmed by single crystal X-ray analysis (Figure 29, Table 1).

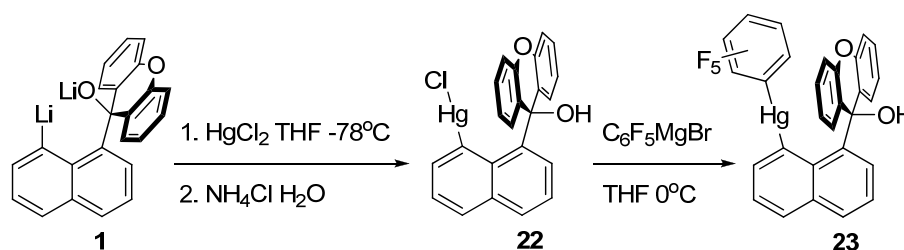


Figure 28. Synthesis of **22** and **23**.

Further reaction of **22** with (perfluorophenyl)magnesium bromide followed by recrystallization from hexane afforded the (perfluorophenyl)mercury derivative **23** as a pale brown crystalline solid (Figure 28). Major spectroscopic features of **23** include: i) three distinct resonances in the ^{19}F NMR spectrum representative of the *ortho*-, *meta*-, and *para*- fluorine atoms of the perfluorophenyl ring, ii) a triplet of triplets centered at -797 ppm in the ^{199}Hg NMR spectrum. The splitting of the ^{199}Hg NMR signal stems from the coupling of the mercury nucleus with the *ortho*- ($^3J_{\text{Hg-F}} = 380.1$ Hz) and *meta*- ($^4J_{\text{Hg-F}} = 72.1$ Hz) fluorines of the perfluorophenyl ring. ^1H NMR shows very little change in the naphthalene resonances, but a distinct upfield shift is observed for the aromatic xanthenol resonances. Structural confirmation was made by X-ray analysis of crystals obtained by the slow evaporation of a THF solution of **23** (Figure 30, Table 2).

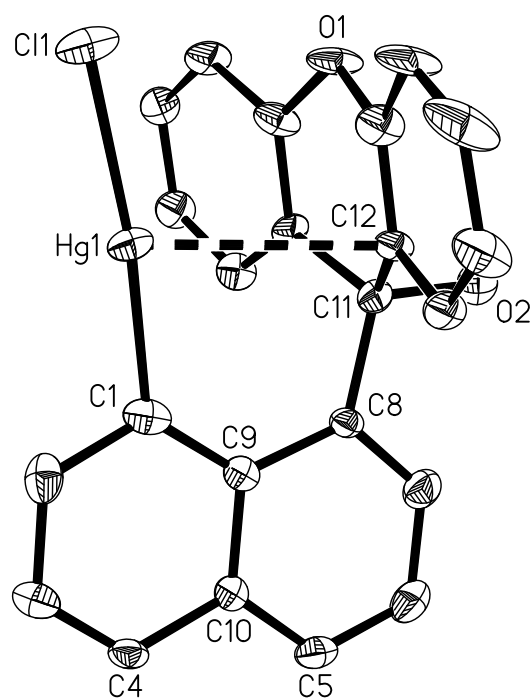


Figure 29. Crystal structure of **22** (50% ellipsoid, H-atoms omitted for clarity); selected bond lengths (Å) and angles (deg). Hg(1)-C(1) 2.061(8), Hg(1)-Cl(1) 2.324(2), Hg(1)-C(12) 3.021(8), C(8)-C(11) 1.559(11), O(2)-C(11), 1.436(10), C(11)-C(23) 1.533(11), C(11)-C(12) 1.503(11), C(12)-C(17) 1.387(11), C(12)-C(13) 1.398(10), C(1)-Hg(1)-Cl(1) 173.4(3), C(1)-Hg(1)-C(12) 83.8(3), Cl(1)-Hg(1)-C(12) 102.63(16), C(2)-C(1)-Hg(1) 109.3(6), C(9)-C(1)-Hg(1) 130.2(6), O(2)-C(11)-C(12) 105.1(6), O(2)-C(11)-C(23) 108.0(6), C(12)-C(11)-C(23) 109.7(7), O(2)-C(11)-C(8) 108.2(6), C(12)-C(11)-C(8) 112.6(6), C(23)-C(11)-C(8) 112.9(6), C(7)-C(8)-C(11) 116.2(7), C(9)-C(8)-C(11) 124.9(7).

Table 1. Crystal Data, Data Collection, and Structure Refinement for **22**·THF.

Crystal data	22 ·THF
Formula	C ₂₇ H ₂₃ O ₃ HgCl
M_r	631.49
crystal size (mm ³)	0.200 x 0.095 x 0.085
crystal system	Triclinic
space group	<i>P</i> -1
<i>a</i> (Å)	8.760(4)
<i>b</i> (Å)	9.007(5)
<i>c</i> (Å)	15.095(8)
α (°)	78.572(9)
β (°)	76.535(9)
γ (°)	73.336(8)
<i>V</i> (Å ³)	1098.5(10)
<i>Z</i>	2
ρ_{calc} (g cm ⁻³)	1.909
μ (mm ⁻¹)	7.155
<i>F</i> (000)	612
Data Collection	
<i>T</i> (K)	110(2)
scan mode	ω
<i>hkl</i> range	-11 → +11, -12 → +12, -20 → +20
measd reflns	8880
unique reflns [<i>R</i> _{int}]	5180 [0.0907]
reflns used for refinement	5180
Refinement	
refined parameters	289
GooF	1.003
R1, ^a wR2 ^b all data	0.0708, 0.1237
ρ_{fin} (max/min) (e Å ⁻³)	2.999, -2.173

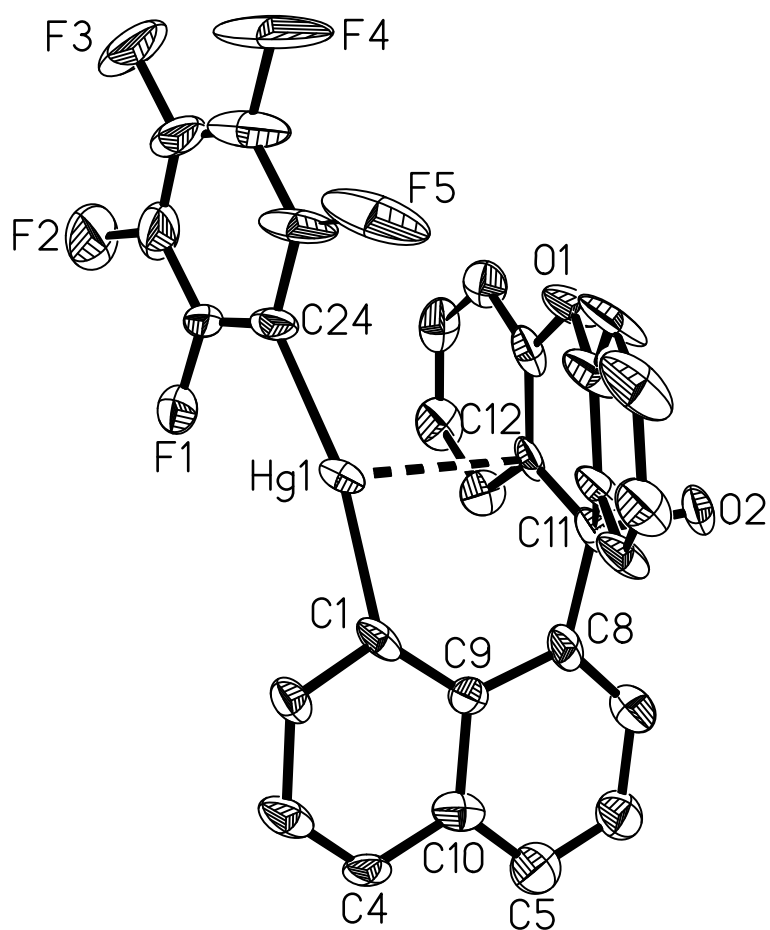


Figure 30. Crystal structure of **23** (50% ellipsoid, H-atoms omitted for clarity); selected bond lengths (Å) and angles (deg). Hg(1)-C(1) 2.058(8), Hg(1)-C(24) 2.096(9), Hg(1)-C(12) 2.940(8), F(1)-C(25) 1.346(12), F(2)-C(26) 1.38(2), F(3)-C(27) 1.339(15), F(4)-C(28) 1.330(16), F(5)-C(29) 1.355(16), O(2)-C(11) 1.474(11), C(8)-C(11) 1.524(11), C(11)-C(23) 1.509(13), C(11)-C(12) 1.517(12), C(1)-Hg(1)-C(24) 168.1(4), C(1)-Hg(1)-C(12) 87.3(3), C(24)-Hg(1)-C(12) 99.2(3), C(2)-C(1)-Hg(1) 111.5(7), C(9)-C(1)-Hg(1) 128.5(6), C(7)-C(8)-C(11) 117.9(8), C(9)-C(8)-C(11) 122.5(8).

Table 2. Crystal Data, Data Collection, and Structure Refinement for **23**·2THF.

Crystal data	23 ·2THF
Formula	C ₃₇ H ₃₁ O ₄ HgF ₅
M_r	835.21
crystal size (mm ³)	0.25 0.13 0.05
crystal system	Triclinic
space group	<i>P</i> -1
<i>a</i> (Å)	8.568(3)
<i>b</i> (Å)	9.388(3)
<i>c</i> (Å)	20.731(6)
α (°)	86.707(5)
β (°)	84.785(5)
γ (°)	70.556(5)
<i>V</i> (Å ³)	1565.4(8)
<i>Z</i>	2
ρ_{calc} (g cm ⁻³)	1.772
μ (mm ⁻¹)	4.987
<i>F</i> (000)	820
Data Collection	
<i>T</i> (K)	110(2)
scan mode	ω
<i>hkl</i> range	-9 → +9, -10 → +10, -23 → +23
measd reflns	10407
unique reflns [<i>R</i> _{int}]	4895 [0.0387]
reflns used for refinement	4895
Refinement	
refined parameters	375
GooF	1.006
R1, ^a wR2 ^b all data	0.0763, 0.1880
ρ_{fin} (max/min) (e Å ⁻³)	9.295, -1.109

Both compounds **22** and **23** crystallize in the triclinic *P*-1 space group as THF adducts (one THF for **22** and two THFs for **23**) with two molecules in the unit cell. Interestingly, the short C(12)-Hg(1) distance of 3.024 Å in **22** and C(12)-Hg(1) distance of 2.945 Å in

23 indicate the presence of secondary Hg- π interactions involving the *ipso*-carbon of one of the aryl groups. As a result, the C(1)-Hg(1)-Cl(1) ($173.3(7)^\circ$) and C(1)-Hg(1)-C(24) ($168.7(1)^\circ$) angles deviate slightly from linearity. In both the chloromercurio derivative **22** and the perfluorophenyl mercury derivative **23**, the hydroxy group of the xanthenol moiety points away from the mercury center. This conformation is unusual. For example, the hydroxyl group of 1,8-bis(diphenylmethanol)naphthalenediyl are oriented inward.⁵² The low steric requirement of the linearly coordinated mercury center as well as the formation of short Hg---C_{aromatic} interactions might be responsible for the observed structure. Unfortunately, all attempts to isolate the cationic species led to cleavage of the Hg(1)-C(1) bond.

Building on results of former graduate student, Ching-Wen Chiu, who successfully synthesized a hybrid carbocationic borane derivative by reaction of the dimesityl borate with Eschenmoser's salt, we set out to make a similar analog featuring a carbocationic moiety in place of the dimesitylboryl moiety.⁵³ Reaction of the dilithio intermediate **1** with Eschenmoser's salt leads to the formation of **24** following aqueous workup (Figure 31). Presumably, the conditions of the reaction or workup led to oxidation of the dimethylamino group affording **24**.

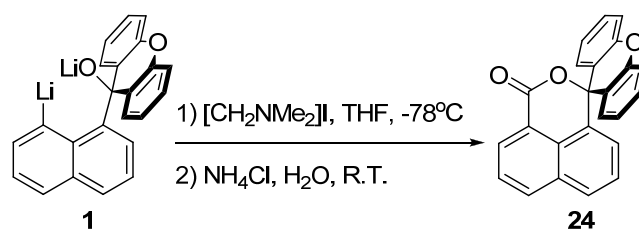


Figure 31. Synthesis of **24**.

Crystals were grown from the slow evaporation of a dichloromethane solution of **24** (Figure 32, Table 3). Compound **24** crystallizes in the $C2/c$ space group with 8 molecules in the unit cell. Examination of the structure shows that carbon C(11) is tetrahedral and bound to the oxygen atom O(2) with a bond length of $1.495(3)$ Å. The carbon atom C(24) is trigonal planar and bound to the oxygen atoms O(2) and O(3) with bond lengths of $1.348(3)$ Å and $1.210(3)$ Å, respectively. Though proof that a range of electrophiles will react with the dilithio reagent **1** compound **24** is of no particular use for the chemistry it was intended for.

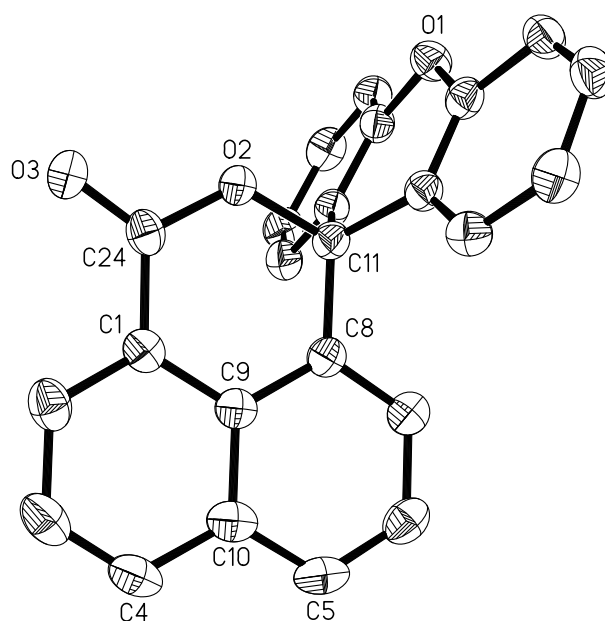


Figure 32. Crystal structure of **24** (50% ellipsoid, H-atoms omitted for clarity); selected bond lengths (Å) and angles (deg). C(1)-C(24) 1.473(4), O(2)-C(24) 1.348(3), O(2)-C(11) 1.495(3), O(3)-C(24) 1.210(3), C(8)-C(11) 1.511(3), C(11)-C(12) 1.513(4), C(11)-C(23) 1.514(4), C(24)-O(2)-C(11) 125.64(19), C(2)-C(1)-C(24) 119.5(2), C(9)-C(1)-C(24) 120.2(2), O(3)-C(24)-O(2) 117.7(2), O(3)-C(24)-C(1) 124.2(2), O(2)-C(24)-C(1) 118.1(2), O(2)-C(11)-C(8) 113.1(2), O(2)-C(11)-C(12) 103.31(19), C(8)-C(11)-C(12) 112.9(2), O(2)-C(11)-C(23) 104.09(19), C(8)-C(11)-C(23) 112.7(2), C(12)-C(11)-C(23) 109.9(2).

Table 3. Crystal Data, Data Collection, and Structure Refinement for **24-0.5(CH₂Cl₂)**.

Crystal data	24·0.5 CH₂Cl₂
formula	C _{24.50} H ₁₅ Cl O ₃
M_r	392.82
crystal size (mm ³)	0.25 0.13 0.05
crystal system	Monoclinic
space group	C ₂ /c
a (Å)	25.156(7)
b (Å)	8.609(2)
c (Å)	17.533(5)
α (°)	90
β (°)	107.244(5)
γ (°)	90
V (Å ³)	3626.3(17)
Z	8
ρ_{calc} (g cm ⁻³)	1.439
μ (mm ⁻¹)	0.235
$F(000)$	1624
Data Collection	
T (K)	110(2)
scan mode	ω
hkl range	-28 \rightarrow +27, -9 \rightarrow +9, -19 \rightarrow +13
measd reflns	8504
unique reflns [R_{int}]	2624 [0.0451]
reflns used for refinement	2624
Refinement	
refined parameters	263
GooF	1.008
R1, ^a wR2 ^b all data	0.0619, 0.1323
ρ_{fin} (max/min) (e Å ⁻³)	0.477, -0.260

2.4 Synthesis, structure and properties of silicon derivatives

Building from the aforementioned unsuccessful results, we decided to attempt the synthesis of unsymmetrical derivatives which are less sensitive towards acidolysis and oxidation. Reaction of 1,8-dilithionaphthalene⁵⁴ with xanthone followed by addition of chlorodimethylsilane subsequently afforded after aqueous work up the silyl ether **25** (Figure 34). This compound, which was isolated as a light yellow solid by recrystallization from hexane has been characterized by NMR spectroscopy and elemental analysis. The ¹H NMR spectrum of **25** corresponds to that of a C_s symmetrical molecule. Six resonances are detected for the unsymmetrically substituted naphthalenediyl backbone and four for the xanthene unit. The structure of this compound has also been determined. It crystallizes in the monoclinic P2(1)/c space group with 4 molecules per unit cell (Figure 33, Table 4). Examination of the structure confirms the connectivity proposed on the basis of the NMR spectroscopy. The molecule does not feature a mirror plane in the solid state, implying that rapid symmetrization occurs in solution on the NMR time scale. As expected, the silicon Si(1) and carbon C(11) atoms both adopt tetrahedral geometries and are bound to the bridging oxygen O(2) atom with no noticeable variation in the Si(1)-O(2) or C(11)-O(2) bond lengths from expected values. The Si(1)-C(11) separation of 2.794 Å is also unremarkable for covalently bridged *peri*-substituted naphthalene derivatives.

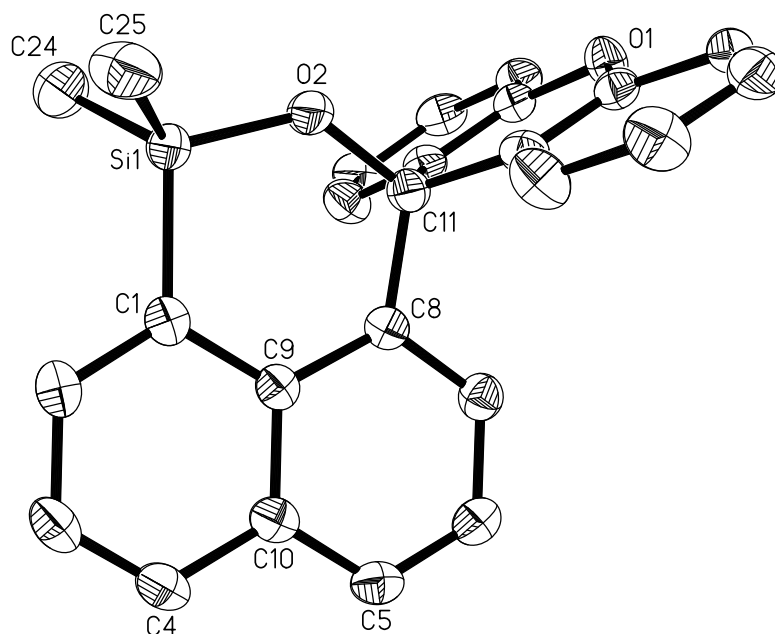


Figure 33. Crystal structure of **25** (50% ellipsoid, H-atoms omitted for clarity); selected bond lengths (Å) and angles (deg). Si(1)-O(2) 1.6325(13), Si(1)-C(24) 1.853(2), Si(1)-C(1) 1.8494(18), Si(1)-C(25) 1.853(2), O(2)-C(11) 1.4408(19), C(11)-C(23) 1.520(2), C(11)-C(12) 1.521(2), C(11)-C(8) 1.546(2), O(2)-Si(1)-C(24) 110.13(9), O(2)-Si(1)-C(1) 105.02(7), C(24)-Si(1)-C(1) 112.54(9), O(2)-Si(1)-C(25) 110.45(9), C(24)-Si(1)-C(25) 109.22(12), C(1)-Si(1)-C(25) 109.43(9), C(23)-C(11)-C(12) 109.80(13), O(2)-C(11)-C(8) 114.90(13), C(23)-C(11)-C(8) 109.36(13), C(12)-C(11)-C(8) 109.14(13), O(2)-C(11)-C(23) 106.11(13), O(2)-C(11)-C(12) 107.42(13).

Table 4. Crystal Data, Data Collection, and Structure Refinement for **25**.

Crystal data	25
formula	C ₂₅ H ₂₀ O ₂ Si
M_r	380.50
crystal size (mm ³)	0.61 x 0.30 x 0.22
crystal system	Monoclinic
space group	P2(1)/c
a (Å)	8.890(2)
b (Å)	26.996(6)
c (Å)	8.6726(19)
α (°)	90
β (°)	113.456(4)
γ (°)	90
V (Å ³)	1909.5(7)
Z	4
ρ_{calc} (g cm ⁻³)	1.324
μ (mm ⁻¹)	0.141
$F(000)$	800
Data Collection	
T (K)	110(2)
scan mode	ω
hkl range	-11 \rightarrow +9, -36 \rightarrow +34, -11 \rightarrow +11
measd reflns	14427
unique reflns [R_{int}]	4432 [0.0256]
reflns used for refinement	4432
Refinement	
refined parameters	253
GooF	1.005
R1, ^a wR2 ^b all data	0.0756, 0.1816
ρ_{fin} (max/min) (e Å ⁻³)	1.427, -0.273

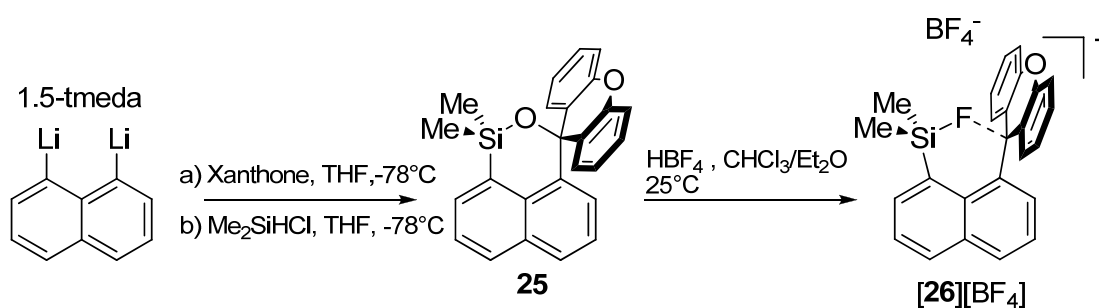


Figure 34. Synthesis of **25** and **[26][BF₄]**.

The silyl ether **25** reacts with HBF₄ aq. in a chloroform/ether mixture to afford **[26][BF₄]** as a dark red air stable salt (Figure 34). The ²⁹Si⁵⁵ NMR resonance of **[26][BF₄]** is observed as a doublet at 20.3 ppm (¹J_{Si-F} = 286 Hz). Interestingly, the fluorine atom appears to be weakly interacting with the methylum carbon atom of the xanthylum moiety whose ¹³C NMR resonance is split into a doublet (¹J_{C-F} = 6.13 Hz).

Single crystals of [26][BF₄] were obtained from acetonitrile/ether and analyzed by X-ray diffraction (Figure 35, Table 5). This salt crystallizes in the *P*-1 space group with two molecules in the unit cell. Examination of the structure of the cation [26]⁺, which is well separated from the [BF₄]⁻ anion, indicates that the fluorine atom F(1) and the methylium carbon atom C(11) are separated by 2.703(2) Å. This distance, which remains within the sum of the van der Waals radii of the two elements ($r_{\text{vdw}}(\text{F}) = 1.30 - 1.38$ Å, $r_{\text{vdw}}(\text{C}) = 1.7$ Å),^{56,57} is longer than the F→C distance of 2.444(2) Å observed in [4]⁺ and can only correspond to a very weak interaction.⁶ Moreover, the structure of [26]⁺ presents a number of features characteristic of sterically strained *peri*-substituted naphthalene derivatives. The core of the naphthalene backbone is twisted as reflected by the dihedral angle θ of 4.5° formed between the planes defined by C(1)-C(9)-C(8) and C(4)-C(10)-C(5); the C(9)-C(1)-Si(1) (133.69(12)°) and C(9)-C(8)-C(11) (123.92(15)°) angles substantially deviate from the ideal value of 120°, thus suggesting that the F(1)-C(11) interaction is enforced by the rigid naphthalenediyl linker. In agreement with the weakness of this interaction, we note that the methylium carbon atom C(11) retains a formal sp² hybridization as indicated by its trigonal planar geometry ($\Sigma_{(\text{C}-\text{C}(11)-\text{C})} = 359.91^\circ$). The Si(1)-F(1) bond of 1.609(1) Å shows no lengthening when compared to other dimethylarylfuorosilanes.⁵⁸

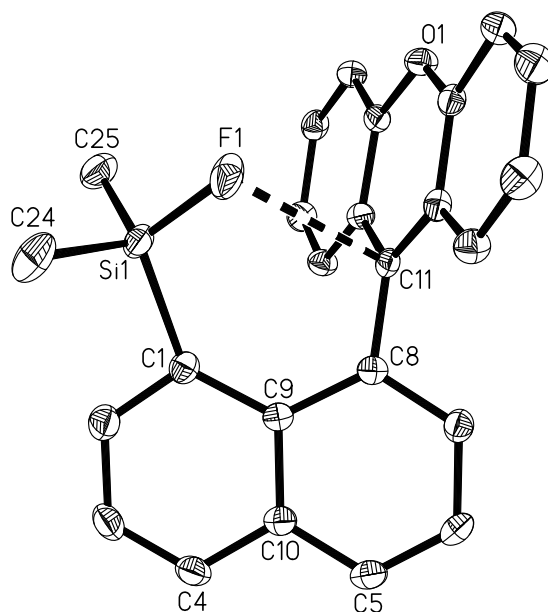


Figure 35. Crystal structure of $[26]^+$ in $[26][BF_4]$ (50% ellipsoid, H-atoms omitted for clarity); selected bond lengths (Å) and angles (deg). C(11)-C(8) 1.473(2), F(1)-C(11) 2.703(2), C(12)-C(11) 1.417(2), C(23)-C(11) 1.417(2), Si(1)-F(1) 1.6086(12), Si(1)-C(25) 1.839(2), Si(1)-C(24) 1.850(2), Si(1)-C(1) 1.8893(19), F(1)-Si(1)-C(25) 107.75(9), F(1)-Si(1)-C(24) 104.56(9), C(25)-Si(1)-C(24) 112.76(10), F(1)-Si(1)-C(1) 111.01(7), C(25)-Si(1)-C(1) 112.58(9), C(24)-Si(1)-C(1) 107.91(9), Si(1)-F(1)-C(11) 101.41(6), C(23)-C(11)-C(12) 118.30(14), C(23)-C(11)-C(8) 121.13(14), C(12)-C(11)-C(8) 120.48(13), C(23)-C(11)-F(1) 78.23(10), C(12)-C(11)-F(1) 89.79(11), C(8)-C(11)-F(1) 104.71(10), C(9)-C(1)-Si(1) 133.69(12), C(9)-C(8)-C(11) 123.92(15).

Table 5. Crystal Data, Data Collection, and Structure Refinement for [26][BF₄].

Crystal data	[26][BF ₄]
formula	C ₂₅ H ₂₀ BF ₅ OSi
M_r	470.31
crystal size (mm ³)	0.23 x 0.23 x 0.15
crystal system	Triclinic
space group	<i>P</i> -1
<i>A</i> (Å)	9.812(2)
<i>B</i> (Å)	10.112(2)
<i>C</i> (Å)	13.009(3)
α (°)	110.373(4)
β (°)	105.230(4)
γ (°)	101.512(4)
<i>V</i> (Å ³)	1105.4(4)
<i>Z</i>	2
ρ_{calc} (g cm ⁻³)	1.413
μ (mm ⁻¹)	0.164
<i>F</i> (000)	484
Data Collection	
<i>T</i> (K)	110(2)
Scan mode	ω
<i>Hkl</i> range	-13 → +8, -13 → +13, -16 → +16
measd reflns	8873
unique reflns [<i>R</i> _{int}]	5204 [0.0245]
Reflns used for	5204
Refinement	
refined parameters	298
GooF	1.007
R1, ^a wR2 ^b all data	0.0629, 0.1576
ρ_{fin} (max/min) (e Å ⁻³)	0.445, -0.289

The DFT optimized structure corresponds closely with that experimentally determined (Figure 36). The F(1)-C(11) distance of 2.66 Å is similar to that observed in the crystalline geometry. An AIM analysis of this interaction reveals a bond path between the F(1) and the C(11) atoms with an electron density $\rho(r)$ of $8.82 \times 10^{-3} \text{ e bohr}^{-3}$ at the bond critical point (BCP) (Figure 37). This value is much lower than the $2.16 \times 10^{-2} \text{ e bohr}^{-3}$ computed for $[4]^+$ and confirms the weakness of the interaction. However, an NBO analysis of the molecule indicates overlap of the empty p_z orbital of C(11) with a lone pair (lp) localized in a 2p orbital on F(1), an interaction similar to the F→C interaction described for $[4]^+$.

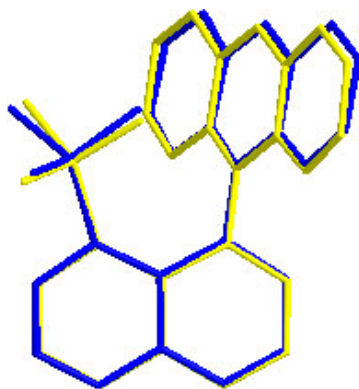


Figure 36. Overlays of the experimental (yellow) and calculated (blue) structures of $[26]^+$.

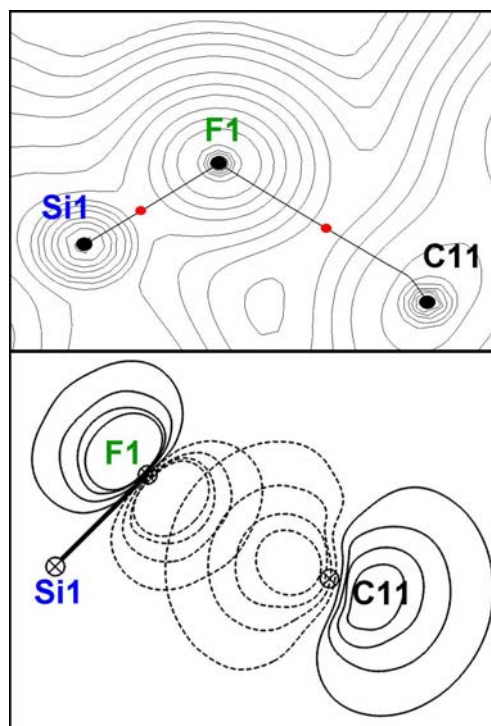


Figure 37. Top: AIM contour plot of the electron density of $[26]^+$ shown in the Si-F-C plane along with bond paths and critical points. Bottom: NBO contour plot showing the $lp_{(F)} \rightarrow p_{z(C)}$ interaction.

Reduction of $[26][BF_4]$ with $NaBH_4$ in acetonitrile leads to formation of **27** (Figure 38). Compound **27** has been isolated as an air stable solid in 70 % yield. The appearance of a singlet in the 1H NMR spectrum of **27** at 5.92 ppm provides clear spectroscopic evidence for the presence of a hydride bound to the former methylium center of the xanthene moiety. ^{29}Si NMR spectroscopy indicates that this hydride is not coupled to the silicon nucleus. Nevertheless, when compared to $[26][BF_4]$, the ^{29}Si : ^{55}Si NMR resonance of **27** at 16.4 ppm is shifted slightly upfield which could be consistent with an increase in the coordination number of the silicon center.^{55,59} This view is

supported by a measurable change of the $^1J_{\text{Si-F}}$ which decreases from 286 Hz in $[\mathbf{26}][\text{BF}_4]$ to 276 Hz in $\mathbf{27}$. Furthermore, comparing the IR stretching frequency of the central C-H bond of $\mathbf{27}$ (2928 cm^{-1}) with that of 9-(naphthalen-1-yl)-9H-xanthene (2937 cm^{-1}) indicates a weakening by 9 cm^{-1} which could be assigned to a C-H \rightarrow Si interaction.

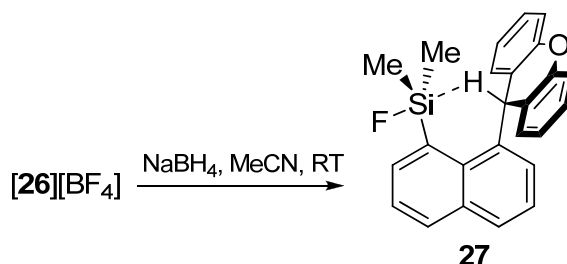


Figure 38. Synthesis of $\mathbf{27}$.

Single crystals of $\mathbf{27}$ were grown from acetonitrile and analyzed by X-ray diffraction (Figure 39, Table 6). The former methylium center C(11) is tetrahedral ($\Sigma_{(\text{C-C11-C})} = 333.2^\circ$). It is bound to the H(1) hydrogen atom which was located on the difference map and refined isotropically. According to this X-ray measurement and in good agreement with theoretical calculations (*vide infra*), the hydrogen atom H(1) is located only $2.32(2)\text{ \AA}$ away from the Si(1) silicon atom, which is well within the sum of the van der Waals radii of the two elements (ca 3.1 \AA).⁶⁰ This Si-H distance is shorter than the Si-H separation of 2.73 \AA found in $[\text{Mes}_3\text{Si}]^{+61}$ but longer than those sometimes observed in main group or transition metal complexes with silicon hydride bridges.^{12,45,60,62-67} The Si(1)-H(1) distance can also be compared to the $2.12\text{-}2.39\text{ \AA}$ range observed for the CH \rightarrow C distance of cations $[\mathbf{5}]^+$, $[\mathbf{6}]^+$ and $[\mathbf{7}]^+$.^{10,44} Another conspicuous feature concerns

the F(1)-Si(1)-H(1) angle of $177.0(5)^\circ$ which indicates that the hydrogen atom occupies an axial coordination site directly opposite from the fluorine atom. In agreement with this view, we note: i) a slight elongation of the Si(1)-F(1) bond ($1.623(1) \text{ \AA}$ vs $1.609(1) \text{ \AA}$ in $[\mathbf{26}]^+$); ii) a substantial increase in the sum of the C-Si(1)-C angles on going from $[\mathbf{26}]^+$ to $\mathbf{27}$ ($\Sigma_{\text{(C-Si1-C)}} = 345.27^\circ$ in $\mathbf{27}$ vs 333.2° in $[\mathbf{26}]^+$). While the values of the C(9)-C(1)-Si(1) ($132.55(15)^\circ$) and C(9)-C(8)-C(11) ($124.56(19)^\circ$) angles are similar to those measured in $[\mathbf{26}]^+$, the naphthalene backbone of $\mathbf{27}$ is only twisted by an angle θ of 1.0° indicating less steric crowding. Altogether, these structural results indicate the presence of a C-H \rightarrow Si agostic interaction in $\mathbf{27}$. To our knowledge, such interactions are unprecedented in the chemistry of fluorosilanes but have been observed in electrophilic silicon species such as $[i\text{-Pr}_3\text{Si}]^+$ which forms an $\sigma\text{-C-H}$ agostic interaction.⁶⁸

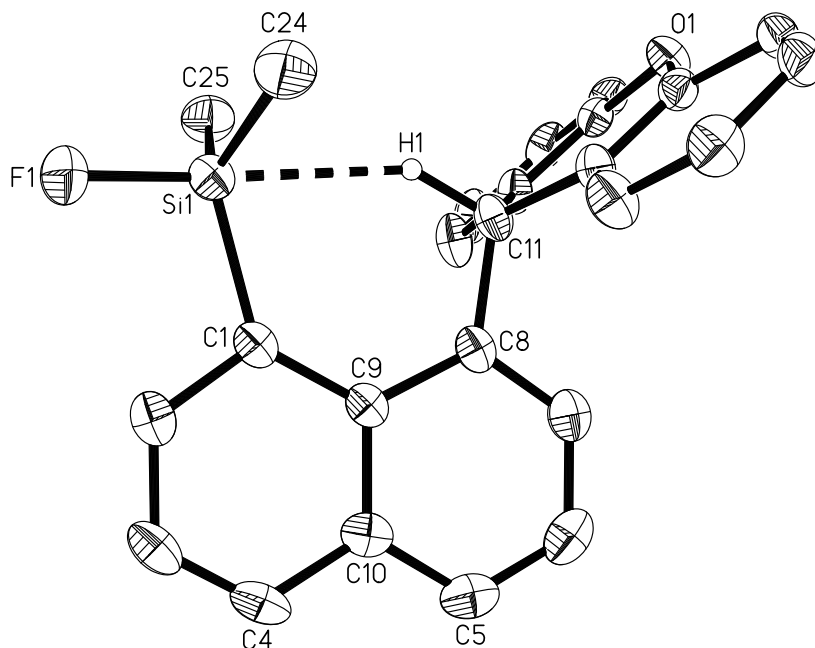


Figure 39. Crystal structure of **27** (50% ellipsoid, non-pertinent H-atoms omitted for clarity); selected bond lengths (Å) and angles (deg). Si(1)-F(1) 1.6229(14), Si(1)-C(24) 1.846(2), Si(1)-C(25) 1.847(2), Si(1)-C(1) 1.896(2), Si(1)-H(1) 2.32(2), C(11)-H(1) 1.11(2), C(11)-C(8) 1.519(3), C(11)-C(23) 1.520(3), C(11)-C(12) 1.524(3), F(1)-Si(1)-C(24) 102.47(10), F(1)-Si(1)-C(25) 102.67(9), C(24)-Si(1)-C(25) 114.69(11), F(1)-Si(1)-C(1) 103.85(8), C(24)-Si(1)-C(1) 116.66(10), C(25)-Si(1)-C(1) 113.92(10), F(1)-Si(1)-H(1) 177.0(5), C(24)-Si(1)-H(1) 75.3(5), C(25)-Si(1)-H(1) 76.8(5), C(1)-Si(1)-H(1) 79.0(5), H(1)-C(11)-C(8) 110.0(10), H(1)-C(11)-C(23) 108.0(10), C(8)-C(11)-C(23) 111.69(17), H(1)-C(11)-C(12) 105.5(10), C(8)-C(11)-C(12) 110.94(16), C(23)-C(11)-C(12) 110.56(16), C(9)-C(1)-Si(1) 132.55(15), C(9)-C(8)-C(11) 124.56(19).

Table 6. Crystal Data, Data Collection, and Structure Refinement for **27**.

Crystal data	27
Formula	C ₂₅ H ₂₁ FOSi
M_r	384.51
crystal size (mm ³)	0.21 x 0.07 x 0.04
crystal system	Triclinic
space group	<i>P</i> -1
a (Å)	8.545(2)
b (Å)	9.429(2)
c (Å)	13.712(5)
α (°)	97.067(5)
β (°)	97.216(5)
γ (°)	115.932(3)
V (Å ³)	965.9(5)
Z	2
ρ_{calc} (g cm ⁻³)	1.322
μ (mm ⁻¹)	0.144
$F(000)$	404
Data Collection	
T (K)	110(2)
scan mode	ω
hkl range	-11 \rightarrow +11, -12 \rightarrow +12, -17 \rightarrow +15
measd reflns	9564
unique reflns [R_{int}]	4458 [0.0317]
reflns used for refinement	4458
Refinement	
refined parameters	257
Goof	1.007
R1, ^a wR2 ^b all data	0.0739, 0.1356
ρ_{fin} (max/min) (e Å ⁻³)	0.595, -0.277

The DFT optimized structure corresponds closely with that experimentally determined (Figure 40). In particular, the Si(1)-H(1) separation of 2.32 Å is close to that observed in the crystal. AIM calculations, which have proved useful for the characterization of agostic interactions in d^0 metal alkyl complexes,⁶⁹ show the presence of a bond path between the Si(1) and the H(1) atoms with an electron density $\rho(r)$ of $1.68 \times 10^{-2} \text{ e bohr}^{-3}$ at the bond critical point (BCP) (Figure 41). This value which is much weaker than those computed for the Si-H bonds of PhMe_2SiH ($11.53 \times 10^{-2} \text{ e bohr}^{-3}$) and $[\mathbf{9}]^+$ (av. $7.44 \times 10^{-2} \text{ e bohr}^{-3}$) reveals the presence of a relatively weak interaction. Nevertheless, its presence can be further asserted through an NBO analysis performed at the B3LYP optimized geometry. This analysis identifies a donor-acceptor interaction involving the C-H σ -bond as a donor and the silicon empty p_z -orbital as the acceptor. It is also important to note that this NBO analysis describes the Si-F bond as a donor-acceptor interaction involving a fluorine lone pair as the donor and the silicon empty p_z -orbital as the acceptor. Hence, the silicon center in **27** bears the bonding characteristic of a five coordinate silicon species such as $[\text{PhSiMe}_2\text{F}_2]^-$ where both axial fluoride ligands compete for a unique silicon p -orbital (Figure 42).

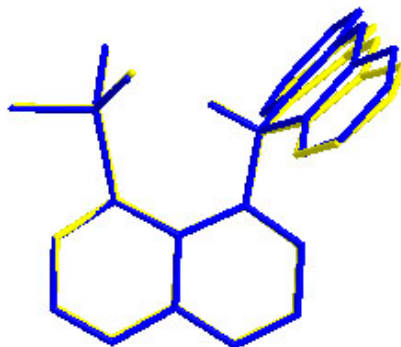


Figure 40. Overlay of the experimental (yellow) and calculated (blue) structures of **27**.

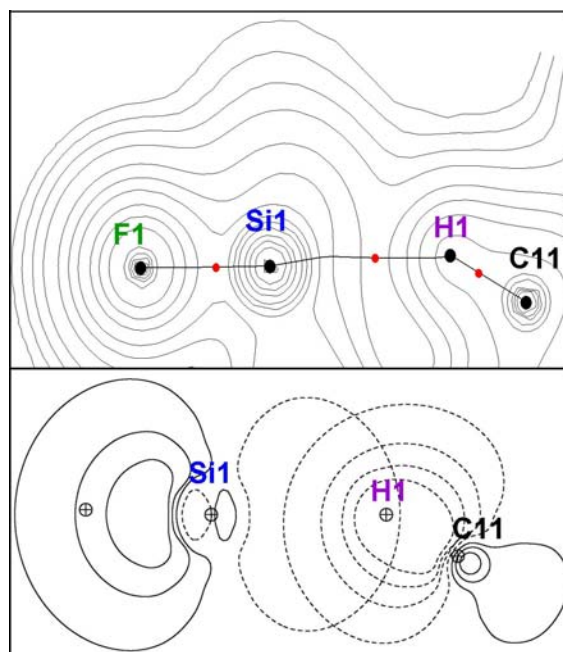


Figure 41. Top: AIM contour plot of the electron density of **27** shown in the F(1)-Si(1)-H(1)-C(11) plane along with bond paths and critical points. Bottom: NBO contour plot showing the $\sigma_{C-H} \rightarrow p_z(Si)$ interaction.

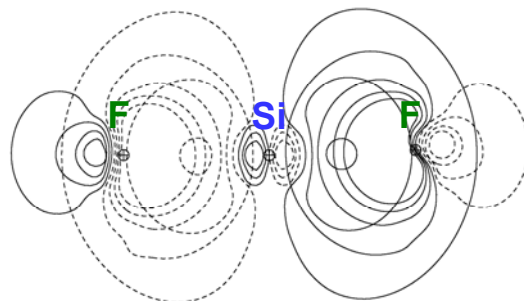
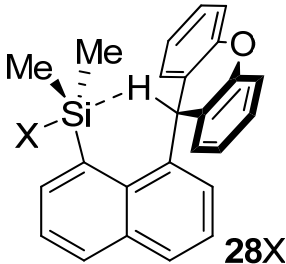


Figure 42. NBO contour plot showing the donor acceptor interactions between the fluoride lone pairs and the silicon empty p orbitals in $[\text{PhMe}_2\text{SiF}_2]^-$

Further insights into the nature of the interaction were gained from a computational survey of a series of molecules in which the fluorine atom of **27** is substituted by a group X (X = CH₃, NH₂, OH). As shown in Table 7 Si(1)-H(1) distance decreases as the Lewis acidity of the silicon center increases. This shortening is also accompanied by an increase of $\rho(r)$ at the BCP. These computational results further substantiate the presence of a donor-acceptor R₃C-H→SiFR₃ interaction in **27**. Lastly, a deletion calculation carried out by zeroing the Kohn-Sham matrix elements corresponding to the $\sigma_{(\text{C-H})} \rightarrow p_{z(\text{Si})}$ interaction leads to an increase of the total energy of the molecule by 3.069 kcal/mol. This deletion calculation suggest that the $\sigma_{(\text{C-H})} \rightarrow p_{z(\text{Si})}$ interaction is comparable in energy to a moderately strong hydrogen bond.⁷⁰ This interaction is weaker than classical agostic interactions because of the absence of back-bonding.

Table 7. Computed metrical parameters and electron density for molecules **27** and **28X**.

Cpd	Si(1)-H(1) (Å)	$\Sigma_{(C-Si-C)}$ (°)	$\rho(r)@BCP$ (e bohr ⁻³)	
28CH₃	2.40	340.2	1.55×10^{-2}	
28NH₂	2.40	340.9	1.52×10^{-3}	
28OH	2.36	343.7	1.60×10^{-2}	
27	2.32	346.8	1.68×10^{-2}	

Subsequent reduction of **27** with LiAlH₄ in refluxing THF overnight affords **29** (Figure 43). The ¹H NMR of **29** confirms formation of a silicon hydride species as evidenced by the appearance of a multiplet at 5.95 ppm. This multiplet is consistent with coupling to two inequivalent methyl groups on the silicon center. The methyl resonance at 0.48 ppm again appears as a doublet as before, but a noticeable decrease in the methyl coupling constant from 8.49 Hz in **27** to 4.99 Hz in **29** as well as an upfield shift of the ²⁹Si{¹H} signal to -1.86 ppm also confirm substitution of the fluoride in **27** for a hydride in **29**. Recrystallization from acetonitrile afforded crystals of **29** (Figure 44, Table 8). Examination of the solid state structure of **29** confirms that proposed by NMR. Indeed, the methyl groups C(24) and C(25) on the silicon center Si(1) are locked into two unique environments due to the hydrogen atom H(2) being located in an endo fashion with respect to the naphthalene backbone.

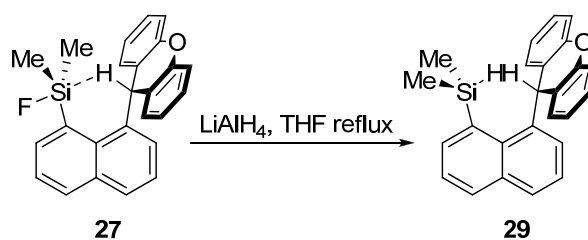


Figure 43. Synthesis of **29**.

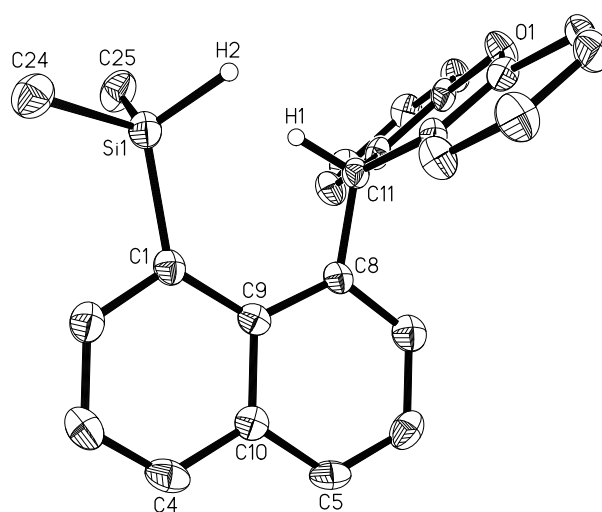


Figure 44. Crystal structure of **29** (50% ellipsoid, non-pertinent H-atoms omitted for clarity); selected bond lengths (Å) and angles (deg). Si(1)-C(25) 1.866(3), Si(1)-C(24) 1.870(3), Si(1)-C(1) 1.896(3), Si(1)-H(2) 1.46(2), C(8)-C(11) 1.533(4), C(11)-H(1) 1.02(2), C(25)-Si(1)-C(24) 109.41(15), C(25)-Si(1)-C(1) 110.57(14), C(24)-Si(1)-C(1) 110.22(15), C(25)-Si(1)-H(2) 109.8(8), C(24)-Si(1)-H(2) 104.0(8), C(1)-Si(1)-H(2) 112.7(8), C(2)-C(1)-Si(1) 111.7(2), C(9)-C(1)-Si(1) 130.5(3), C(23)-C(11)-C(12) 111.2(3), C(23)-C(11)-C(8) 112.8(3), C(12)-C(11)-C(8) 110.8(3), C(23)-C(11)-H(1) 108.5(13), C(12)-C(11)-H(1) 104.7(13), C(8)-C(11)-H(1) 108.5(14), C(7)-C(8)-C(11) 114.7(3), C(9)-C(8)-C(11) 124.9(3).

Table 8. Crystal Data, Data Collection, and Structure Refinement for **29**.

Crystal data	29
formula	C ₂₅ H ₂₂ OSi
M_r	366.52
crystal size (mm ³)	0.11 x 0.09 x 0.08
Crystal system	Triclinic
Space group	<i>P</i> -1
<i>a</i> (Å)	8.7016(17)
<i>b</i> (Å)	8.7208(17)
<i>c</i> (Å)	14.717(3)
<i>A</i> (°)	94.14(3)
<i>β</i> (°)	101.13(3)
<i>Γ</i> (°)	116.62(3)
<i>V</i> (Å ³)	963.5(3)
<i>Z</i>	2
ρ_{calc} (g cm ⁻³)	1.263
μ (mm ⁻¹)	0.134
<i>F</i> (000)	388
Data Collection	
<i>T</i> (K)	110(2)
scan mode	ω
<i>hkl</i> range	-9 → +9, -9 → +9, -16 → +16
measd reflns	6477
unique reflns [<i>R</i> _{int}]	2723 [0.0567]
reflns used for refinement	2723
Refinement	
refined parameters	252
GooF	1.007
R1, ^a wR2 ^b all data	0.1168, 0.0860
ρ_{fin} (max/min) (e Å ⁻³)	0.526, -0.622

Upon addition of one equivalent of TASF to a solution of **[26]**⁺ in CDCl₃, remarkable changes are observed. The red solution immediately loses color indicating quaternization of the methylium carbon atom. The ¹H NMR of the resulting solution indicates that symmetrization also occurs about the naphthalene backbone (Figure 45). One possible explanation for this is the formation of **30** (Figure 46). Attempts to isolate this species have proven to be difficult due to its sensitivity, but it might also be useful as a reagent for the preparation of unsymmetrical derivatives that are difficult via other routes.

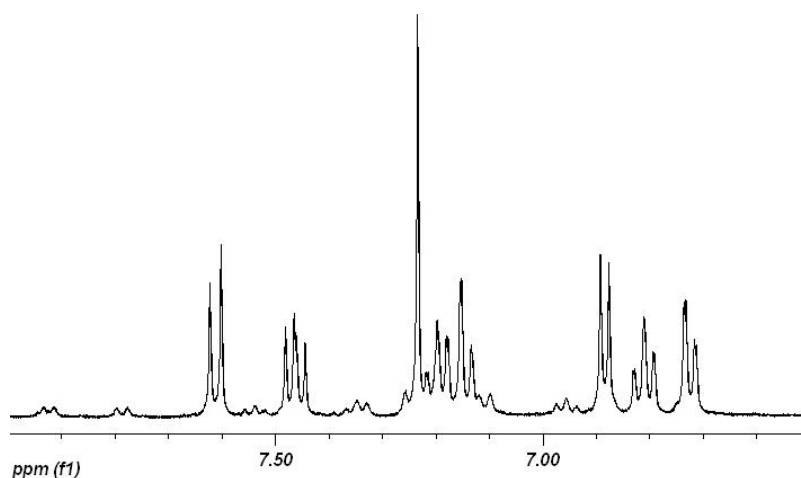


Figure 45. NMR spectra of **30**.

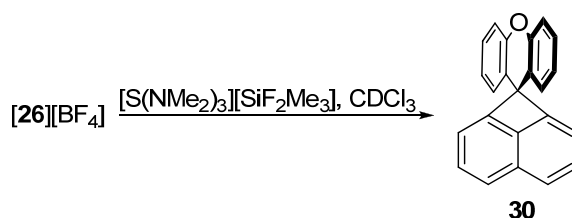


Figure 46. Synthesis of **30**.

2.5 Conclusions

In conclusion, the dilithio derivative **1** has been shown to be a useful way to access unsymmetrical derivatives on the 1,8-naphthalenediyl scaffold. This has been shown in its ability to react with various main group electrophiles. We also report the synthesis and structural characterization of a compound featuring an agostic $R_3C-H \rightarrow SiFR_3$ interaction. Formation of this interaction is made possible by the use of the naphthalene backbone which holds the interacting functionalities in close proximity. Despite its weakness, the presence of this interaction is indubitable and notably affects the geometry of the silicon center which adopts a distorted trigonal bipyramidal geometry. Furthermore, the instability of **30** provides hope that it might be a useful reagent for the synthesis of unsymmetrical derivatives.

2.6 Experimental

Calculations. Density functional theory (DFT) calculations (full geometry optimization) were carried out with *Gaussian03* using the gradient-corrected Becke exchange functional (B3LYP) and the Lee-Yang-Parr correlation functional. A 6-

31+g(d') basis set was used for all oxygen and fluorine atoms as well as any carbon and hydrogen atoms involved in bridging interactions. A 6-31+g(d) basis set was used for silicon, and a 6-31g basis set was used for all remaining carbon and hydrogen atoms. Frequency calculations, which were carried out on the optimized structure of each compound, confirmed the absence of any imaginary frequencies. The electron density of the DFT-optimized structures of [26]⁺ and 27 were subjected to an Atoms-In-Molecules (AIM) analysis using AIM2000. Natural Bond Order (NBO) analyses of the DFT optimized geometries were visualized using the NBO View PC suite.

Synthesis of 22. A solution of xanthone (0.82 g, 4.17 mmol) in THF (20 mL) was added to a solution of 1,8-dilithionaphthalene (1.05 g, 4.09 mmol) in THF (10 mL) at -78°C. After stirring for 30 min. at -78°C, mercuric chloride (1.55 g, 5.71 mmol) dissolved in THF (10mL) was added to the orange suspension. The resulting dark green solution was stirred at -78°C for one hour before it was allowed to warm to room temperature where stirring was continued for another hour. The solution was quenched with 5% NH₄Cl_{aq} (15 mL), the white precipitate filtered from the yellow solution, and washed with H₂O, EtOH, and hexane. The resulting powder was dried under vacuum to afford 22 as a white solid. Yield: 85% (1.95 g). Single crystals of 22 suitable for X-ray structural analysis were obtained by slow evaporation of a THF solution. ¹H NMR (CDCl₃): δ 2.24 (s, 1 H, COH), δ 6.018 (d, J = 7.19 Hz, 2 H, CH_{xan}), δ 6.95 (pseudo t, J_{apparent} = 6.4 Hz, 2 H, CH_{xan}), δ 7.11 (d, J = 5.59 Hz, 1 H, CH_{naph}), δ 7.308 (t, J = 6.79 Hz, 1 H, CH_{naph}), δ 7.47 (m, 4 H, CH_{xan}), δ 7.72 (t, J = 7.89 Hz, 1 H, CH_{naph}), δ 7.93 (d, J = 7.99 Hz, 1 H, CH_{naph}),

δ 8.03 (d, $J = 7.99$ Hz, 1 H, CH_{naph}), δ 8.69 (d, $J = 7.19$ Hz, 1 H, CH_{naph}); ^{13}C NMR (CDCl_3): CH_{xan} : δ 119.0, 124.2, 127.3, 130.9; Quat C_{xan} : δ 126.5, 136.9; COH_{xan} : δ 72.3; CH_{naph} : δ 123.8, 125.1, 129.8, 131.2, 132.1, 136.6; Quat C_{naph} : δ 151.8 others not observed due to solubility; ^{199}Hg (CDCl_3): δ -1074.5; Decomposes above 270°C

Synthesis of 23. Perfluorophenyl Grignard (1.96g, 7.24 mmol) in THF (20mL) was added to a stirred suspension of **1** (1.0 g, 1.44 mmol) in THF (20 mL) at 0°C . After 5 minutes, the resulting brown suspension was allowed to warm to room temperature where it was stirred for another 2 hours. The solution was quenched with 5% NH_4Cl (15 mL), the organic phase extracted with diethyl ether (2 x 15 mL), dried with MgSO_4 , and concentrated. Recrystallization from hexane yielded **23** as a light brown solid. Yield: 95% (0.94 g). Single crystals of **23** suitable for X-ray structural analysis were obtained by slow evaporation of a THF solution. ^1H NMR (CDCl_3): δ 2.14 (s, 1 H, OH), δ 6.78 (d, $J = 7.59$ Hz, 2 H, CH_{xan}), δ 6.99 (t, $J = 7.59$ Hz, 2 H, CH_{xan}), δ 7.08 (d, $J = 8.39$ Hz, 2 H, CH_{xan}), δ 7.16 (d, $J = 5.79$ Hz, 1 H, CH_{naph}), δ 7.38 (m, 3 H, $CH_{\text{xan}} + CH_{\text{naph}}$), δ 7.71 (t, $J = 7.59$ Hz, 1 H, CH_{naph}), δ 7.92 (d, $J = 8.19$ Hz, 1 H, CH_{naph}), δ 8.05 (d, $J = 7.19$ Hz, 1 H, CH_{naph}), δ 8.62 (d, $J = 7.19$ Hz, 1 H, CH_{naph}); ^{13}C NMR (CDCl_3): CH_{xan} : δ 117.8, 124.2, 127.5, 130.6; Quat C_{xan} : δ 126.5, 151.5; COH_{xan} : δ 72.6; CH_{naph} : δ 123.7, 124.9, 129.5, 130.7, 131.9, 136.5; Quat C_{naph} : δ 136.6, 136.8, 136.9, 163.9; CF: δ 136.2 (br s), 138.8 (br s), 139.3 (br s), 141.8 (br s), 146.2 (br s), 148.5 (br s); ^{199}Hg (CDCl_3): δ -797.5 (tt, $^3J_{\text{Hg-F}} = 380.1$ Hz, $^4J_{\text{Hg-F}} = 72.1$ Hz); ^{19}F NMR (CDCl_3): δ -117.35

(m, 2F, F_{ortho}), δ -153.9 (t, ${}^3J_{F-F} = 19.5$ Hz, 1 F, F_{para}), δ -160.8 (m, 2 F, F_{meta}); Melting point: 163-165°C.

Synthesis of 24. A solution of xanthone (0.08g, 0.40 mmol) in THF (20mL) was added to a solution of 1,8-dilithionaphthalene (0.10g, 0.39 mmol) in THF (5 mL) at -78°C. After 30 min, addition of Eschenmoser's salt (0.07 g, 0.39 mmol) in THF (15 mL) was added to the red orange suspension and the resulting yellow solution was stirred at -78°C for another 2 hours and warmed to room temperature. The solution was quenched with a saturated NH_4Cl solution (15 mL), extracted with ether, dried with $MgSO_4$ and evaporated under reduced pressure. Evaporation of a dichloromethane solution of **24** afforded single crystals suitable for X-ray structural analysis.

Synthesis of 25. A solution of xanthone (0.77g, 4.01 mmol) in THF (20mL) was added to a solution of 1,8-dilithionaphthalene (1.01g, 3.90 mmol) in THF (5 mL) at -78°C. After 30 min, addition of dimethylchlorosilane (0.50 mL, 4.50 mmol) to the resulting red-orange suspension resulted in a yellow solution which was stirred at -78°C for 1 h and warmed to room temperature. The solution was then quenched with a saturated aqueous NH_4Cl solution (15 mL), extracted with ether (2 x 15 mL) and evaporated under reduced pressure. Recrystallization from hexane yielded **25** as a pale yellow solid. Yield: 80% (1.19 g). 1H NMR ($CDCl_3$, 400 MHz): δ 0.41 (s, 6 H, CH_{Me}), δ 6.91 (m, 3 H, CH), δ 7.14 (d, 2 H, CH_{Xan} , ${}^3J_{H-H} = 7.99$ Hz), δ 7.24 (m, 5 H, CH), δ 7.58 (t, 1 H, CH_{Naph} , ${}^3J_{H-H} = 7.19$), δ 7.74 (m, 2H, CH), δ 7.96 (d, 1 H, CH_{Naph} , ${}^3J_{H-H} = 8.39$ Hz). ${}^{13}C$

NMR (CDCl₃, 100.5 MHz): δ 1.66, 75.48, 116.59, 123.05, 125.01, 125.29, 127.81, 128.63, 128.82, 129.62, 130.06, 130.45, 131.30, 131.69, 132.87, 134.17, 142.94, 149.08. ²⁹Si NMR (CDCl₃, 79.4 MHz): δ 0.03. Elemental analysis calcd. (%) for C₂₅H₂₀O₂Si: C 78.91, H 5.30; found: C 79.05, H 5.34. Melting point: 256-258°C.

Synthesis of [26][BF₄]. Tetrafluoroboric acid (40 % in H₂O, 2 mL) was added to a solution of **25** (0.50 g, 1.32 mmol) in diethyl ether (10 mL). The suspension was shaken in a separatory funnel for 10 min. The resulting deep red mixture was extracted with chloroform (2 x 10 mL). Evaporation of the resulting organic phase afforded a dark red solid which was washed with ether (2 x 10 mL) to yield [26][BF₄] as a dark red air and water stable solid. Yield: 90 % (0.55 g). ¹H NMR (CDCl₃, 400 MHz): δ -0.22 (d, 6 H, CH_{Me}, ³J_{H-F} = 7.59 Hz), δ 7.61 (t, 1 H, CH_{Naph}, ³J_{H-H} = 7.59 Hz), δ 7.73 (d, 1 H, CH_{Naph}, ³J_{H-H} = 6.39 Hz), δ 7.79 (t, 2 H, CH_{Xan}, ³J_{H-H} = 7.59 Hz), δ 7.83 (m, 4 H, CH), δ 8.18 (d, 1 H, CH_{Naph}, ³J_{H-H} = 6.79 Hz), δ 8.29 (d, 1 H, CH_{Naph}, ³J_{H-H} = 6.39 Hz), δ 8.41 (d, 2 H, CH_{Xan}, ³J_{H-H} = 8.39 Hz), δ 8.47 (t, 2 H, CH_{Xan}, ³J_{H-H} = 6.79 Hz). ¹³C NMR (CDCl₃, 100.5 MHz): δ 0.51 (d, ²J_{C-F} = 15.77 Hz), 120.23, 124.99 (d, ²J_{C-F} = 4.52 Hz), 125.56, 126.24 (d, ³J_{C-F} = 2.11 Hz), 128.99, 129.78, 131.78, 132.67, 133.46, 133.63, 134.23, 134.79, 135.17, 137.66 (d, ³J_{C-F} = 5.63 Hz), 143.77, 158.55, 176.68 (d, ¹J_{C-F} = 6.13 Hz). ¹⁹F NMR (CDCl₃, 375 MHz): -154.27 (s, ¹¹BF₄), -154.21 (s, ¹⁰BF₄), -144.95 (sept, ³J_{F-H} = 7.51 Hz). ²⁹Si{¹H} NMR (CDCl₃, 79.3 MHz): δ 20.3 (d, ¹J_{Si-F} = 286 Hz). Elemental analysis calcd. (%) for C₂₅H₂₀BF₅OSi: C 63.84, H 4.29; found: C 63.79, H 4.30. Melting point: 325-327°C.

Synthesis of 27. Sodium borohydride (0.1 g, 2.64 mmol) was added to a solution of [26][BF₄] (0.75 g, 1.06 mmol) in acetonitrile (10 mL) and stirred until the red color had dissipated. The solvent was evacuated and the solid extracted with diethyl ether (3 x 10 mL). The resulting solution was concentrated and recrystallized from acetonitrile to yield **27** as a yellow crystalline solid. Yield: 70% (0.28 g). ¹H NMR (CDCl₃, 500 MHz): δ 0.45 (d, 6 H, CH_{Me}, ³J_{H-F} = 8.49 Hz), δ 5.92 (s, 1H, CH_{Xan}), δ 6.64 (d, 2 H, CH_{Xan}, ³J_{H-H} = 7.99 Hz), δ 6.83 (t, 2 H, CH_{Xan}, ³J_{H-H} = 6.99 Hz), δ 7.12 (d, 2 H, CH_{Xan}, ³J_{H-H} = 8.49 Hz), δ 7.18 (t, 2 H, CH_{Xan}, ³J_{H-H} = 7.99 Hz), δ 7.35 (d, 1 H, CH_{Naph}, ³J_{H-H} = 6.99 Hz), δ 7.42 (t, 1 H, CH_{Naph}, ³J_{H-H} = 7.49 Hz), δ 7.55 (t, 1 H, CH_{Naph}, ³J_{H-H} = 8.99 Hz), δ 7.83 (d, 1 H, CH_{Naph}, ³J_{H-H} = 7.75 Hz), δ 8.02 (d, 1 H, CH_{Naph}, ³J_{H-H} = 7.99 Hz), δ 8.19 (d, 1 H, CH_{Naph}, ³J_{H-H} = 6.99 Hz). ¹³C NMR (CDCl₃, 125.7 MHz): δ 1.43 (d, ²J_{C-F} = 17.59 Hz), 41.29 (d, ³J_{C-F} = 3.01 Hz), 116.18, 122.91, 124.66 (d, ³J_{C-F} = 1.50 Hz), 124.79, 126.00, 127.97, 129.32, 130.10, 131.54 (d, ³J_{C-F} = 9.17 Hz), 132.19, 132.84, 134.45, 136.46 (d, ³J_{C-F} = 12.19 Hz), 137.31, 143.41, 151.09. ¹⁹F NMR (CDCl₃, 375.9 MHz): -148.98 (sept., ³J_{F-H} = 7.89). ²⁹Si{¹H}NMR (CDCl₃, 79.4 MHz): 16.42 (d, ¹J_{Si-F} = 276 Hz). Elemental analysis caclcd. (%) for C₂₅H₂₁FOSi: C 78.09, H 5.50; found C 78.22, H 5.51. Melting point: 190-192°C. IR: 2928 cm⁻¹.

Synthesis of 29. LiAlH₄ (0.020 g, 0.52 mmol) was added to a solution of **27** (0.20 g, 0.52 mmol) in acetonitrile (5 mL), and the suspension stirred overnight at room temperature. The suspension was filtered and the acetonitrile removed under reduced pressure to yield two isomers. Washing of the mixture with acetonitrile (1 mL) afforded pure **29**. Yield: 40% (0.076 g). Single crystals of **29** were grown from slow evaporation of an acetonitrile solution. ¹H NMR (CD₃CN, 500 MHz): δ 0.49 (d, 6 H, CH_{Me}, ³J_{H-F} = 3.99 Hz), δ 4.98 (m, 1H, CH_{Si}), δ 6.60 (s, 1H, CH_{Xan}), δ 6.75 (d, 2 H, CH_{Xan}, ³J_{H-H} = 6.99 Hz), δ 6.90 (t, 2 H, CH_{Xan}, ³J_{H-H} = 7.99 Hz), δ 7.18 (d, 2 H, CH_{Xan}, ³J_{H-H} = 7.99 Hz), δ 7.24 (t, 2 H, CH_{Xan}, ³J_{H-H} = 6.99 Hz), δ 7.43 (t, 1 H, CH_{Naph}, ³J_{H-H} = 6.99 Hz), δ 7.59 (t, 1 H, CH_{Naph}, ³J_{H-H} = 6.99 Hz), δ 7.88 (d, 1 H, CH_{Naph}, ³J_{H-H} = 8.49 Hz), δ 8.08 (m, 2 H). ¹³C NMR (CD₃CN, 125.7 MHz): δ -0.92, 40.83, 117.07, 124.03, 125.77, 126.06, 126.74, 129.02, 129.99, 130.97, 132.61, 132.95, 133.55, 138.42, 146.68, 151.56. ²⁹Si{¹H}NMR (CD₃CN, 99.3 MHz): -1.86.

CHAPTER III

SYNTHESIS AND REDOX PROPERTIES OF BORATA-ALKENES

3.1 Background

3.1.1 Carbon centered radicals

It has been known for some time now that carbon-based radicals can be stabilized by attaching pendant aromatic substituents. The simplest form of these radicals is the triphenylmethyl (trityl) radical **31**.^{71,72} This radical can be produced from the oxidation of substituted triphenylmethanes or by the electrochemical reduction of the triphenylmethyl cation. Unfortunately, it dimerizes in a head to tail fashion and is unstable in solution (Figure 47).

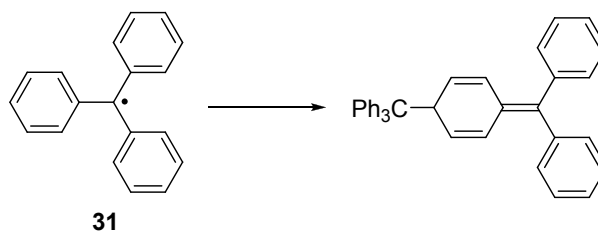


Figure 47. Dimerization of **31**

Chichibabin's hydrocarbon **32** and Thiele's hydrocarbon **33** both exhibit partial diradical character at room temperature in solution (Figure 48). This character is brought about by the central phenylene linkers whose aromaticity lowers the energy of

the radical. The singlet/triplet energy gap for this process is low (2-10 kcal mol⁻¹). Also, on increasing the number of phenylene linkers from one to two, the amount of diradical character increases. This is evidenced by the stability of each derivative in solution. Derivative **33** readily decomposes in aerated solutions whereas **32** has a much slower rate of decomposition. These species can be handled as solids in air with no apparent decomposition whereas the triphenylmethyl radical **31** is much more reactive.

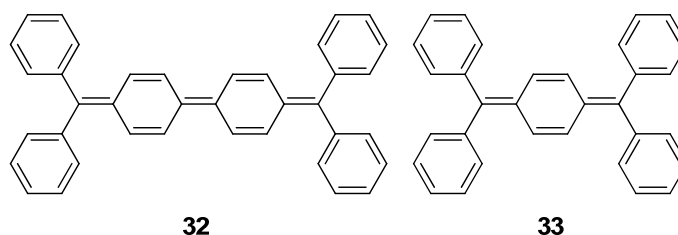


Figure 48. Chichibabin's hydrocarbon **32** and Thiele's hydrocarbon **33**

3.1.2 Triarylboryl radicals

Boron centered radicals have been studied extensively recently due to their isoelectronic relationship with the aforementioned carbon centered radicals. These radicals tend to be much more reactive because of the formal negative charge on the species however. For example, the triphenylboryl radical dimerizes in the same fashion as the triphenylmethyl radical. By substituting the phenyl groups for mesityl substituents, such triarylboryl radicals can be stabilized and isolated in the solid state. In fact, the trimesitylboryl radical anion **34** has been isolated by reduction of trimesitylborane with sodium and its structure determined by X-ray crystallography

(Figure 49).¹⁹ The central boron atom remains planar with only slight deviations of the C-B-C angles from 120°. Also, there is a very slight increase of the B-C bond lengths (0.02 Å) when compared to those of trimesityl borane. This can be ascribed to the degree of delocalization of the radical throughout the system. EPR spectroscopy of the trimesitylboryl radical anion shows hyperfine coupling to boron ($a(^{11}\text{B}) = 9.87 \text{ G}$) in THF which helps to confirm the delocalization of the radical. This value can be compared to a more boron centered radical such as $[\text{B}(\text{tBu})_3]^{\cdot-}$ which has been shown to have a ^{11}B coupling of 38.5 G.

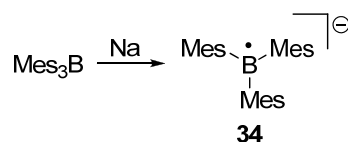


Figure 49. Synthesis of **34**

Dianion $[\mathbf{35}]^{2-}$ constitutes the boron based analog of Thiele's hydrocarbon **33** (Figure 50).⁷³ Cyclic voltammetry of **35** shows two reversible one electron processes to the radical anion $[\mathbf{35}]^{\cdot-}$ (-1.39 V vs. SCE) and dianion $[\mathbf{35}]^{2-}$ (-2.08 V vs. SCE), respectively. EPR spectroscopy of the radical anion $[\mathbf{35}]^{\cdot-}$ reveals an extremely complicated spectrum presumably due to the high degree of delocalization of the radical throughout the system. Unlike Thiele's hydrocarbon **33**, the dianion $[\mathbf{35}]^{2-}$ shows no EPR signal indicating a diamagnetic quinone type structure.

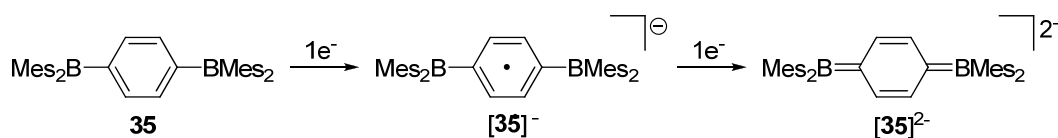


Figure 50. One and two electron reduction processes of **35**

3.1.3 Alkenyl radicals

For some time now, it has been known that tetraarylethylene derivatives can be oxidized and reduced in a reversible manner to afford the formal α -dications and radical cations.⁴³ One such series is the **36**/[**36**]^{•+}/[**36**]²⁺ series in which the aryl substituents are anisyl groups (Figure 51). Oxidation of **36** with triethyloxonium hexachloroantimonate yields the radical cation [**36**]^{•+} while oxidation of **36** with antimony pentachloride yielded the dication [**36**]²⁺. Each species has been structurally characterized by X-ray crystallography. First, it is important to note that the central ethylene unit shows a drastic change in bond length upon successive oxidation. The formal alkene **36** has a central ethylene bond length of 1.359 Å while that in the radical cation [**36**]^{•+} is 1.417 Å and the formal dication [**36**]²⁺ is 1.503 Å. Furthermore, there is a significant distortion in the torsion angle about the central bond from 3.8° in **36** to 30.5° in [**36**]^{•+} and 61.6° in [**36**]²⁺. This change further supports the formation of a one electron π -bond in [**36**]^{•+} and a single bond in [**36**]²⁺.

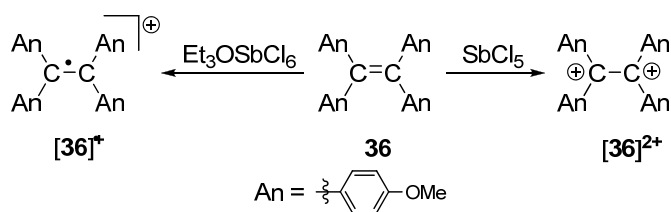


Figure 51. Oxidation processes of **36**

3.1.4 Borata-alkenes and their radicals

The Power group has long been interested in compounds where one or more of the carbon atoms in an alkene is substituted by a boron atom. In 1986, their group successfully structurally characterized one of the first examples of a boron stabilized carbanion or borata-alkene.⁷⁴ Deprotonation of Mes_3B with $n\text{-BuLi}$ provides $[37]^-$ as the $[\text{Li}(12\text{-crown-4})]^+$ salt (Figure 52). The anion $[37]^-$ shows significant B-C double bond character with a B-C bond length of 1.522(10) Å.

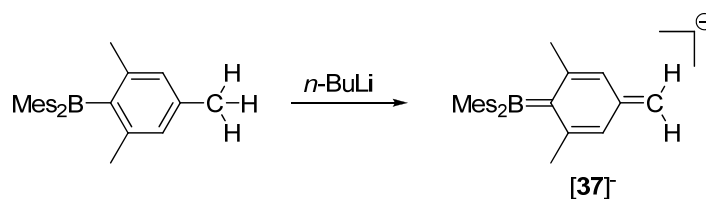


Figure 52. Synthesis of $[37]^-$

As an extension of their work with $[37]^-$, the Power group synthesized $[38]^-$ by deprotonation of Mes_2BMe with LiMes (Figure 53).⁷⁵ Derivative $[38]^-$ displays shorter B-C bond length of 1.438(9) Å, much shorter than that of $[37]^-$. The isolation of these

borata-alkene derivatives $[37]^-$ and $[38]^-$ provided new insights into the nature of B-C double bonds which had previously been proposed but never structurally characterized.

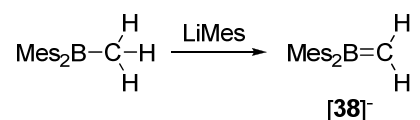


Figure 53. Synthesis of $[38]^-$

In 2007, the Gabbaï group reported the isolation of the first structurally characterized series illustrating the structural changes accompanying stepwise population of the B-C π -bond.^{40,76} The series $[2]^+/2^\bullet/[2]^-$ shows distinct changes in the B-C bond length (1.627(5) Å for $[2]^+$, 1.559(5) Å for 2^\bullet and 1.462(8) Å for $[2]^-$, Figure 54). Accompanying the bond length change, there is a noticeable change in the torsion angle about the B-C bond much like that reported for the all carbon derivative **36** (62.4° for $[2]^+$, 44.8° for 2^\bullet and 15.3° for $[2]^-$). It is important to note that both the carbon and the boron atoms in the B-C bond remain planar throughout the process which is indicative of stepwise population of a π -bond.

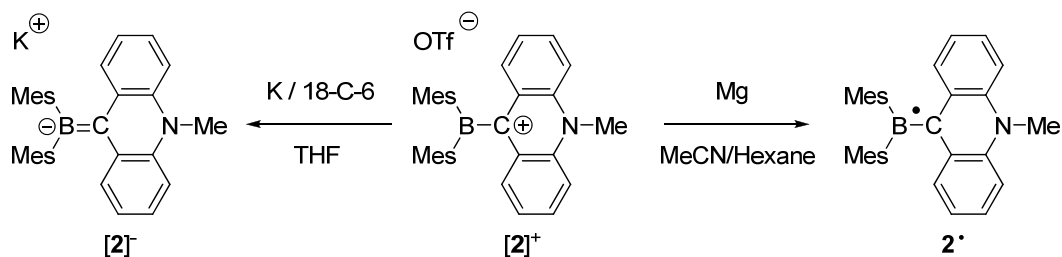


Figure 54. One and two electron reduction processes of $[2]^+$.

Building on the previous results published by Power, Gabbai and Kaim, we have explored the redox properties of derivatives in which a carbocation and a boryl unit are connected by a *p*-phenylene group.

3.2 Synthesis and structure

Lithiation of (4-bromophenyl)dimesitylborane followed by addition of xanthone or N-methylacridone affords the corresponding alcohols **39**-OH and **40**-OH after aqueous work up (Figure 55). Subsequent reaction with aqueous HBF₄ yields cations [**39**]⁺ and [**40**]⁺ as orange and yellow air stable salts, respectively. The ¹H NMR spectra of these salts reveals a significant downfield shift of the xanthone and acridine resonances with respect to the corresponding alcohols. The ¹¹B NMR spectra are diagnostic for free triaryl boranes with broad resonances at 76 and 78 ppm for [**39**]⁺ and [**40**]⁺, respectively.

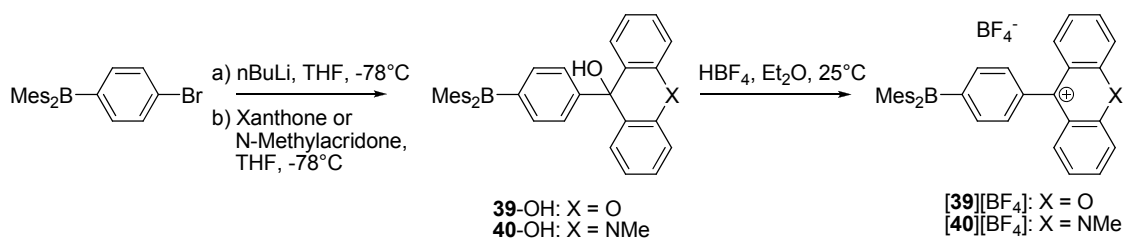


Figure 55. Synthesis of [**39**][BF₄] and [**40**][BF₄]

Salt [**39**][BF₄] crystallizes in the P2(1)/c space group with 4 molecules in the unit cell (Figure 56, Table 9). Examination of the structure of the cation [**39**]⁺, which is well separated from the [BF₄]⁻ anion reveals that the boron atom B(1) as well as the

methylum carbon C(7) are both indeed trigonal planar ($\Sigma_{\angle C-B-C} = 360.0^\circ$, $\Sigma_{\angle C-C-C} = 359.9^\circ$). As expected, the dimesitylboryl unit has oriented itself in such a way to optimize π conjugation with the *p*-phenylene backbone as evidenced by the relatively small dihedral angle of 23.6° formed between the planes defined by C(20)-B(1)-C(29) and C(3)-C(4)-C(5). On the other hand, the xanthenium unit forms a large dihedral angle of 66.0° between the C(8)-C(7)-C(19) and C(2)-C(1)-C(6) planes. This indicates very little conjugation with the π system of the *p*-phenylene linker.

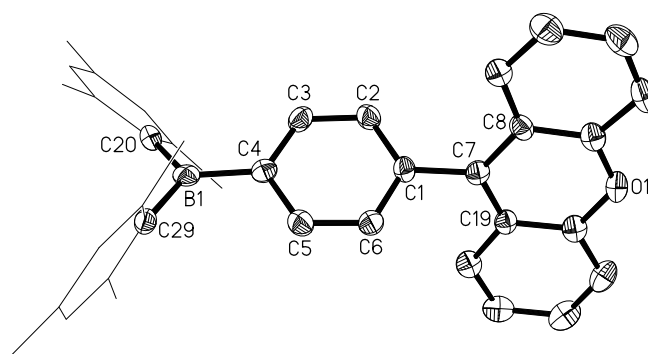


Figure 56. Crystal structure of $[39]^+$ in $[39][BF_4]$ (50% ellipsoid, H-atoms omitted and mesityl groups represented by thin lines for clarity). Selected distances [\AA] and angles [deg]: C(1)-C(6) 1.384(4), C(1)-C(2) 1.396(4), C(1)-C(7) 1.476(4), B(1)-C(4) 1.566(4), B(1)-C(20) 1.574(4), B(1)-C(29) 1.578(4), O(1)-C(13) 1.346(3), O(1)-C(14) 1.358(3), C(6)-C(1)-C(2) 119.8(2), C(6)-C(1)-C(7) 117.7(2), C(2)-C(1)-C(7) 122.5(2), C(4)-B(1)-C(20) 120.6(3), C(4)-B(1)-C(29) 118.0(2), C(20)-B(1)-C(29) 121.4(2), C(13)-O(1)-C(14) 121.0(2), C(19)-C(7)-C(8) 118.7(2), C(19)-C(7)-C(1) 119.8(2), C(8)-C(7)-C(1) 121.4(2).

Table 9. Crystal Data, Data Collection, and Structure Refinement for [39][BF₄].

Crystal data	[39][BF ₄]
Formula	C ₃₇ H ₃₄ B ₂ F ₄ O
M_r	592.26
crystal size (mm ³)	0.21 x 0.11 x 0.09
crystal system	Monoclinic
space group	P2(1)/c
a (Å)	14.766(2)
b (Å)	18.426(3)
c (Å)	11.3920(17)
α (°)	90
β (°)	104.089(2)
γ (°)	90
V (Å ³)	3006.1(8)
Z	4
ρ_{calc} (g cm ⁻³)	1.309
μ (mm ⁻¹)	0.093
$F(000)$	1240
Data Collection	
T (K)	110(2)
scan mode	ω
hkl range	-15 \rightarrow +15, -19 \rightarrow +19, -12 \rightarrow +12
measd reflns	22863
unique reflns [R_{int}]	3933 [0.0693]
reflns used for refinement	3933
Refinement	
refined parameters	397
GooF	1.006
R1, ^a wR2 ^b all data	0.0680, 0.1273
ρ_{fin} (max/min) (e Å ⁻³)	0.422, -0.290

The salt $[40][BF_4]$ also crystallizes in the $P2(1)/c$ space group with 4 molecules in the unit cell and is well separated from the $[BF_4]^-$ anion (Figure 57, Table 10). Inspection of the structure reveals many similarities to that of $[39]^+$. The boron atom B(1) and methylium carbon C(7) are both trigonal planar ($\Sigma_{\angle C-B-C} = 360.1^\circ$, $\Sigma_{\angle C-C-C} = 360.0^\circ$) as expected. Also, the dihedral angles for the dimesitylboryl (23.7°) and acridinium (65.3°) units are close to those observed in $[39]^+$.

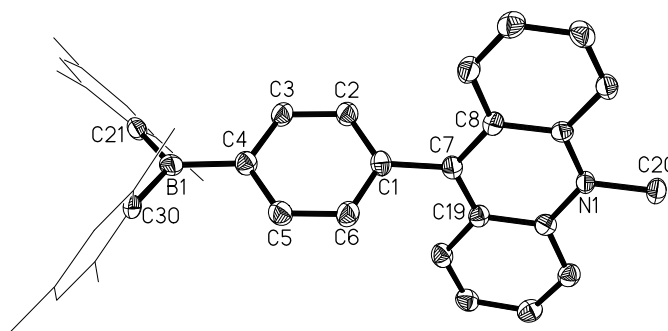


Figure 57. Crystal structure of $[40]^+$ in $[40][BF_4]$ (50% ellipsoid, H-atoms omitted and mesityl groups represented by thin lines for clarity). Selected distances [\AA] and angles [deg]: N(1)-C(13) 1.366(4), N(1)-C(14) 1.379(4), N(1)-C(20) 1.470(4), C(1)-C(6) 1.388(5), C(1)-C(2) 1.390(5), C(1)-C(7) 1.490(5), B(1)-C(4) 1.561(5), B(1)-C(21) 1.567(5), B(1)-C(30) 1.570(5), C(13)-N(1)-C(14) 122.1(3), C(13)-N(1)-C(20) 118.2(3), C(14)-N(1)-C(20) 119.7(3), C(6)-C(1)-C(2) 119.2(3), C(6)-C(1)-C(7) 117.8(3), C(2)-C(1)-C(7) 123.0(3), C(4)-B(1)-C(21) 120.7(3), C(4)-B(1)-C(30) 117.1(3), C(21)-B(1)-C(30) 122.3(3).

Table 10. Crystal Data, Data Collection, and Structure Refinement for [40][BF₄].

Crystal data	[40][BF ₄]
Formula	C ₃₈ H ₃₇ B ₂ F ₄ N
M_r	605.31
crystal size (mm ³)	0.23 x 0.09 x 0.08
crystal system	Monoclinic
space group	P2(1)/c
a (Å)	14.619(6)
b (Å)	18.738(8)
c (Å)	11.622(5)
α (°)	90
β (°)	103.495(6)
γ (°)	90
V (Å ³)	3096(2)
Z	4
ρ_{calc} (g cm ⁻³)	1.299
μ (mm ⁻¹)	0.090
$F(000)$	1272
Data Collection	
T (K)	110(2)
scan mode	ω
hkl range	-16 \rightarrow +16, -20 \rightarrow +21, -13 \rightarrow +13
measd reflns	21958
unique reflns [R_{int}]	4863 [0.0839]
reflns used for refinement	4863
Refinement	
refined parameters	406
GooF	1.008
$R1,^a$ $wR2^b$ all data	0.0924, 0.1659
ρ_{fin} (max/min) (e Å ⁻³)	0.416, -0.477

3.3 Electrochemistry

The cyclic voltammograms of $[39]^+$ and $[40]^+$ show two distinct waves. The first wave corresponding to the methylium center and formation of 39^\bullet and 40^\bullet is reversible, while the second wave to produce species $[39]^-$ and $[40]^-$ is boron based and appears to be quasi-reversible (Figure 58, Figure 59). A minimal shift in the reduction potentials of the methylium centers ($E_{1/2} = -0.386$ V for $[39]^+$ in CH_2Cl_2 and -0.99 V for $[40]^+$ in THF) is observed when compared to the non-borylated analogs ($E_{1/2} = -0.47$ V for phenylxanthenium and -0.86 V for phenylacridinium). This slight difference can be attributed to simple solvent effects rather than communication with the boron center. On the other hand, the dimesitylboryl reduction potentials ($E_{\text{peak}} = -1.60$ V and -1.94 V vs. Fc/Fc^+ for $[39]^+$ and $[40]^+$ respectively) are considerably more positive than that of Mes_3B ($E_{1/2} = -2.6$ V vs. Fc/Fc^+) owing to the stability of the resulting species $[39]^-$ and $[40]^-$. Encouraged by these results, we attempted the isolation of the singly reduced species 39^\bullet .

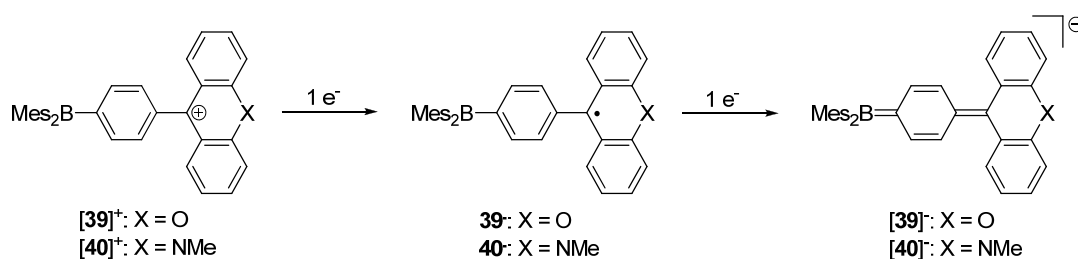


Figure 58. One and two electron reduction products of $[39]^+$ and $[40]^+$

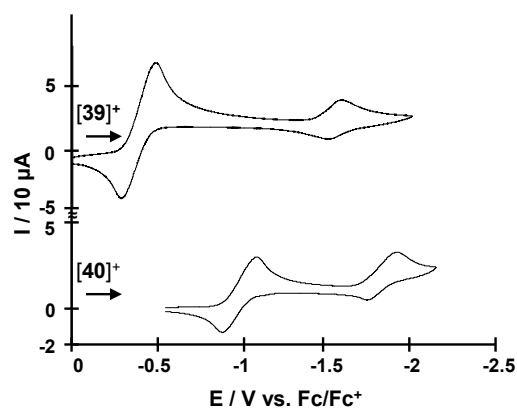


Figure 59. CV of $[39]^+$ in CH_2Cl_2 , and $[40]^+$ in THF with a glassy carbon working electrode; scan rate 100 mV s^{-1} , $0.1 \text{ M NBu}_4\text{PF}_6$.

Treatment of $[39]^+$ with magnesium in acetonitrile affords the reduction product 39^\bullet (Figure 60). The EPR spectrum of 39^\bullet in hexane can be simulated using the hyperfine coupling constants shown in Figure 61. The dimesitylboryl moiety has little ($a(^{11}\text{B}) = 0.78 \text{ G}$) contribution to the EPR signal. However, based on simple DFT calculations at the B3LYP 6-31G level of theory, the spin density map for 39^\bullet does indeed show some delocalization of the unpaired electron onto the boron atom (Figure 62).

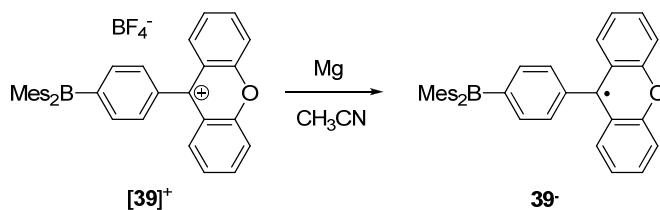


Figure 60. Reduction of $[39]^+$

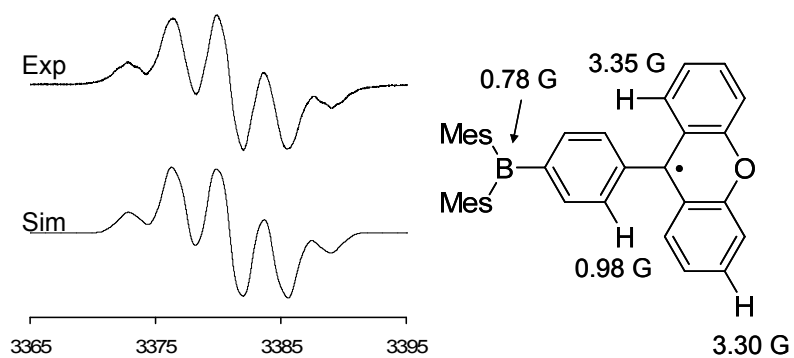


Figure 61. Experimental and simulated EPR spectra of **39'** (left) and hyperfine coupling parameters (right)

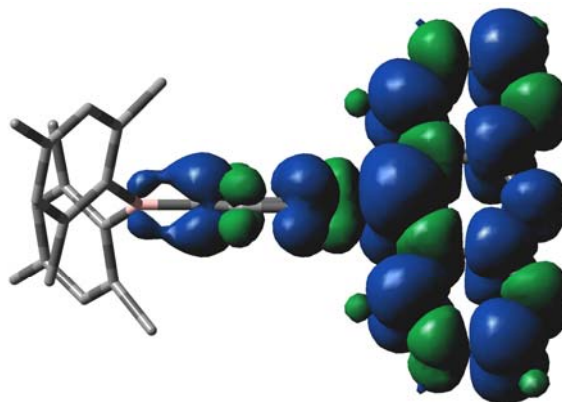


Figure 62. Calculated spin density map of **39'** (isovalue 0.0006).

Isolation of **39**[•] in the solid state has proven to be difficult, but upon exposure to oxygen, the peroxy species **41** is generated (Figure 63). Examination of the structure of **41** shows the former methylium centers C(7) and C(44) are now indeed tetrahedral and bonded to O(2) and O(4) respectively while the boron atoms B(1) and B(2) remain planar ($\Sigma\angle_{C-B-C} = 359.9^\circ$ and 360.0° respectively) (Figure 64, Table 11). The location of the peroxy bridge is not surprising since the former methylium centers display the largest amount of spin density.

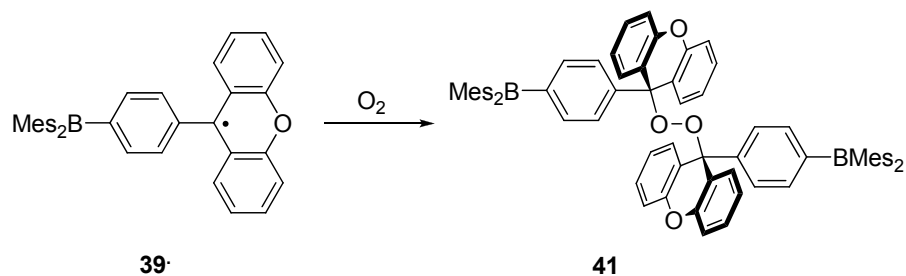


Figure 63. Synthesis of **41**

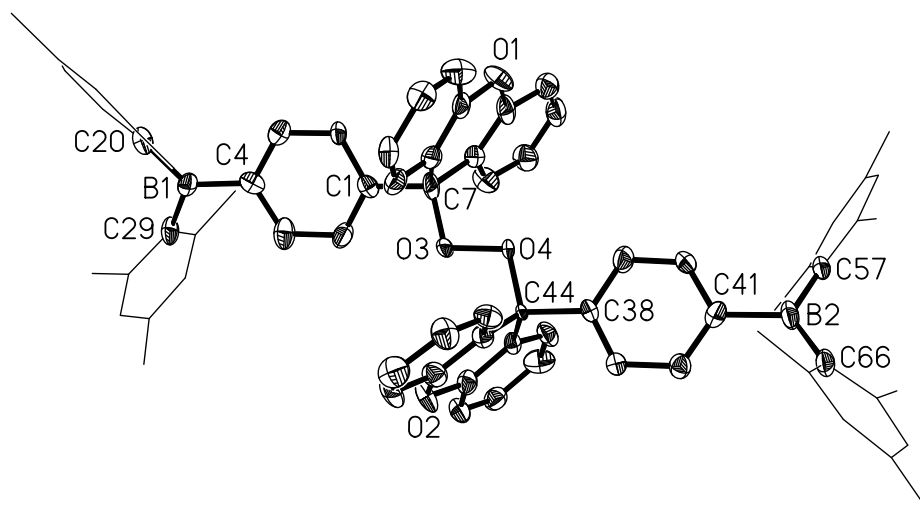


Figure 64. Crystal structure of **41** (50% ellipsoid, H-atoms omitted and mesityl groups represented by thin lines for clarity). Selected distances [\AA] and angles [deg]: O(1)-C(14) 1.393(10), O(1)-C(13) 1.398(10), C(1)-C(6) 1.348(11), C(1)-C(2) 1.397(12), C(1)-C(7) 1.553(11), B(1)-C(29) 1.551(14), B(1)-C(4) 1.552(13), B(1)-C(20) 1.563(13), O(2)-C(51) 1.378(10), O(2)-C(50) 1.382(9), B(2)-C(57) 1.567(14), B(2)-C(66) 1.569(14), B(2)-C(41) 1.604(13), O(3)-C(7) 1.436(10), O(3)-O(4) 1.490(7), O(4)-C(44) 1.461(9), C(14)-O(1)-C(13) 116.3(7), C(29)-B(1)-C(4) 116.9(8), C(29)-B(1)-C(20) 123.0(8), C(4)-B(1)-C(20) 120.0(9), C(51)-O(2)-C(50) 118.0(7), C(57)-B(2)-C(66) 125.6(8), C(57)-B(2)-C(41) 115.2(9), C(66)-B(2)-C(41) 119.2(8), C(7)-O(3)-O(4) 103.7(5), C(44)-O(4)-O(3) 105.0(5).

Table 11. Crystal Data, Data Collection, and Structure Refinement for **41-2(CH₂Cl₂)**.

Crystal data	41-2(CH₂Cl₂)
formula	C ₇₆ H ₇₂ B ₂ Cl ₄ O ₄
M_r	1212.76
crystal size (mm ³)	0.10 x 0.08 x 0.06
crystal system	Monoclinic
space group	Pc
a (Å)	20.127(6)
b (Å)	9.367(3)
c (Å)	17.039(5)
α (°)	90
β (°)	92.587(4)
γ (°)	90
V (Å ³)	3209.2(18)
Z	2
ρ_{calc} (g cm ⁻³)	1.255
μ (mm ⁻¹)	0.235
$F(000)$	1276
Data Collection	
T (K)	110(2)
scan mode	ω
hkl range	-23 \rightarrow +23, -10 \rightarrow +10, -19 \rightarrow +19
measd reflns	27216
unique reflns [R_{int}]	10047 [0.1281]
reflns used for refinement	10047
Refinement	
refined parameters	775
GooF	1.009
R1, ^a wR2 ^b all data	0.1838, 0.1987
ρ_{fin} (max/min) (e Å ⁻³)	0.542, -0.555

3.4 Other extended radical systems

In an exploratory part of this work, we synthesized symmetrical systems based on the 9,9-dimethylxanthene scaffold. 9,9-dimethylxanthene was treated with 2 eq. of *n*BuLi in ether overnight and xanthone was added the following day (Figure 65). Extraction of the crude mixture with ether following aqueous workup yielded crude **42**-(OH)₂ which was washed with hexane to yield pure **42**-(OH)₂. Dehydration of **42**-(OH)₂ with HBF₄ in ether yielded the dicationic species [**42**][BF₄]₂ as a dark red solid. ¹H NMR shows all the usual signals that one would expect from a 4,5-disubstituted 9,9-dimethylxanthene backbone, and all of the signals are well resolved with respect to the cationic moieties occupying the 4 and 5 positions of the backbone. Furthermore, the ¹H NMR of [**42**][BF₄]₂ showed a distinct downfield shift of all aromatic resonances with respect to the diol indicating the formation of the dication. Further evidence for the formation of the dication was observed in the ¹³C NMR in the form of a singlet at 173.4 ppm.

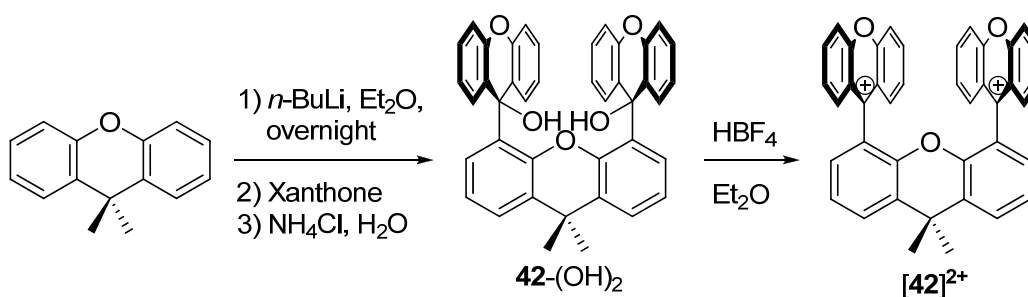


Figure 65. Synthesis of [**42**][BF₄]₂

Crystallization of the salt $[\mathbf{42}][\text{BF}_4]_2$ was possible by diffusing ether into a concentrated acetonitrile solution of $[\mathbf{42}][\text{BF}_4]_2$, but the X-ray diffraction data proved to be difficult to solve. Upon reaction of $[\mathbf{42}][\text{BF}_4]_2$ with I^- , the I_3^- salt $[\mathbf{42}][\text{I}_3]_2$ was obtained. This salt, crystallized by the same method, yielded a solvable data set (Figure 66, Table 12). Examination of the structure reveals that the carbocations C(16) and C(29) are planar (sum of angles) as expected. The planes of the cationic xanthene moieties are also orthogonal to the plane of the backbone. This indicates very little communication between the cationic substituents through the backbone. Further examination of the structure shows that the cationic xanthene units are bent slightly toward the center of the backbone. Perhaps this is due to Coulombic attraction to the more electronegative oxygen atom at the 1-position of the xanthene backbone, but more than likely it can be attributed to simple steric repulsions between the xanthenium moieties and the hydrogen atoms ortho to them.

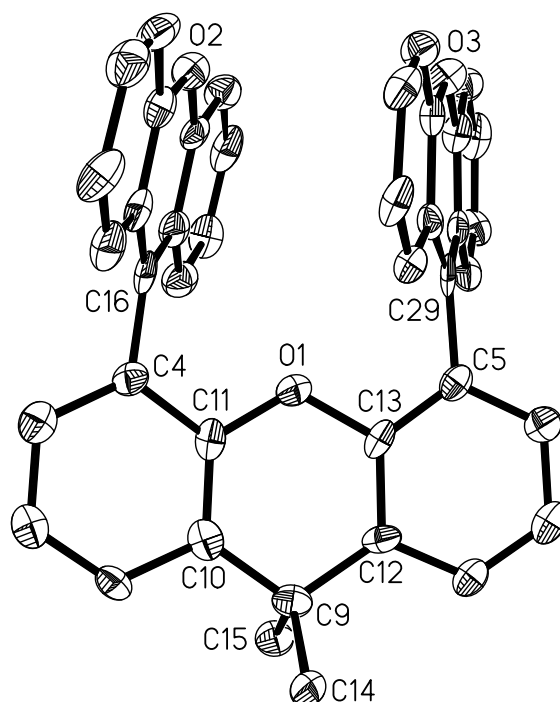


Figure 66. Crystal structure of $[42]^{2+}$ in $[42][I_3]_2$ (50% ellipsoid, H-atoms omitted for clarity) . Put in bond lengths etc. Selected distances [\AA] and angles [deg]: O(1)-C(11) 1.366(10), O(1)-C(13) 1.391(10), O(2)-C(23) 1.364(10), O(2)-C(22) 1.376(11), O(3)-C(35) 1.343(11), O(3)-C(36) 1.360(10), C(4)-C(16) 1.463(12), C(5)-C(29) 1.514(11), C(16)-C(17) 1.407(12), C(16)-C(28) 1.434(12), C(29)-C(30) 1.399(12), C(29)-C(41) 1.417(12), C(11)-O(1)-C(13) 120.5(7), C(23)-O(2)-C(22) 118.9(7), C(35)-O(3)-C(36) 121.4(7), C(17)-C(16)-C(28) 117.2(8), C(17)-C(16)-C(4) 121.6(8), C(28)-C(16)-C(4) 121.0(8), C(30)-C(29)-C(41) 120.2(8), C(30)-C(29)-C(5) 121.2(7), C(41)-C(29)-C(5) 118.6(8).

Table 12. Crystal Data, Data Collection, and Structure Refinement for [42][I₃]₂.

Crystal data	[42][I ₃] ₂
formula	C41 H28 I6 O3
M_r	1330.03
crystal size (mm ³)	0.20 x 0.20 x 0.06
crystal system	Monoclinic
space group	P2(1)/c
a (Å)	20.757(3)
b (Å)	14.407(2)
c (Å)	14.170(2)
α (°)	90
β (°)	108.642(2)
γ (°)	90
V (Å ³)	4015.4(10)
Z	4
ρ_{calc} (g cm ⁻³)	2.200
μ (mm ⁻¹)	4.679
$F(000)$	2464
Data Collection	
T (K)	110(2)
scan mode	ω
hkl range	-23 \rightarrow +23, -16 \rightarrow +15, -16 \rightarrow +16
measd reflns	25998
unique reflns [R_{int}]	6295 [0.0995]
reflns used for refinement	6295
Refinement	
refined parameters	454
GooF	1.006
$R1$, ^a $wR2$ ^b all data	0.0787, 0.1765
ρ_{fin} (max/min) (e Å ⁻³)	7.899, -1.725

The CV of $[42][BF_4]_2$ reveals two distinct reversible reduction waves (Figure 67). The first reduction at -0.28 V is considerably more positive than that observed for a normal single electron xanthenium reduction indicating that the second cationic center is destabilizing the molecule slightly, whereas the second reduction appears at -0.49 V where expected for a single electron xanthenium reduction. In an NMR reaction, addition of magnesium to an acetonitrile solution of $[42][BF_4]_2$ led to a loss of most of the NMR resonances as well as an extreme broadening of those that remained. This change in the NMR spectra suggests the species formed, is paramagnetic and therefore in the triplet state. Despite attempts to isolate and crystallize the putative diradical, no sufficient crystals have been obtained for X-ray analysis.

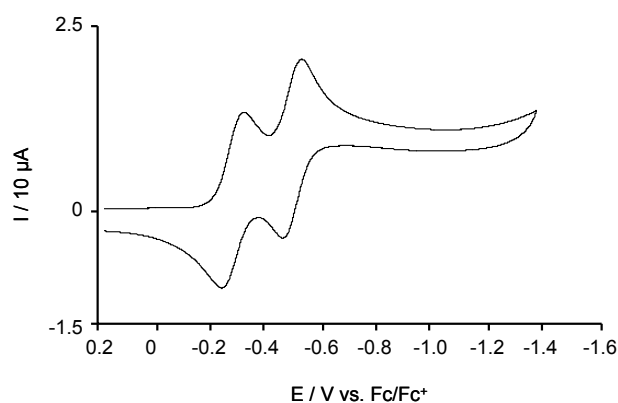


Figure 67. Cyclic voltammogram of $[42][BF_4]_2$ in MeCN with a Pt working electrode; scan rate 50 mV/sec, 0.1 M nBu_4NPF_6 (vs. Fc/Fc^+).

3.5 Conclusion

In conclusion, we report the synthesis of two new phenylene linked carbocationic boranes [39]⁺ and [40]⁺. When compared to [2]⁺, these novel systems cannot be reduced reversibly to the borata-alkenes. This lack of reversibility may arise from the inability of the carbocationic moiety to adopt a coplanar arrangement with the phenylene linker.

3.6 Experimental

Synthesis of [39][BF₄]. nBuLi (2.85 M in hexane, 1.1 ml, 3.13 mmol) was added to a solution of (4-bromophenyl)dimesitylborane (1.27 g, 3.13 mmol) in THF (10 ml) at -78°C. The solution was stirred for 1 hour, and xanthone (0.62 g, 3.13 mmol) in THF (10 ml) was added. After stirring for 30 minutes at -78°C, the reaction was allowed to warm to room temperature where it was stirred for another 2 hours. The reaction was quenched with 5% NH₄Cl_{aq} (20 ml) extracted with ether (2 x 10 ml), dried with MgSO₄ and solvent removed to afford crude 9-(4-(dimesitylboryl)phenyl)-9-xanthenol which was washed with hexane (2 x 5 ml) to remove most impurities. Without further purification, this solid was redissolved in ether and allowed to react with HBF₄ (40 % in H₂O, 2 mL) to afford [39][BF₄] (1.15 g) in 62% overall yield based on (4-bromophenyl)dimesitylborane. ¹H NMR (CD₃CN, 500 MHz): δ 2.09 (s, 12 H, CH_{Me}), δ 2.32 (s, 6H, CH_{Me}), δ 6.94 (s, 4 H, CH_{Mes}), δ 7.68 (d, 2 H, CH_{Ph}, ³J_{H-H} = 8.50 Hz), δ 7.80 (d, 2 H, CH_{Ph}, ³J_{H-H} = 8.0 Hz), δ 7.99 (t, 2 H, CH_{Xan}, ³J_{H-H} = 7.50 Hz), δ 8.17 (d, 2 H, CH_{Xan}, ³J_{H-H} = 9.00 Hz), δ 8.40 (d, 2 H, CH_{Xan}, ³J_{H-H} = 9.00 Hz), δ 8.60 (t, 2 H, CH_{Xan}, ³J_{H-H} = 7.00 Hz), ¹³C NMR (CD₃CN, 100.49 MHz): δ 21.27, 23.783, 120.68, 124.85,

129.35, 130.53, 131.16, 132.67, 134.54, 136.32, 140.75, 141.88, 142.24, 145.60, 151.12, 159.56, 175.92. ^{11}B NMR (CD_3CN , 128.21 MHz): δ -0.52 (s, BF_4), 76.00 (br, s).

Synthesis of [40][BF_4]. N-methylacridone (0.65 g, 3.13 mmol) was substituted for xanthone in the above procedure, and it was repeated to afford [40][BF_4] (1.27 g) in 67% overall yield based on (4-bromophenyl)dimesitylborane. ^1H NMR (CDCl_3 , 400 MHz): δ 2.11 (s, 12 H, CH_{Me}), δ 2.32 (s, 6H, CH_{Me}), δ 5.02 (s, 3H, $\text{CH}_{\text{N-Me}}$), δ 6.87 (s, 4 H, CH_{Mes}), δ 7.44 (d, 2 H, CH_{Ph} , $^3J_{\text{H-H}} = 7.60$ Hz), δ 7.80 (m, 4 H), δ 7.93 (d, 2 H, CH_{Acr} , $^3J_{\text{H-H}} = 8.80$ Hz), δ 8.38 (t, 2 H, CH_{Acr} , $^3J_{\text{H-H}} = 8.00$ Hz), δ 8.74 (d, 2 H, CH_{Acr} , $^3J_{\text{H-H}} = 8.80$ Hz). ^{13}C NMR (CDCl_3 , 100.47 MHz): δ 21.26, 23.59, 39.41, 119.09, 125.73, 128.01, 128.49, 129.46, 129.75, 135.83, 136.04, 139.20, 139.48, 140.79, 141.25, 141.62, 148.29, 161.06. ^{11}B NMR (CD_3CN , 128.21 MHz): δ -1.22 (s, BF_4), 78.00 (br, s).

Synthesis of [42][BF₄]₂. nBuLi (0.4 mL, 2.85 M) was added to a stirred solution of xanthene (0.200 g, 0.95 mmol) in ether (5 mL) at -78°C and allowed to warm to room temperature where it was stirred for overnight. At this time, the resulting pink suspension was cooled again to -78°C and xanthone (0.400 g, 2.03 mmol) in THF (20 mL) was added. The red suspension was stirred for one hour before being allowed to warm to room temperature. The reaction was quenched with a saturated NH₄Cl solution, extracted with ether (3 x 10 mL), dried over anhydrous magnesium sulfate, and the solvent removed to yield **42**-(OH)₂ as a crude white solid. Yield: 75% (0.430 g). The white powder (0.100 g) containing **42**-(OH)₂ was treated with 40% aqueous HBF₄ (1 mL) and stirred for five minutes until a deep red color was observed. The ether was then evaporated, and the resulting red solid washed with ether (3 x 5 mL) and dried to yield [42][BF₄]₂ as a dark red, air and water stable solid. Yield: 80% (0.098 g). ¹H NMR (CDCl₃, 500 MHz): δ 1.96 (s, 6 H, CH_{Me}), δ 7.19 (d, 2 H, CH, ³J_{H-H} = 6.49 Hz), δ 7.48 (m, 6 H), δ 7.72 (d, 4 H, ³J_{H-H} = 8.49 Hz), δ 8.05 (d, 2 H, ³J_{H-H} = 6.99 Hz), δ 8.22 (m, 8 H). ¹³C NMR (CDCl₃, 125.7 MHz): δ 33.94, 118.66, 119.38, 120.74, 124.37, 125.99, 130.58, 131.02, 132.20, 132.88, 133.32, 146.41, 158.44, 173.48.

CHAPTER IV

SYNTHESIS AND REDOX PROPERTIES OF α -PHOSPHONIO- AND α - PHOSPHONYL-CARBOCATIONS

4.1 Background

4.1.1 Phosphorus ylids

Phosphorus ylids have been used extensively in organic chemistry for the synthesis of olefins. Despite their widespread use, relatively little is known about their redox chemistry. One of the first studies concerning the electrochemical properties of pentaaryl phosphorus ylids was reported in 1970 by Schipper et al.³⁷ This report confirmed the oxidation of **43** to the radical cation $[\mathbf{43}]^{+\bullet}$ (Figure 68). EPR spectroscopy of the resulting radical cation showed a large hyperfine coupling constant to the phosphorus center of 26.6 G indicating a significant interaction of the radical with the phosphorus center. The EPR spectrum of $[\mathbf{43}]^{+\bullet}$ did not, however, show any coupling to the phenyl groups bound to phosphorus. Schipper and co-workers also reported the formation of the corresponding dication $[\mathbf{43}]^{2+}$, but were unable to isolate the red species. Cyclic voltammetry of **43** performed by Janssen and co-workers found the second oxidation to the dication $[\mathbf{43}]^{2+}$ to be irreversible indicating that the species is unstable.³⁵

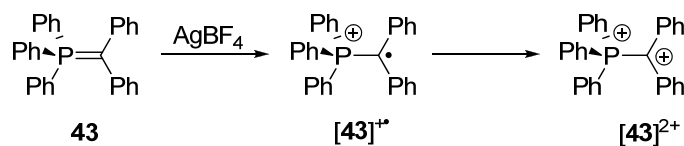


Figure 68. Oxidation of **43** to $[43]^+$ and proposed dication $[43]^{2+}$

Further studies carried out by Janssen and co-workers showed that when the radical cation $[43]^+$ is generated in situ, it slowly dimerizes in a tail to tail fashion (Figure 69). This resultant radical cation $[43-43]^+$ can be observed by EPR spectroscopy as a triplet with hyperfine coupling to the phosphorus center of 32.82 G.³⁵

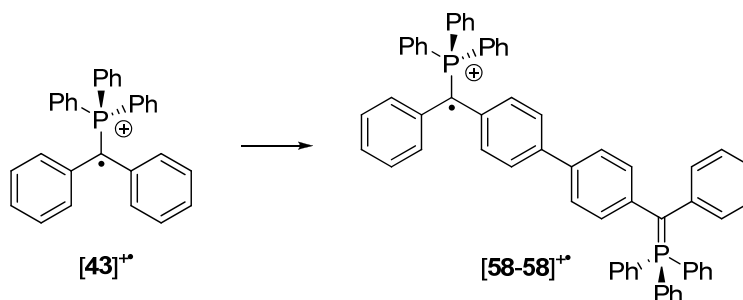


Figure 69. Dimerization of $[43]^+$

Kaim and co-workers have also been interested in phosphorus derivatives such as 44^{2+} (Figure 70).⁷⁷ Derivative $[44]^{2+}$ can be reduced by one electron to afford the radical cation $[44]^+$. EPR spectroscopy shows triplet with a 15.08 G coupling to each of the phosphorus centers at room temperature. It is important to note that CV of $[44]^{2+}$ revealed the reduction wave corresponding to the formation of the bisylid to be irreversible.

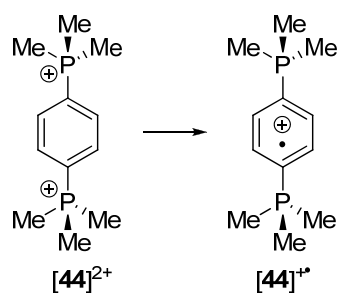


Figure 70. Reduction of $[\mathbf{44}]^{2+}$

4.1.2 Imminium and Imidazolium phosphonium species

Recently, Bertrand and co-workers have synthesized a variety of dicationic compounds which can be converted into ylids upon reduction.⁷⁸ Compound $[\mathbf{45}]^{2+}$ is formally an imminium phosphonium derivative, but when reduced by two electrons, the ylid **45** is isolated giving hope that both redox states are accessible (Figure 71). Another interesting derivative synthesized in the Bertrand group is $[\mathbf{46}]^{2+}$ (Figure 72). This derivative was synthesized by halide abstraction from the chloroimidazolium salt and triphenylphosphine. Reduction of this compound with two equivalents of potassium, however, results in dimerization of the carbene and liberation of triphenylphosphinyl moiety. This is potentially due to the steric requirement of triphenylphosphine.

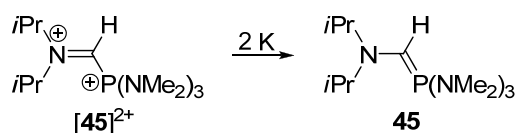


Figure 71. Reduction of $[\mathbf{45}]^{2+}$

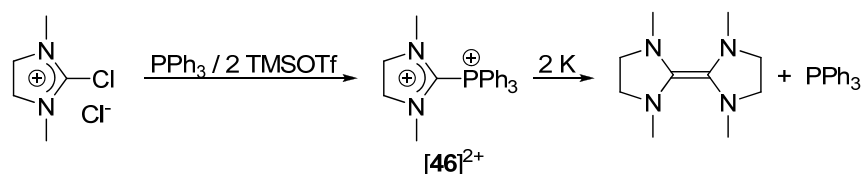


Figure 72. Synthesis and reduction of $[46]^{2+}$

4.1.3 α -phosphoryl radicals

In 2007, Apeloig et al. reported the formation of a coordination product between an Arduengo carbene and a diethyl phosphite moiety.³⁹ Irradiation of a mixture of the carbene and $[(i\text{PrO})_2(\text{O})\text{P}]_2\text{Hg}$ in benzene with UV light led to generation of derivative 47^\bullet as the coordination product (Figure 73). The EPR spectrum reveals a doublet with hyperfine coupling to the phosphorus center of 48.7 G. This large coupling constant is attributed to the ability of the phosphine oxide to accept electron density. Unfortunately, the coordination product is only observable under UV irradiation, and when the UV irradiation is turned off, the carbene dissociates and the radical is no longer observed.

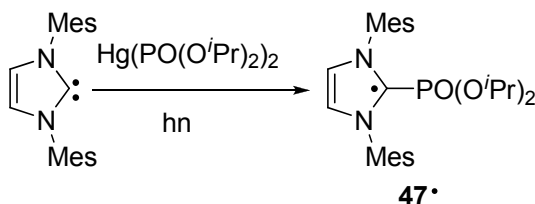


Figure 73. Synthesis and reduction of 47^\bullet

4.1.4 Reduction of 9,9-bipyridinium derivatives

Reduction of bipyridinium systems has been of interest to several groups due to the reversible nature of the oxidation/reduction processes. In 1981, Parker and co-workers reported the successful electrochemical characterization of 10,10'-dimethyl-9,9'-biacridylidene **48** series (Figure 74).⁷⁹ CV of the dication $[48]^{2+}$ in dichloromethane reveals two distinct reversible reduction/oxidation processes indicating the high stability of all three redox states.

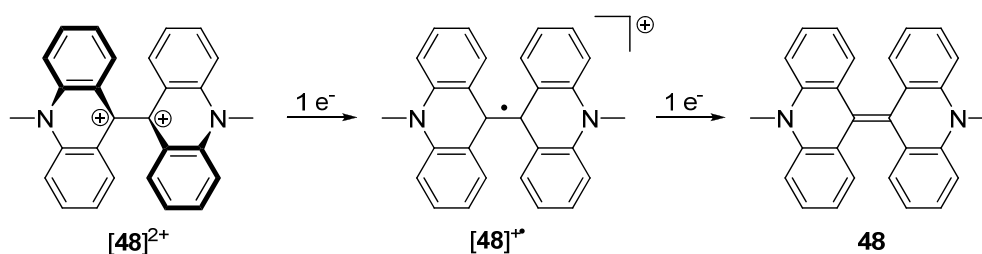


Figure 74. Electrochemical series of **48**

In 2005, the group of Vaid was able to successfully isolate and structurally characterize derivatives $[49]^{2+}$ and $[49]^{\bullet+}$ from the 1,1'-diphenyl-4,4'-bipyridylidene redox system (Figure 75).⁴² The solid state structures of $[49]^{2+}$ and $[49]^{\bullet+}$ differ in the planarity of the central ring systems. For $[49]^{2+}$, the twist is 37° whereas in $[49]^{\bullet+}$ the central rings are nearly coplanar with a twist of only 1° indicating that the delocalization of the radical helps to planarize the rings through increased π bonding. Indeed, the bond between the central rings is shortened by 0.057 \AA also indicating an increase in bond

order. Furthermore, although the doubly reduced species **49** was not characterized, the second reduction wave in the CV reported by the Vaid group is reversible providing evidence that **49** is isolable.

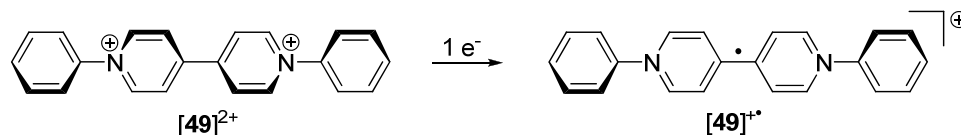


Figure 75. Reduction of [49]^{2+}

As part of our current interest in the chemistry of cationic electron deficient main group molecules, we have decided to target α -phosphonio-carbocations that have been previously difficult to isolate. In the initial phase of our work, we tried to reproduce the results reported by Schipper on the oxidation of **43** with AgBF_4 . Despite repeated attempts, we did not observe the formation of the corresponding dication. Faced with this failure, we decided to focus on a system possessing a donor stabilized carbocationic center. Building on the redox chemistry of bipyridinium systems, we targeted the direct synthesis of dications of type \mathbf{A}^{2+} (Figure 76).

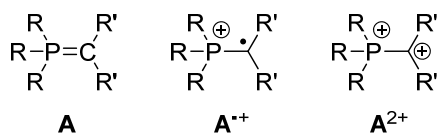


Figure 76. Different oxidation states of P-C double bonds.

4.2 Synthesis and structure

Employing the halide abstraction chemistry used by Bertrand, 9-bromo-*N*-methylacridinium was treated with Ph_3P , (*p*-ClPh) $_3\text{P}$ and Ph_2MeP in PhCl in the presence of TMSOTf. Under these conditions, an immediate reaction took place leading to the precipitation of the dications $[\mathbf{50}]^{2+}$, $[\mathbf{51}]^{2+}$ (as bright yellow solids) and $[\mathbf{52}]^{2+}$ (as an orange solid) which were isolated by filtration (Figure 77). These salts are remarkably stable and soluble in MeCN. They can easily be handled in air without apparent decomposition. They have been fully characterized. Some of the most salient spectroscopic features include: i) a ^{31}P NMR resonance at 20.78 ($[\mathbf{50}]^{2+}$), 20.86 ($[\mathbf{51}]^{2+}$) and 20.85 ($[\mathbf{52}]^{2+}$) ppm corresponding to the phosphonium center; ii) a ^1H NMR resonance at 5.07 ($[\mathbf{50}]^{2+}$), 5.06 ($[\mathbf{51}]^{2+}$) and 5.02 ($[\mathbf{52}]^{2+}$) ppm corresponding to the *N*-methyl group; and iii) a ^{13}C NMR resonance of the C-9 carbon atom of the acridinium unit at 142.85 ($[\mathbf{50}]^{2+}$) and 142.82 ($[\mathbf{51}]^{2+}$). We note that the α -phosphonio-acridinium dications (form **a**) can be alternatively described as α -phosphonio-carbocations (form **b**).

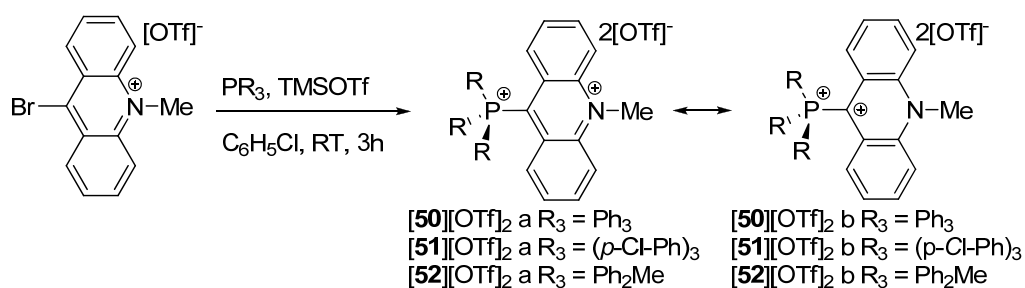


Figure 77. Synthesis of **[50][OTf]₂**, **[51][OTf]₂** and **[52][OTf]₂**

The dication **[50]²⁺** can also be observed by ESI MS at $m/z = 227.58$ amu. Final confirmation for the formation of these α -phosphonio-carbocations was derived from single crystal X-ray diffraction studies (Figure 78, Figure 79, Figure 80, Table 13, Table 14, Table 15). Inspection of the molecular structure indicates that the P(1)-C(9) distances (1.835(4) Å, 1.827(7) Å and 1.827(6) Å for **50²⁺**, **51²⁺** and **52²⁺** respectively) are slightly elongated. This slight elongation can be assigned to electrostatic repulsion between the phosphonium center and the C-9 methylium center. The acridinium moiety is strictly planar in all cases indicating stabilization of the carbocationic center by the aromatic π -system.

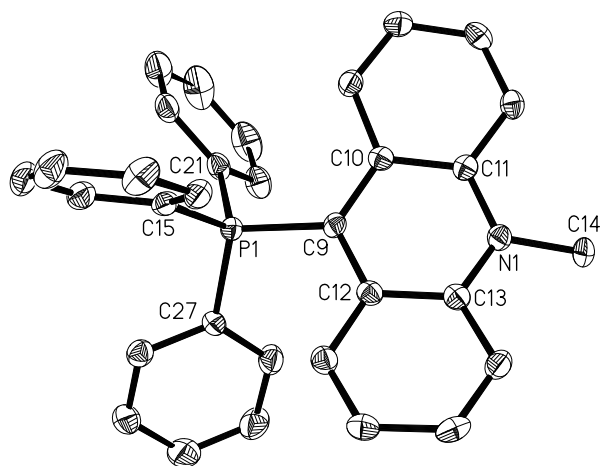


Figure 78. Crystal structure of $[50]^{2+}$ in $[50][OTf]_2$ (50% ellipsoid, H-atoms omitted for clarity); selected bond lengths (Å) and angles (deg). P(1)-C(15) 1.789(4), P(1)-C(27) 1.802(4), P(1)-C(21) 1.799(4), P(1)-C(9) 1.835(4), N(1)-C(11) 1.354(6), N(1)-C(13) 1.363(6), N(1)-C(14) 1.483(5), C(10)-C(9) 1.403(6), C(9)-C(12) 1.410(6), C(15)-P(1)-C(27) 112.8(2), C(15)-P(1)-C(21) 111.9(2), C(27)-P(1)-C(21) 104.8(2), C(15)-P(1)-C(9) 108.3(2), C(27)-P(1)-C(9) 108.2(2), C(21)-P(1)-C(9) 110.8(2), C(11)-N(1)-C(13) 121.5(4), C(11)-N(1)-C(14) 118.8(4), C(13)-N(1)-C(14) 119.7(4), C(10)-C(9)-C(12) 119.6(4), C(10)-C(9)-P(1) 120.9(3), C(12)-C(9)-P(1) 119.6(3).

Table 13. Crystal Data, Data Collection, and Structure Refinement for [50][OTf]₂-CH₃CN.

Crystal data	[50][OTf] ₂ -CH ₃ CN
Formula	C ₃₆ H ₂₉ F ₆ N ₂ O ₆ PS ₂
M_r	794.70
crystal size (mm ³)	0.21 x 0.11 x 0.08
crystal system	Triclinic
space group	<i>P</i> -1
<i>a</i> (Å)	8.8521(18)
<i>b</i> (Å)	11.469(2)
<i>c</i> (Å)	17.493(4)
α (°)	94.488(3)
β (°)	96.354(3)
γ (°)	91.056(3)
<i>V</i> (Å ³)	1759.0(6)
<i>Z</i>	2
ρ_{calc} (g cm ⁻³)	1.500
μ (mm ⁻¹)	0.278
<i>F</i> (000)	816
Data Collection	
<i>T</i> (K)	110(2)
scan mode	ω
<i>hkl</i> range	-10 → +10, -13 → +13, -19 → +20
measd reflns	11662
unique reflns [<i>R</i> _{int}]	5492 [0.0285]
reflns used for refinement	5492
Refinement	
refined parameters	479
GooF	1.006
R1, ^a wR2 ^b all data	0.0898, 0.1662
ρ_{fin} (max/min) (e Å ⁻³)	1.191, -1.335

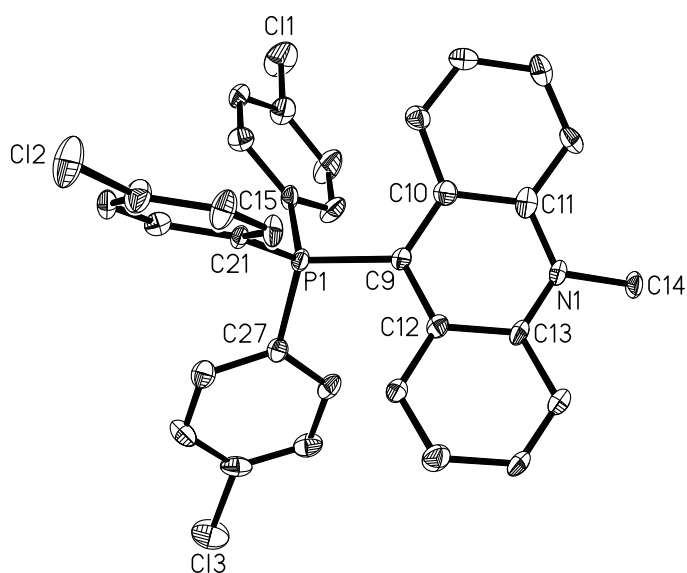


Figure 79. Crystal structure of $[51]^{2+}$ in $[51][OTf]_2$ (50% ellipsoid, H-atoms omitted for clarity); selected bond lengths (Å) and angles (deg). P(1)-C(21) 1.764(7), P(1)-C(15) 1.795(7), P(1)-C(27) 1.807(7), P(1)-C(9) 1.827(7), N(1)-C(11) 1.360(8), N(1)-C(13) 1.378(8), N(1)-C(14) 1.470(8), C(9)-C(12) 1.400(9), C(9)-C(10) 1.418(9), C(21)-P(1)-C(15) 113.0(3), C(21)-P(1)-C(27) 111.6(3), C(15)-P(1)-C(27) 104.8(3), C(21)-P(1)-C(9) 110.5(3), C(15)-P(1)-C(9) 107.3(3), C(27)-P(1)-C(9) 109.4(3), C(11)-N(1)-C(13) 121.5(5), C(11)-N(1)-C(14) 118.2(6), C(13)-N(1)-C(14) 120.3(5), C(12)-C(9)-C(10) 119.8(6), C(12)-C(9)-P(1) 119.8(5), C(10)-C(9)-P(1) 120.2(5).

Table 14. Crystal Data, Data Collection, and Structure Refinement for [51][OTf]₂-Et₂O.

Crystal data	[51][OTf] ₂ -Et ₂ O
Formula	C ₃₈ H ₃₃ Cl ₃ F ₆ NO ₇ PS ₂
M_r	931.09
crystal size (mm ³)	0.13 x 0.11 x 0.05
crystal system	Monoclinic
space group	P2(1)/c
a (Å)	10.355(14)
b (Å)	19.22(3)
c (Å)	20.96(3)
α (°)	90
β (°)	95.31(3)
γ (°)	90
V (Å ³)	4153(10)
Z	4
ρ_{calc} (g cm ⁻³)	1.489
μ (mm ⁻¹)	0.436
$F(000)$	1904
Data Collection	
T (K)	110(2)
scan mode	ω
hkl range	-11 \rightarrow +11, -22 \rightarrow +21, -23 \rightarrow +15
measd reflns	19614
unique reflns [R_{int}]	6487 [0.1049]
reflns used for refinement	6487
Refinement	
refined parameters	523
Goof	1.005
$R1$, ^a $wR2$ ^b all data	0.1347, 0.2137
ρ_{fin} (max/min) (e Å ⁻³)	0.589, -0.610

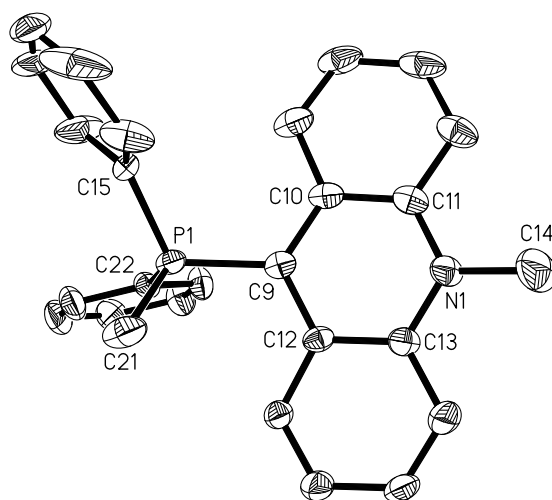


Figure 80. Crystal structure of $[52]^{2+}$ in $[52][OTf]_2$ (50% ellipsoid, H-atoms omitted for clarity); selected bond lengths (Å) and angles (deg). P(1)-C(22) 1.782(6), P(1)-C(15) 1.790(5), P(1)-C(21) 1.803(6), P(1)-C(9) 1.827(6), N(1)-C(11) 1.359(8), N(1)-C(13) 1.365(7), N(1)-C(14) 1.477(9), C(9)-C(12) 1.401(7), C(9)-C(10) 1.414(8), C(22)-P(1)-C(15) 110.8(3), C(22)-P(1)-C(21) 112.9(4), C(15)-P(1)-C(21) 101.1(3), C(22)-P(1)-C(9) 106.0(3), C(15)-P(1)-C(9) 115.0(3), C(21)-P(1)-C(9) 111.2(3), C(11)-N(1)-C(13) 122.2(5), C(11)-N(1)-C(14) 117.4(6), C(13)-N(1)-C(14) 120.4(6), C(12)-C(9)-C(10) 119.4(5), C(12)-C(9)-P(1) 118.5(4), C(10)-C(9)-P(1) 122.1(4).

Table 15. Crystal Data, Data Collection, and Structure Refinement for [52][OTf]₂.

Crystal data	[52][OTf] ₂
formula	C ₂₉ H ₂₄ F ₆ NO ₆ PS ₂
M_r	691.58
crystal size (mm ³)	0.13 x 0.12 x 0.08
crystal system	Triclinic
space group	<i>P</i> -1
a (Å)	8.1302(14)
b (Å)	10.4702(18)
c (Å)	18.089(3)
α (°)	100.441(2)
β (°)	101.919(2)
γ (°)	93.448(2)
V (Å ³)	1474.0(4)
Z	2
ρ_{calc} (g cm ⁻³)	1.558
μ (mm ⁻¹)	0.318
$F(000)$	708
Data Collection	
T (K)	110(2)
scan mode	ω
hkl range	-10 \rightarrow +10, -13 \rightarrow +14, -24 \rightarrow +23
measd reflns	17161
unique reflns [R_{int}]	6883 [0.0256]
reflns used for refinement	6883
Refinement	
refined parameters	407
GooF	1.007
R1, ^a wR2 ^b all data	0.1488, 0.3041
ρ_{fin} (max/min) (e Å ⁻³)	3.821, -1.970

To better understand the properties of these dications, the structure of $[50]^{2+}$ has been computed at the B3LYP/6-31+g(d) level of theory and compared to the computed structure of the monocation triphenyl-9-acridinyl-phosponium ($[I]^+$). These computational studies show that the P-C_{acr} bond length increases from 1.848 to 1.893 Å upon methylation thus supporting the presence of increased electrostatic repulsion in the dication $[50]^{2+}$.

The dication $[50]^{2+}$ reacts with Lewis basic substrates such as pyridine or DMAP in MeCN to afford the corresponding pyridine or DMAP stabilized dications $[53][OTf]_2$ and $[54][OTf]_2$ (Figure 81). These reactions can be described as ligand exchange reactions thus suggesting that $[50]^{2+}$ (as well as $[53]^{2+}$ and $[54]^{2+}$) can be regarded as ligand stabilized carbocations (representation **c**; Figure 82). The two new salts $[53][OTf]_2$ and $[54][OTf]_2$, which can easily be handled in air, have been fully characterized. Their 1H NMR spectra exhibit resonances for the acridinium moiety that are very similar to those observed for $[50]^{2+}$ as well as the expected resonances for the coordinated pyridine and DMAP, respectively.

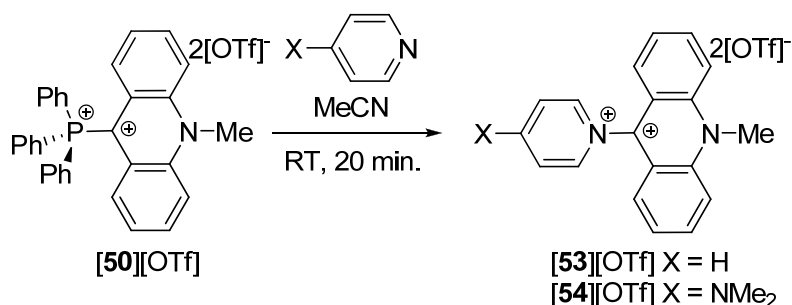


Figure 81. Synthesis of $[53][OTf]_2$ and $[54][OTf]_2$

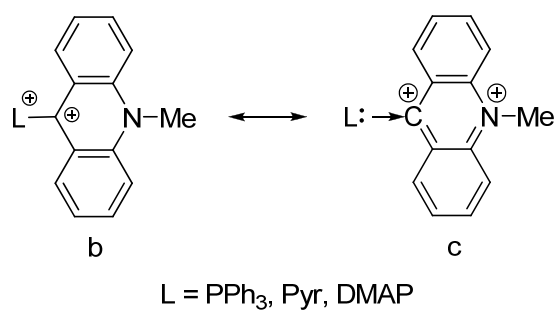


Figure 82. Representations of forms **b** and **c** of ligand stabilized carbocations

Both of these salts have been characterized by X-ray diffraction which confirms the proposed connectivity (Figure 83, Figure 84, Table 16, Table 17). In both structures, the acridinium moiety adopts a planar conformation and forms a dihedral angle of 83.2° and 76.8°(av.) with the plane containing the pyridine or DMAP ligand respectively. This large twist angle indicates the absence of any π -conjugation between the acridinium moiety and the pyridine or DMAP ligand.

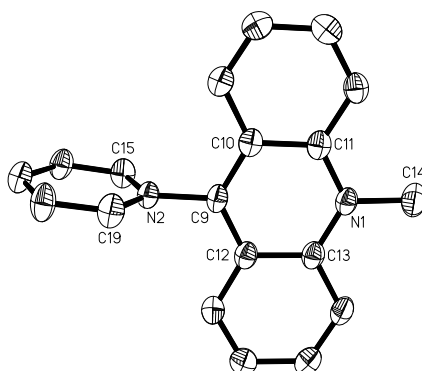


Figure 83. Crystal structure of $[53]^{2+}$ in $[53][OTf]_2$ (50% ellipsoid, H-atoms omitted for clarity); selected bond lengths (Å) and angles (deg). N(1)-C(13) 1.360(3), N(1)-C(11) 1.366(3), N(1)-C(14) 1.500(3), N(2)-C(15) 1.344(3), N(2)-C(19) 1.346(3), N(2)-C(9) 1.462(3), C(9)-C(10) 1.383(3), C(9)-C(12) 1.386(3), C(13)-N(1)-C(11) 122.45(19), C(13)-N(1)-C(14) 119.4(2), C(11)-N(1)-C(14) 117.9(2), C(15)-N(2)-C(19) 121.76(19), C(15)-N(2)-C(9) 118.51(18), C(19)-N(2)-C(9) 119.52(18), C(10)-C(9)-C(12) 123.56(19), C(10)-C(9)-N(2) 117.42(19), C(12)-C(9)-N(2) 119.0(2).

Table 16. Crystal Data, Data Collection, and Structure Refinement for [53][OTf]₂-CH₃CN.

Crystal data	[53][OTf] ₂ -CH ₃ CN
Formula	C ₂₃ H ₁₉ F ₆ N ₃ O ₆ S ₂
<i>M</i> _r	611.53
crystal size (mm ³)	0.46 x 0.19 x 0.05
crystal system	Triclinic
space group	<i>P</i> -1
<i>a</i> (Å)	7.768(5)
<i>b</i> (Å)	12.784(8)
<i>c</i> (Å)	13.518(8)
<i>α</i> (°)	80.568(11)
<i>β</i> (°)	84.351(11)
<i>γ</i> (°)	85.296(12)
<i>V</i> (Å ³)	1314.9(14)
<i>Z</i>	2
<i>ρ</i> _{calc} (g cm ⁻³)	1.545
<i>μ</i> (mm ⁻¹)	0.289
<i>F</i> (000)	624
Data Collection	
<i>T</i> (K)	110(2)
scan mode	<i>ω</i>
<i>hkl</i> range	-7 → +10, -17 → +17, -18 → +17
measd reflns	8434
unique reflns [<i>R</i> _{int}]	6136 [0.0604]
reflns used for refinement	6136
Refinement	
refined parameters	362
GooF	1.006
R1, ^a wR2 ^b all data	0.0715, 0.1532
<i>ρ</i> _{fin} (max/min) (e Å ⁻³)	0.870, -0.368

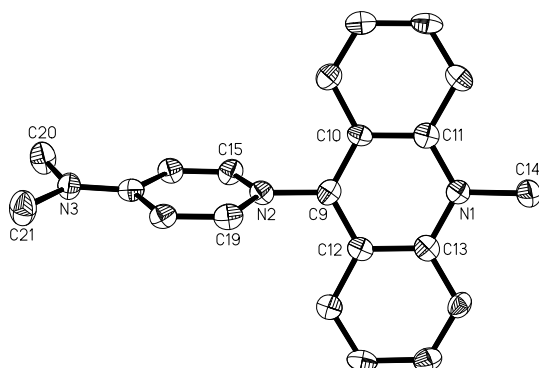


Figure 84. Crystal structure of $[54]^{2+}$ in $[54][OTf]_2$ (50% ellipsoid, H-atoms omitted for clarity); selected bond lengths (Å) and angles (deg). N(1)-C(13) 1.375(6), N(1)-C(11) 1.382(6), N(1)-C(14) 1.484(6), N(2)-C(15) 1.366(6), N(2)-C(19) 1.376(6), N(2)-C(9) 1.445(6), N(3)-C(17) 1.316(6), N(3)-C(20) 1.462(6), N(3)-C(21) 1.465(6), C(9)-C(10) 1.391(6), C(9)-C(12) 1.393(6), C(13)-N(1)-C(11) 121.8(4), C(13)-N(1)-C(14) 117.7(4), C(11)-N(1)-C(14) 120.4(4), C(15)-N(2)-C(19) 119.2(4), C(15)-N(2)-C(9) 121.2(4), C(19)-N(2)-C(9) 119.7(4), C(17)-N(3)-C(20) 121.0(4), C(17)-N(3)-C(21) 120.8(4), C(20)-N(3)-C(21) 118.0(4), C(10)-C(9)-C(12) 122.4(4), C(10)-C(9)-N(2) 118.8(4), C(12)-C(9)-N(2) 118.8(4).

Table 17. Crystal Data, Data Collection, and Structure Refinement for [54][OTf]₂-CH₃CN.

Crystal data	[54][OTf] ₂ -CH ₃ CN
Formula	C ₂₅ H ₂₄ F ₆ N ₄ O ₆ S ₂
M_r	654.60
crystal size (mm ³)	0.35 x 0.21 x 0.12
crystal system	Monoclinic
space group	P2(1)/n
a (Å)	10.211(4)
b (Å)	20.565(8)
c (Å)	26.905(10)
α (°)	90
β (°)	92.698(5)
γ (°)	90
V (Å ³)	5644(4)
Z	8
ρ_{calc} (g cm ⁻³)	1.541
μ (mm ⁻¹)	0.276
$F(000)$	2688
Data Collection	
T (K)	110(2)
scan mode	ω
hkl range	-11 \rightarrow +11, -23 \rightarrow +23, -30 \rightarrow +27
measd reflns	36049
unique reflns [R_{int}]	8864 [0.1097]
reflns used for refinement	8864
Refinement	
refined parameters	783
Goof	1.004
R1, ^a wR2 ^b all data	0.1145, 0.1737
ρ_{fin} (max/min) (e Å ⁻³)	0.363, -0.431

4.3 Electrochemistry

With these dications in hand, we decided to investigate their redox behavior. To this end, we recorded their cyclic voltammogram in MeCN using a glassy carbon electrode (Figure 85). In all three cases, the dications undergo a reversible reduction followed by an irreversible one, respectively. A comparison of the first reduction potential of these dications (-0.21 V for $[\mathbf{50}]^{2+}$ vs. -0.49 V for $[\mathbf{53}]^{2+}$ and -0.61 V for $[\mathbf{54}]^{2+}$) show that $[\mathbf{50}]^{2+}$ is substantially more electrophilic than $[\mathbf{53}]^{2+}$ and $[\mathbf{54}]^{2+}$. This measurement also suggests that resulting radical cation $[\mathbf{50}]^{2+}$ should be relatively stable. In order to verify this assumption, $[\mathbf{50}]^{2+}$ was reduced with 1eq. of Na/Hg in THF to produce a dark green solution of $[\mathbf{50}]^{+\bullet}$. EPR spectroscopy carried on this solution allowed for the detection of a signal which is split into a doublet by a ^{31}P hyperfine coupling constant of 18 G. This hyperfine coupling constant can be compared to the value of 26.3 G reported for $[\text{Ph}_3\text{PCPh}_2]^{+\bullet}$. The fine structure of the spectrum could be further simulated using the hyperfine coupling constants shown in Figure 86 which are typical of N-methyl-acridinyl radicals.

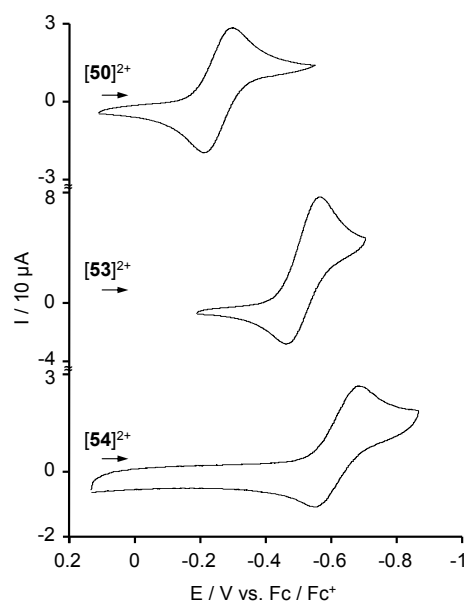


Figure 85. CV of $[50]^{2+}$, $[53]^{2+}$ and $[54]^{2+}$ in CH_3CN with a glassy carbon working electrode; scan rate 100 mV s^{-1} , $0.1 \text{ M NBu}_4\text{PF}_6$.

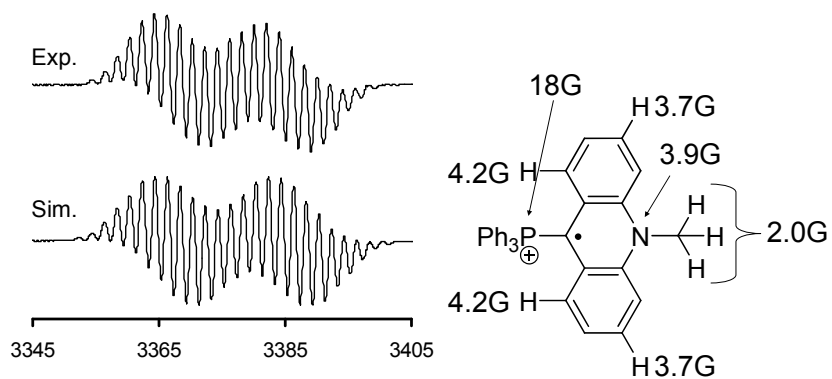


Figure 86. Experimental and simulated EPR spectra of $[50]^{+}$ (left) and hyperfine coupling parameters (right)

Unlike $[\text{Ph}_3\text{PCPh}_2]^{++}$ which is only moderately stable, solutions of $[\mathbf{50}]^{++}$ can be stored for several days at -20°C without notable decay of the EPR signal intensity. Last but not least, the irreversible second wave observed in the cyclic voltammogram of $[\mathbf{50}]^{2+}$ suggests that the neutral ylid may be too electron rich to observe under those conditions.

4.4 Synthesis and structure of α -phosphonyl-carbocations

Lithiation of 9-bromoacridine followed by quenching with diethylphosphonyl chloride affords the neutral phosphonate ester **55** (Figure 87). Methylation of the nitrogen leads to formation of the cationic species $[\mathbf{56}]^+$ which can be isolated as a yellow solid in good yield. Some of the notable spectroscopic features of $[\mathbf{56}]^+$ are i) a ^1H NMR resonance at 5.10 ppm corresponding to the N-methyl group, ii) a ^{13}C resonance at 146.5 ppm for the carbocation and iii) a ^{31}P NMR resonance at 10.56 ppm indicative of a phosphonate ester. Crystals of this salt were grown from acetonitrile/ether, and the structure determined (Figure 88, Table 18). As before, the acridinium moiety is strictly planar ($\Sigma\angle\text{X-C(9)-X} = 360.0^\circ$). Furthermore, the P(1)-O(1) bond aligns itself with the planar acridinium moiety presumably to effect greater conjugation throughout the system.

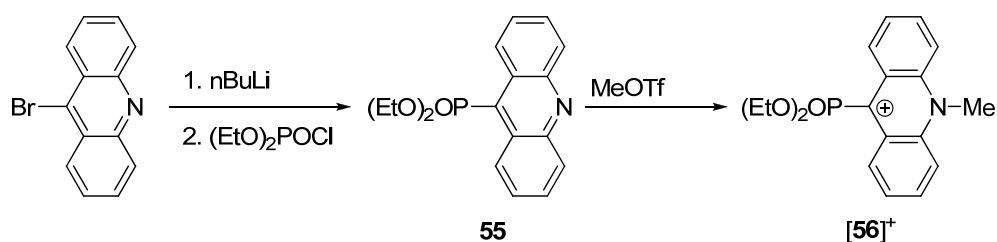


Figure 87. Synthesis of $[\mathbf{56}]^+$

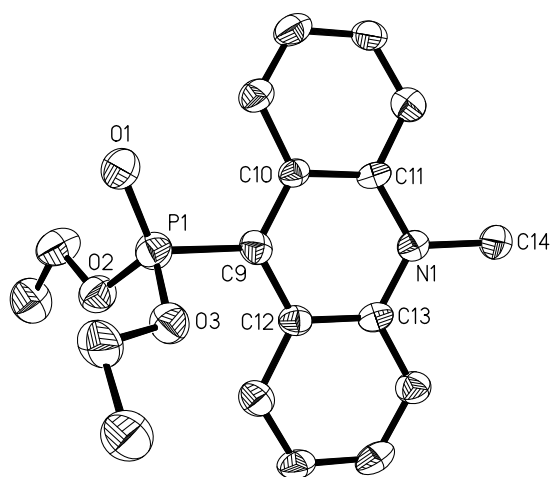


Figure 88. Crystal structure of $[56]^+$ in $[56][OTf]$ (50% ellipsoid, H-atoms omitted for clarity); selected bond lengths (Å) and angles (deg). P(1)-O(1) 1.458(5), P(1)-O(3) 1.562(5), P(1)-O(2) 1.569(5), P(1)-C(9) 1.826(7), O(2)-C(15) 1.452(9), N(1)-C(11) 1.365(8), N(1)-C(13) 1.368(8), N(1)-C(14) 1.479(8), O(3)-C(17) 1.469(8), O(1)-P(1)-O(3) 116.1(3), O(1)-P(1)-O(2) 114.1(3), O(3)-P(1)-O(2) 103.5(3), O(1)-P(1)-C(9) 115.7(3), O(3)-P(1)-C(9) 99.8(3), O(2)-P(1)-C(9) 105.9(3), C(15)-O(2)-P(1) 120.5(5), C(11)-N(1)-C(13) 121.4(6), C(11)-N(1)-C(14) 117.7(5), C(13)-N(1)-C(14) 120.9(5), C(17)-O(3)-P(1) 120.4(5), C(10)-C(9)-C(12) 119.2(6), C(10)-C(9)-P(1) 120.9(5), C(12)-C(9)-P(1) 119.9(5).

Table 18. Crystal Data, Data Collection, and Structure Refinement for [56][OTf].

Crystal data	[56][OTf]
Formula	C ₁₉ H ₂₁ F ₃ NO ₆ PS
M_r	479.40
crystal size (mm ³)	0.25 x 0.05 x 0.03
crystal system	Triclinic
space group	<i>P</i> -1
a (Å)	8.110(6)
b (Å)	11.825(8)
c (Å)	11.877(8)
α (°)	104.216(12)
β (°)	107.182(11)
γ (°)	92.472(13)
V (Å ³)	1046.5(12)
Z	2
ρ_{calc} (g cm ⁻³)	1.521
μ (mm ⁻¹)	0.295
$F(000)$	496
Data Collection	
T (K)	110(2)
scan mode	ω
hkl range	-9 \rightarrow +5, -13 \rightarrow +12, -13 \rightarrow +13
measd reflns	4840
unique reflns	3227 [0.0492]
reflns used for	3227
Refinement	
refined	280
GooF	1.008
R1, ^a wR2 ^b all	0.1146, 0.2050
ρ_{fin} (max/min) (e)	0.513, -0.362

4.5 Electrochemistry of α -phosphonyl-carbocations

The CV of $[56]^+$ shows a single reversible reduction wave at -0.63 V corresponding to the reduction of the acridinium substituent (Figure 89). The reversibility of this reduction implies that the neutral radical is a stable species. Reduction of $[56]^+$ with magnesium in acetonitrile/hexane produced a dark red hexane solution on which EPR measurements were done. The EPR of 56^\bullet shows a significant coupling to the phosphorus center of 19.7 G. Other hyperfine coupling constants used to simulate the obtained EPR spectrum can be found in Figure 90. Based on these parameters, it can be determined that the radical is predominantly acridine based with some delocalization onto the phosphorus center leading to the observed coupling.

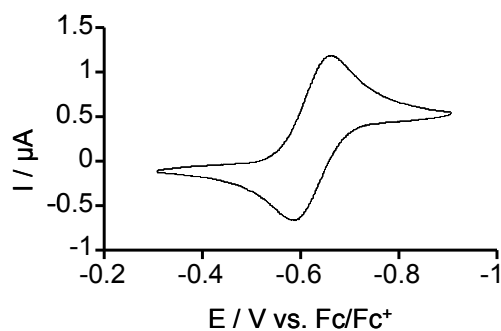


Figure 89. CV of $[56]^+$ in CH_3CN with a glassy carbon working electrode; scan rate 100 mV s^{-1} , $0.1 \text{ M NBu}_4\text{PF}_6$.

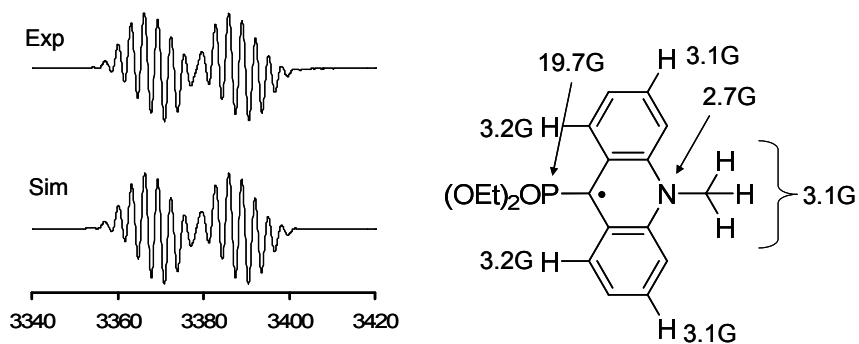


Figure 90. Experimental and simulated EPR spectra of 56^\bullet (left) and hyperfine coupling parameters (right)

4.6 Conclusions

In conclusion, the synthesis and structural characterization of α -phosphonio-carbocations $[50]^{2+}$, $[51]^{2+}$ and $[52]^{2+}$ is reported. Dication $[50]^{2+}$ shows remarkable reactivity with pyridines. These ligand exchange reactions imply that such α -phosphonio and α -pyridinium-carbocations can also be regarded as ligand stabilized carbocations. Reduction of the α -phosphonio-carbocation $[50]^{2+}$ affords an extremely stable acridine based radical which can be stored for extended periods of time without decomposition. However, the second reduction which would produce the ylid is irreversible suggesting the instability of the species. In addition to this, the first structure of an α -phosphonyl-carbocation is reported. Reduction of this cation again yields a very stable radical which has been characterized by EPR spectroscopy.

4.7 Experimental

Synthesis of [50][OTf]₂. Trimethylsilyltriflate (0.45 ml, 2.5 mmol) was added to a solution of 9-bromo-N-methylacridinium triflate (1.05 g, 2.5 mmol) and triphenylphosphine (0.65 g, 2.5 mmol) in PhCl (10 ml). The resulting solution was stirred overnight. After that time, Et₂O (30 ml) was added, the suspension filtered, and solid dried under reduced pressure to yield [50][OTf]₂ as a bright yellow solid. Yield: 90 % (1.68 g), ¹H NMR (CD₃CN, 400 MHz): δ 5.07 (s, 3 H), δ 7.53 (t, 2 H, ³J_{H-H} = 7.2 Hz), δ 7.73 (m, 6 H), δ 7.86 (d, 2 H, ³J_{H-H} = 8.8 Hz), δ 7.94 (m, 9 H), δ 8.31 (t, 2 H, ³J_{H-H} = 8.0 Hz), δ 8.77 (d, 2 H, ³J_{H-H} = 9.6 Hz), ³¹P NMR (CD₃CN, 161.8 MHz): δ 20.78. ¹³C NMR (CD₃CN 100.5 MHz): δ 43.04, 119.90 (d, CH_{Ph}, ¹J_{C-P} = 86.9 Hz), 121.04, 128.06 (d, CH_{Acrr}, ³J_{C-P} = 8.3 Hz), 130.303, 131.59 (d, C_{Acrr}, ²J_{C-P} = 6.8 Hz), 131.94 (d, C_{Acrr}, ³J_{C-P} = 13.7 Hz), 135.43 (d, C_{Acrr}, ²J_{C-P} = 10.7 Hz), 136.35, 137.02, 139.81, 142.86 (d, C_{Acrr}, ¹J_{C-P} = 9.1 Hz). Elemental analysis calcd. (%) for C₃₄H₂₆F₆NO₆PS₂: C 54.18, H 3.48; found: C 54.23, H 3.39.

Synthesis of [51][OTf]₂. Repeating the same procedure for [50][OTf]₂ and substituting (*p*-ClPh)₃P (0.91 g, 2.5 mmol) for triphenylphosphine yielded [51][OTf]₂ (1.59 g) in 75% yield. ¹H NMR (CD₃CN, 500 MHz): δ 5.06 (s, 3H), δ 7.62 (t, 2 H, ³J_{H-H} = 7.0 Hz), δ 7.75 (m, 6 H), δ 7.85 (m, 8 H), δ 8.34 (t, 2 H, ³J_{H-H} = 7.0 Hz), δ 8.77 (d, 2 H, ³J_{H-H} = 9.0 Hz). ³¹P NMR (CD₃CN, 161.8 MHz): δ 20.85. ¹³C NMR (CD₃CN 100.5 MHz): δ 43.10, 117.38, 121.08, 127.78 (d, CH_{Acrr}, ³J_{C-P} = 8.8 Hz), 130.57, 131.43 (d, C_{Acrr}, ²J_{C-P} = 7.6 Hz), 132.15 (d, C_{Acrr}, ³J_{C-P} = 14.9 Hz), 134.80 (d, C_{Acrr}, ¹J_{C-P} = 80.1 Hz), 136.98 (d,

C_{Acr} , ${}^2J_{\text{C-P}} = 12.3$ Hz) , 139.72, 142.83 (d, C_{Acr} , ${}^1J_{\text{C-P}} = 9.9$ Hz) , 143.82 (d, C_{Acr} , ${}^3J_{\text{C-P}} = 3.8$ Hz). Elemental analysis calcd. (%) for $\text{C}_{34}\text{H}_{23}\text{Cl}_3\text{F}_6\text{NO}_6\text{PS}_2$: C 47.65, H 2.71; found: C 47.78, H 2.81.

Synthesis of [52][OTf]₂. Repeating the same procedure for [50][OTf]₂ and substituting Ph_2MeP (0.50 g, 2.5 mmol) for triphenylphosphine yielded [52][OTf]₂ (1.12 g) in 65% yield. ${}^1\text{H}$ NMR (CD_3CN , 500 MHz): δ 3.10 (d, 3H, 12.99 Hz), δ 5.06 (s, 3H), δ 7.76 (m, 6 H), δ 7.84 (m, 4 H), δ 7.98 (m, 4 H), δ 8.37 (t, 2 H, ${}^3J_{\text{H-H}} = 7.50$ Hz) , δ 8.77 (d, 2 H, ${}^3J_{\text{H-H}} = 9.50$ Hz).

Synthesis of [53][OTf]₂. Pyridine (0.10 ml, 1.23 mmol) was added to a solution of [50][OTf]₂ (0.51 g, 0.68 mmol) in CH_3CN (5 ml) and stirred for 30 min. After that time, Et_2O (20 ml) was added, the suspension filtered, and the solid dried under reduced pressure to yield [53][OTf]₂. Yield 95% (0.40 g). ${}^1\text{H}$ NMR (CD_3CN , 400 MHz): δ 5.03 (s, 3 H), δ 7.68 (d, 2 H, ${}^3J_{\text{H-H}} = 8.3$ Hz), δ 8.06 (t, 2 H, ${}^3J_{\text{H-H}} = 6.8$ Hz), δ 8.56 (m, 4 H), δ 8.82 (d, 2 H, ${}^3J_{\text{H-H}} = 9.6$ Hz) , δ 9.09 (d, 2 H, ${}^3J_{\text{H-H}} = 5.6$ Hz) , δ 9.13 (t, 1 H, ${}^3J_{\text{H-H}} = 8.0$ Hz). ${}^{13}\text{C}$ NMR (CD_3CN 100.5 MHz): δ 41.50, 120.59, 123.67, 125.45, 131.09, 131.98, 141.19, 144.18, 147.11, 150.10, 151.70..

Synthesis of [54][OTf]₂. DMAP (0.085 g, 0.69 mmol) was added to a solution of [50][OTf]₂ (0.52 g, 0.69 mmol) in CH₃CN (5 ml) and stirred for 30 min. After that time, Et₂O (20 ml) was added, the suspension filtered, and the solid dried under reduced pressure to yield [54][OTf]₂. Yield: 95% (0.37 g), ¹H NMR (CD₃CN, 500 MHz): δ 3.42 (s, 6 H), δ 4.96 (s, 3 H), δ 7.28 (d, 2 H, ³J_{H-H} = 8.0 Hz), δ 7.96 (d, 2 H, ³J_{H-H} = 8.8 Hz), δ 8.07 (t, 2 H, ³J_{H-H} = 7.6 Hz), δ 8.21 (d, 2 H, ³J_{H-H} = 8.0 Hz), δ 8.51 (t, 2 H, ³J_{H-H} = 6.8 Hz), δ 8.77 (d, 2 H, ³J_{H-H} = 9.2 Hz). ¹³C NMR (CD₃CN 100.5 MHz): δ 40.98, 41.50, 109.60, 120.49, 124.84, 126.00, 131.28, 140.73, 142.74, 144.22, 151.82, 158.48. Elemental analysis calcd. (%) for C₂₃H₂₁F₆N₃O₆S₂: C 45.02, H 3.45; found: C 45.07, H 3.45.

Synthesis of [56][OTf]. *n*-BuLi (2.3 M in hexane, 1.7 ml, 3.8 mmol) was added to a suspension of 9-bromoacridine (1.00 g, 3.8 mmol) in Et₂O (10 ml) at -78°C and the resulting suspension was stirred for 10 min. After that time, diethylphosphorylchloride

(0.55 ml, 3.8 mmol) was added and the suspension stirred for 2 hours. After 2 hours, the reaction was filtered and solvent removed under reduced pressure to afford crude **55**. The solid was then washed with hexanes (2 x 5 ml) to remove impurities and used without further purification. Dry CH₂Cl₂ (10 ml) was then added followed by MeOTf (1.3 ml, 11.4 mmol) and the solution stirred for 1 hour. After that time, Et₂O (20 ml) was added and the suspension filtered to yield [**56**][OTf]. Yield 1.11 g, 60% overall yield based on 9-bromoacridine. ¹H NMR (CDCl₃, 500 MHz): δ 1.33 (t, 6 H, CH_{Me}, ³J_{H-H} = 7.0 Hz), δ 4.24 (m, 2 H), δ 4.40 (m, 2 H), δ 5.10 (s, 3 H), δ 7.95 (d, 2 H, ³J_{H-H} = 8.0 Hz), δ 7.37 (d, 2 H, ³J_{H-H} = 7.0 Hz), δ 8.76 (d, 2 H, ³J_{H-H} = 9.5 Hz), δ 9.66 (d, 2 H, ³J_{H-H} = 9.0 Hz). ³¹P NMR (CDCl₃, 161.8 MHz): δ 10.56. ¹³C NMR (CDCl₃, 100.5 MHz): δ 16.35 (d, CH_{Me}, ³J_{C-P} = 6.1 Hz), 41.25, 64.52 (d, CH_{Me}, ²J_{C-P} = 5.7 Hz), 119.19, 128.68, 128.78, 130.21 (d, CH_{Acr}, ³J_{C-P} = 3.4 Hz), 138.90, 141.42 (d, C_{Acr}, ²J_{C-P} = 12.9 Hz), 146.4 (d, C_{Acr}, ¹J_{C-P} = 168.2 Hz). Elemental analysis calcd. (%) for C₁₉H₂₁F₃NO₆PS: C 47.60, H 4.42; found: C 47.06, H 4.10.

CHAPTER V

FLUORIDE ION COMPLEXATION BY A B₂/Hg HETERONUCLEAR
TRIDENTATE LEWIS ACID*

5.1 Background

5.1.1 Diboranes as anion complexation agents

Diboranes, specifically those based on the 1,8-naphthalenediyl and *o*-phenylene scaffold, have been used extensively to chelate various small anions. Katz has shown that 1,8-bis(dimethylboryl)naphthalene **57** effectively chelates anions such as fluoride, hydride and hydroxide (Figure 91).^{1,80} The resulting compounds feature bridging interactions that are relatively symmetrical with the anion residing between the dimethylboryl moieties. The hydride bridged derivative **58** has been successfully characterized by X-ray crystallography and displays a B-H-B 3c-2e bond with bond lengths of 1.49(5) and 1.20(5) Å and a B-H-B bond angle of 142(4)°. Though they were not successfully crystallized, the fluoride and hydroxide adducts **59** and **60** also appear to adopt symmetrical structures. Indeed, the ¹H and ¹³C NMR spectra of all three derivatives reveal symmetrical products in agreement with a chelate structure. Furthermore, **59** does not undergo exchange between **57** and **59** upon heating (conditions

* Reprinted in part with permission from, "Fluoride Ion Complexation by a B₂/Hg Heteronuclear Tridentate Lewis Acid"; C. L. Dorsey, P. Jewula, T. W. Hudnall, J. D. Hoefelmeyer, T. J. Taylor, N. R. Honesty, C.-W. Chiu, M. Schulte, F. P. Gabbaï; *Dalton Trans.*, **2008**, 33, 4442-4450, Copyright 2008 by the Royal Society of Chemistry.

under which mixtures of Et_3B and Et_3BF rapidly equilibrate) which can be attributed to cooperation of the two dimethylboryl units in binding the fluoride anion.

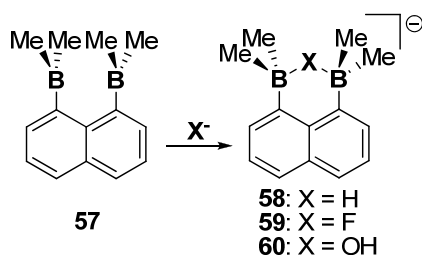


Figure 91. Bridged diboranes **58**, **59** and **60**

The *o*-phenylene scaffold has also been used effectively to promote chelation of a variety of anions. Piers and co-workers have shown that 1,2-bis(bis(pentafluorophenyl)boryl)tetrafluorobenzene **61** effectively chelates a variety of anions including hydroxide, methoxide, azide, fluoride and chloride (Figure 92).⁸¹⁻⁸⁴ Complexation of these anions again occurs symmetrically between the boron centers according to NMR and X-ray crystallography. Although the perfluorophenyl substituents substantially enhance the Lewis acidity of the borane moieties, they impair the use of **61** as an anion sensor by increasing its sensitivity towards oxygen and water.

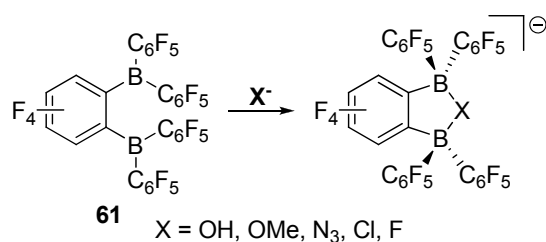


Figure 92. Bridging in *o*-phenylene derivatives

5.1.2 Diboranes for the selective binding of fluoride

Similar results have been published by the Gabbai group. Utilizing the same 1,8-naphthalenediyl scaffold, they have shown that diboranes substituted with aryl groups can selectively bind fluoride (Figure 93). Compounds **62** and **63** have both synthesized and their fluoride adducts crystallized and analyzed by X-ray diffraction.^{3,85} The bonding cavity between the borane moieties appears to be too small to capture larger anions. This is more than likely due to the steric requirements of the dimesityl boryl moiety that occupies one side of the scaffold. Also, DFT studies carried out on **63** and various model compounds have shown that the enhanced fluoride affinity for 1,8-naphthalenediyl diboranes can be partially attributed to the relief of steric crowding upon binding fluoride. This helps support the argument that sterics play a large role in both binding and stabilizing the bridging species. Fluoride binding studies have been carried out on both **62** and **63**, and the binding constants determined in THF. For both derivatives, the binding constant has been calculated to be greater than 5×10^9 . Though both diboranes **62** and **63** slowly decompose in the presence of H₂O, neither [**62**-μ₂-F]⁻

or $[\mathbf{63}\text{-}\mu_2\text{-F}]^-$ lose fluoride upon addition of water again suggesting strong chelation of fluoride by both bidentate diboranes.

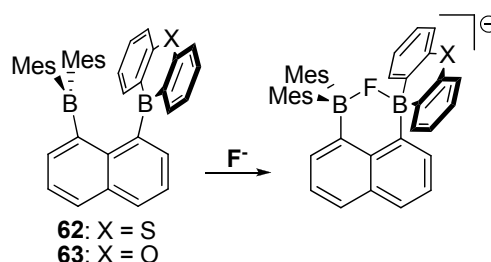


Figure 93. Fluoride binding of **62** and **63**

5.1.3 Hybrid boron/mercury systems for selective fluoride binding

The Gabbai group has also been interested in systems in which one of the borane moieties is substituted by a different Lewis acidic main group element. One of the elements that our group has been most interested in is mercury. Mercury was chosen for several reasons. First, it has been shown that mercury can act as a Lewis acid when decorated with electron withdrawing moieties, and heavy atoms such as mercury help to enhance phosphorescence of chromophores through spin-orbit coupling.⁸⁶ The first compound of this type synthesized by the Gabbai group was **64** (Figure 94).⁸⁷ This molecule features a dimesitylboryl substituent and a perfluorophenylmercury substituent on the 1,8-naphthalenediyl scaffold. Reaction of **64** with fluoride yields the fluoride adduct **65**. Examination of the solid state structure of **65** reveals that the fluoride is indeed bound between the two Lewis acidic centers with a B-F bond length of 1.483(4) Å and a Hg-F interaction of 2.589(2) Å. Unlike the diborane analogs mentioned

previously, however, **64** is able to bind fluoride in the presence of H₂O. In a 90/10 (v/v) THF/H₂O mixed solvent system, **64** is able to capture fluoride with a binding constant of $2.3(\pm 0.2) \times 10^4 \text{ M}^{-1}$. Another feature of **64** is that upon conversion to **65**, there is a notable change in the emission spectrum. This change in the emission properties can easily be seen with the naked eye as the free Lewis acid **64** emits red while the fluoride adduct **65** emits pale green in the solid state. Spin-orbit coupling from the mercury center aids in enhancing the phosphorescence of these two compounds. The observed change is due to the “quenching” of the dimesitylboryl naphthalene chromophore upon fluoride binding. This is caused by the disruption of conjugation through the boron p-orbital. When this occurs, the resultant emission spectrum only originates from the naphthalene chromophore.

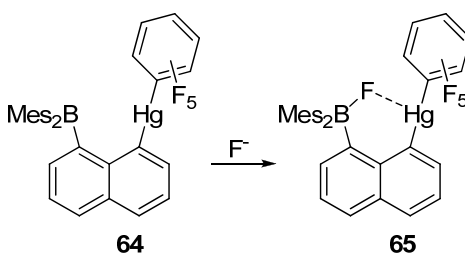


Figure 94. Fluoride binding of **64**

The Gabbai group has also studied the effects of placing cationic substituents on the mercury. Compound **66** features a cationic phenylene substituent pendant to the mercury (Figure 95).⁸⁸ This compound can effectively bind fluoride much like **64** to give **67**. Again, chelation of the fluoride anion can be seen in the solid state structure of

67. The B-F bond of 1.474(8) Å and the Hg-F interaction of 2.618(3) Å confirm the cooperation of the two centers in binding the fluoride anion. When titrated with fluoride in the same 90/10 (v/v) THF/H₂O mixture as before, **67** is able to bind fluoride with a stability constant of $6.2 (\pm 0.2) \times 10^4 \text{ M}^{-1}$ confirming that cationic substituents on the mercury center can aid in the binding of fluoride.

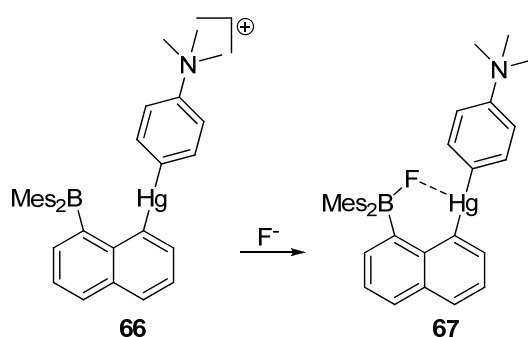


Figure 95. Fluoride binding of **66**

5.2 Introduction

As shown above, several chelating naphthalene-based boranes have been prepared and investigated. To further our understanding of the chemistry of such compounds, we have now decided to compare the fluoride binding properties of the neutral diborane **68**⁸⁹ to that of the neutral B/Hg bidentate Lewis acid **69** (Figure 96).⁸⁸ We have also investigated the synthesis, characterization and fluoride binding properties of a novel B/Hg/B trifunctional Lewis acid.

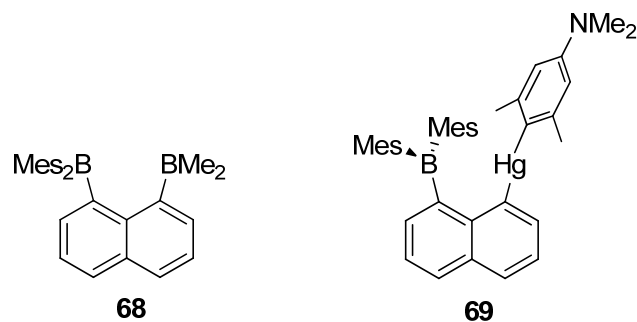


Figure 96. Previously synthesized derivatives **68** and **69**

5.3 Synthesis and spectroscopic characterization*

We have previously described the synthesis of **68**⁸⁹ and **69**⁸⁸ which were obtained by reaction of $[\text{Li}(\text{THF})_4][1,8\text{-}\mu\text{-(Mes}_2\text{B)C}_{10}\text{H}_6]$ ⁸⁹ with Me_2BBr and $(2,6\text{-Me}_2\text{-4-Me}_2\text{NC}_6\text{H}_2)\text{HgCl}$, respectively. We have carried out the reaction of this borate with half an equivalent of HgCl_2 and found that it affords the B/Hg/B trifunctional Lewis acid **70** in 70% yield (Figure 97).

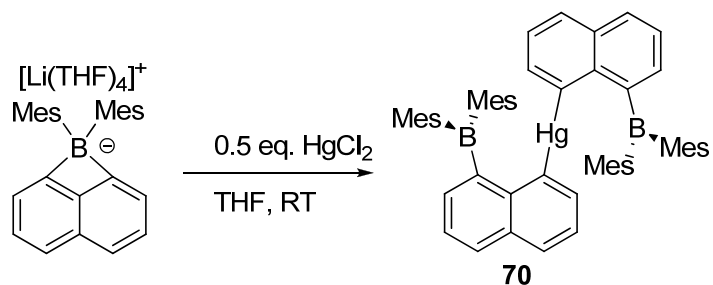


Figure 97. Synthesis of **70**

* Original synthesis of **70** carried out by Marcus Schulte

Compounds **70** has been characterized by multinuclear NMR spectroscopy and elemental analysis. The ^1H NMR spectrum exhibits six distinct resonances that correspond to the aromatic CH groups of the unsymmetrically substituted naphthalene backbone. In the case of **70**, the aryl and methyl proton resonances of the mesityl groups are split into broad multiple signals thus indicating the existence of a congested structure. The ^{11}B NMR signal detected at 72.3 for **70** and 72.1 ppm for confirms the presence of a base-free trigonal planar boron center.^{87,88} The ^{199}Hg resonance of **70** (-800 ppm, CDCl_3) is comparable to that of diphenylmercury (-820 ppm, d_6 -DMSO).^{90,91}

5.4 Structure of **70***

Compound **70** crystallizes in the monoclinic space group $P2_1/c$ with half a molecule of interstitial chloroform (Figure 98, Table 1). The boron atoms B(1) and B(2) adopt a trigonal planar geometry ($\Sigma_{(\text{C-B-C})} = 359.1^\circ, 359.4^\circ$) and are separated from the mercury atom Hg(1) by 3.462(15) Å and 3.463(14) Å, respectively. These distances are slightly longer than the Hg-B separation of 3.3 Å measured in for compounds **64** and **66**^{87,88} which probably results from the greater degree of steric crowding present in **70**. The mercury center Hg(1) adopts a distorted linear geometry (C(1)-Hg(1)-C(31) $168.1(4)^\circ$) and forms short interactions of 3.156(12) Å and 3.132(12) Å with the mesityl *ipso*-carbon atoms C(21) and C(41). These short distances indicate the presence of a secondary Hg- π interaction. When compared to intermolecular Hg- π interactions,^{92,93} these distances appear relatively short and might be partly enforced by the rigid

* Structure determined by Dr. Thomas J. Taylor

naphthalene backbone. The two trigonal planar boryl moieties which are separated by a B-B distance of 6.14 Å; form a dihedral angle of only 29.4° and are oriented in a co-facial fashion with respect to one another.

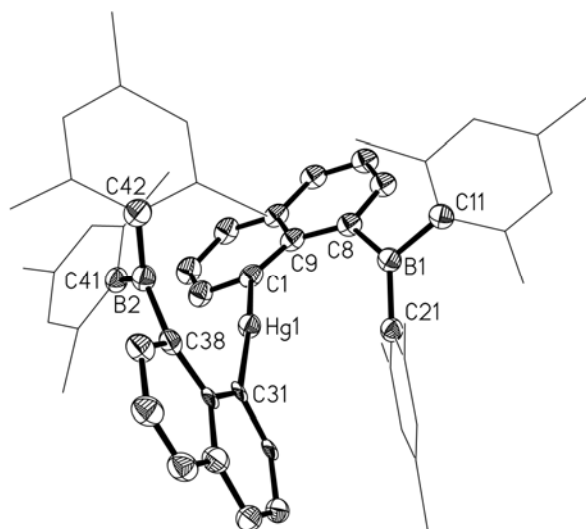


Figure 98. ORTEP view of **70** (50% ellipsoid), H atoms are omitted and the mesityl groups are represented by thin lines. Selected distances [Å] and angles [deg]: Hg(1)-C(31) 2.036(10), Hg(1)-C(1) 2.172(12), Hg(1)-C(41) 3.132(12), Hg(1)-C(21) 3.156(12), Hg(1)-B(1) 3.462(15), Hg(1)-B(2) 3.463(14), B(1)-C(21) 1.549(19), B(1)-C(8) 1.612(19), B(1)-C(11) 1.63(2), B(1)-B(2) 6.139(17), C(1)-C(9) 1.375(17), C(1)-C(2) 1.380(17), C(2)-C(3) 1.438(18), B(2)-C(51) 1.55(2), B(2)-C(38) 1.580(18), B(2)-C(41) 1.589(18), C(31)-Hg(1)-C(1) 168.1(4), C(21)-B(1)-C(8) 125.7(12), C(21)-B(1)-C(11) 119.3(11), C(8)-B(1)-C(11) 114.1(11), C(51)-B(2)-C(38) 113.6(11), C(51)-B(2)-C(41) 121.2(11), C(38)-B(2)-C(41) 124.6(12).

Table 19. Crystal Data, Data Collection, and Structure Refinement for **70-0.5(CHCl₃)**.

Crystal data	70-0.5(CHCl₃)
Formula	C _{56.50} H _{56.50} B ₂ Cl _{1.50} Hg
M _r	1010.90
crystal size (mm ³)	0.08 x 0.05 x 0.015
crystal system	Monoclinic
space group	P2 ₁ /c
a (Å)	12.1981(19)
b (Å)	27.747(4)
c (Å)	14.241(3)
α (°)	90.0000
β (°)	98.204(7)
γ (°)	90.0000
V (Å ³)	4770.6(15)
Z	4
ρ _{calc} (g cm ⁻³)	1.407
μ (mm ⁻¹)	6.822
F(000)	2044
Data Collection	
T (K)	110(2)
scan mode	ω
hkl range	-13 → +13, -31 → +31, -15 → +15
measd reflns	31362
unique reflns [R _{int}]	6768 [0.1001]
reflns used for refinement	6768
Refinement	
refined parameters	582
GooF	1.012
R1, ^a wR2 ^b all data	0.1167, 0.1860
ρ _{fin} (max/min) (e Å ⁻³)	3.103, -1.782

5.5 Calculations

The structure of **68**, **69** and **70** have been optimized computationally using density functional theory (DFT) methods at the B3LYP level of theory with mixed basis sets. The fully optimized geometry of **68** and **70** are close to that observed in the solid state. In particular, the calculated B-B separation of 3.31 Å in **68** and the B-Hg separation of 3.51 Å in **70** are comparable to those observed in the crystal structure (B-B = 3.206 Å for **68**;⁸⁹ av. B-Hg = 3.46 Å for **70**).⁸⁸ Examination of the orbitals indicates that the LUMO in **68**, **69**, and **70** bears a large contribution from the 2p-orbitals of the boron centers of the dimesityl boryl moieties with essentially no participation from the other Lewis acidic centers (Figure 99). In the case of **68**, the +I effect of the methyl group as well as hyperconjugation⁹⁴ probably raise the energy of the empty p-orbital of the Me₂B moiety thus precluding its participation in the LUMO. For **69** and **70**, the mercury atom vacant orbitals might be intrinsically too high in energy to participate in the LUMO.

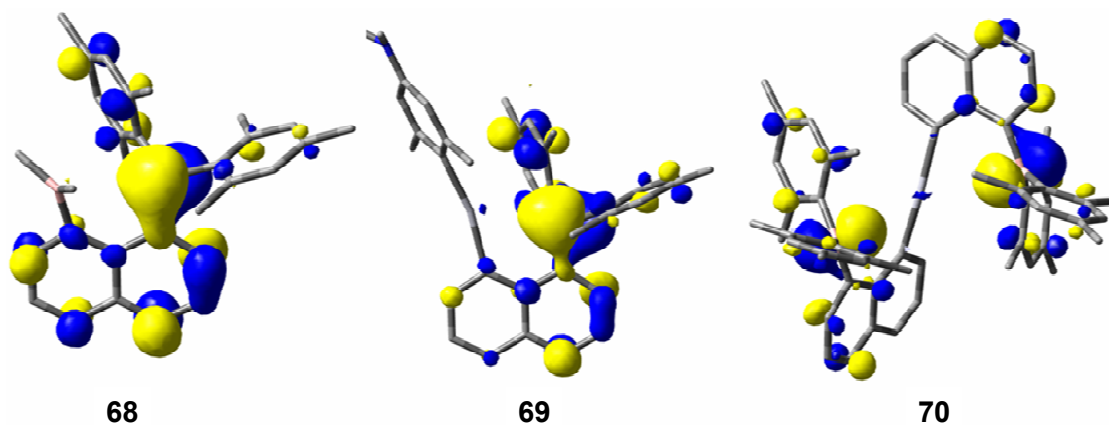


Figure 99. Optimized geometry and LUMO of **68**, **69** and **70** (isodensity value = 0.04)

5.6 Electrochemistry*

The cyclic voltammogram of **68** shows a reversible reduction wave at $E_{1/2}$ -2.31 V (vs. Fc/Fc^+) which is followed by an irreversible one at E_{peak} -2.93 V (Figure 4). As in the case of simple triarylboranes such as Mes_3B ,^{15-22,25,26} these two waves are respectively assigned to the reversible one-electron and irreversible two-electron reduction of the dimesitylboryl moiety. This electrochemical study also suggests that the dimethylboryl moiety is not electroactive in the potential window studied. In the case of **69**, the cyclic voltammogram in THF shows a reversible reduction wave at $E_{1/2}$ -2.26 V (vs. Fc/Fc^+) which is followed by undefined irreversible processes, again in agreement with the reversible one-electron reduction of the dimesitylboryl moiety (Figure 100). Although the electrochemical behavior of **68** and **69** is similar to those of triarylboranes, we note that their reduction potentials are markedly more positive than those of other triaryl

* Electrochemistry done in collaboration with Pawel Jewula, a visiting REU student

boranes such as dimesityl-1-naphthylborane which is reduced at -2.41 V (vs. Fc/Fc⁺).³² This difference suggests that the Me₂B moiety in **68**⁸⁹ and the (2,6-Me₂-4-Me₂NC₆H₂)Hg⁸⁸ moiety in **69** increases the electrophilicity of the derivatives. The cyclic voltammogram of **70** in THF shows two reversible reduction waves at E_{1/2} -2.31 V and -2.61 V corresponding to the reduction of the two boron centers. As expected, the potential of the first reduction wave is close to that measured for **68** and **69** and can be regarded as corresponding to the reduction of the first boron center. The relatively large ΔE_{1/2} observed between these two waves indicate substantial coupling of the two electroactive boryl moieties of **70**. Because mercury should not efficiently mediate π-conjugation, we propose that this coupling has electrostatic origins and is magnified by the proximity of the two boryl units.

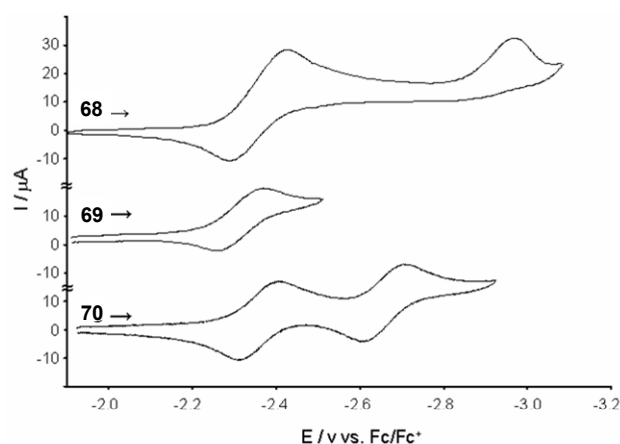


Figure 100. Cyclic voltammograms of **68** (top) **69** (middle) and **70** (bottom) in THF with a glassy-carbon working electrode (0.3 M *n*Bu₄NPF₆). Scan rates: $\nu = 100 \text{ mV s}^{-1}$.

5.7 Fluoride anion binding*

In previous reports we have shown that bidentate diboranes such as **62** and **63** are well adapted for the complexation of fluoride anions.^{3,11,85} We have also shown that the reduction waves present in the voltammogram of such diboranes could serve to monitor fluoride binding in solution.⁸⁵ As part of the present studies, we decided to determine whether a similar behavior would be observed for heteronuclear B/Hg derivatives such as **69** and **70**. Addition of fluoride to a THF solution of **69** or **70** containing $n\text{BuN}_4\text{PF}_6$ as a supporting electrolyte results in the progressive disappearance of the reduction wave, which is no longer detected after the addition of 1 equiv. of fluoride (Figure 101). The disappearance of this wave results from coordination of a fluoride anion to the dimesitylboron center which can no longer be reduced because of coordinative saturation (Figure 102, Figure 103). In the case of **70**, addition of fluoride results in the rapid disappearance of the first reduction wave at -2.26 V which is no longer visible after the addition of 1 equiv. of the anion (Figure 103). Interestingly, the potential of the second wave undergoes an anodic shift of 50-60 mV. These observations can be interpreted by invoking the formation of a 1:1 complex [**70**- μ_2 -F] in which the fluoride binds to only one boron center. The reduction observed at -2.66 V thus corresponds to the reduction of the remaining tricoordinate boron center (Figure 101). Further addition of fluoride only leads to a more progressive decrease of the remaining reduction wave suggesting that binding of a second fluoride anion is less favorable than the first one.

* Anion binding studies done in collaboration with Dr. Todd W. Hudnall and Pawel Jewula

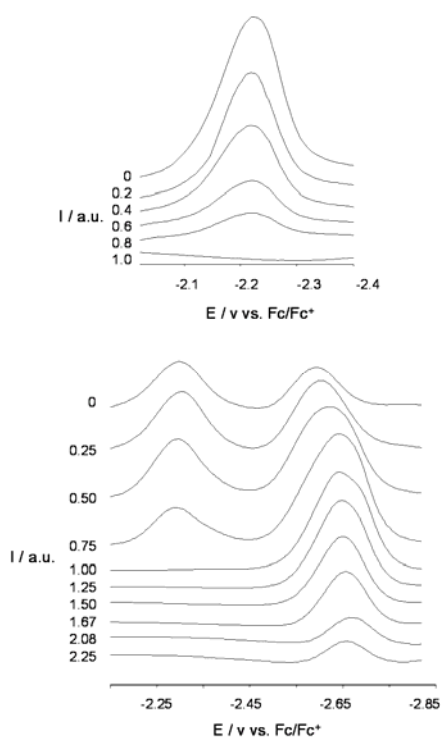


Figure 101. Changes in the differential pulsed voltammogram of **69** (top) and **70** (bottom) observed upon the addition of $n\text{Bu}_4\text{NF}$ to a THF solution (0.3 M).

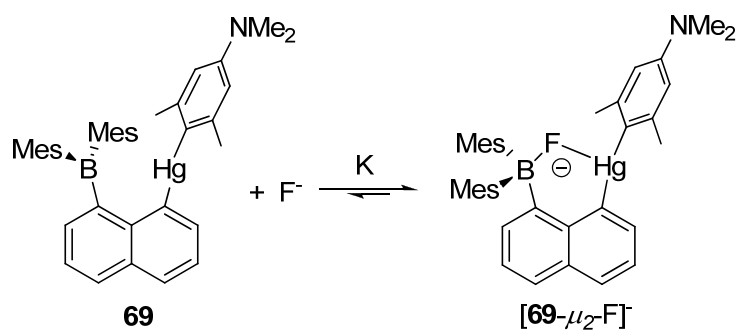


Figure 102. Equilibrium between **69** and $[\mathbf{69}-\mu_2\text{-F}]^-$

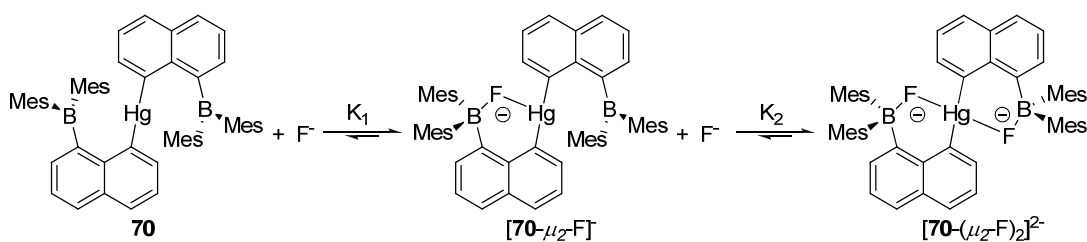


Figure 103. Equilibrium between **70**, $[\mathbf{70}-\mu_2\text{-F}]^-$ and $[\mathbf{70}-(\mu_2\text{-F})_2]^{2-}$

Further insights into the fluoride binding behavior of **70** were gained from UV-vis titration studies in THF. The addition of TBAF to a THF solution of **70** ($\epsilon_{360} = 17400 \text{ M}^{-1} \text{ cm}^{-1}$) results in a decrease of the absorbance at 360 nm caused by coordinative saturation of the boron center (Figure 104). Interestingly, addition of up to one equivalent of fluoride anion leads to a linear decrease of the absorbance. At exactly one equivalent of added fluoride, the isotherm shows a distinct break and addition of over 1 equiv of fluoride leads to a much more progressive decrease of the absorbance. These observations can be rationalized based on the following argument. Addition of the first equivalent essentially leads to the quantitative formation of the 1:1 adduct $[\mathbf{70}-\mu_2\text{-F}]^-$ ($\epsilon_{360} = 8200 \text{ M}^{-1} \text{ cm}^{-1}$). Addition of a second fluoride anion to produce $[\mathbf{70}-(\mu_2\text{-F})_2]^{2-}$ is much less favorable explaining the more progressive decrease of the absorbance (Scheme 3). Because fluoride binding to **70** occurs in two very distinct regimes, the fluoride binding constants can be evaluated independently. The first fluoride binding constant K_1 exceeds the value of 10^8 M^{-1} measurable by a UV-vis titration. Fitting of the data obtained above 1 equiv. of added fluoride affords $K_2 = 5.2 (0.4) 10^3 \text{ M}^{-1}$. These results are in agreement with the conclusions derived from the fluoride binding

experiments monitored by differential pulsed voltammetry which also showed that binding of the first fluoride anion is much more favorable than the second one. These results can be easily understood by considering the fact that the binding of the second fluoride anion would lead to the formation of a dianion and is therefore electrostatically and possibly sterically disfavored.

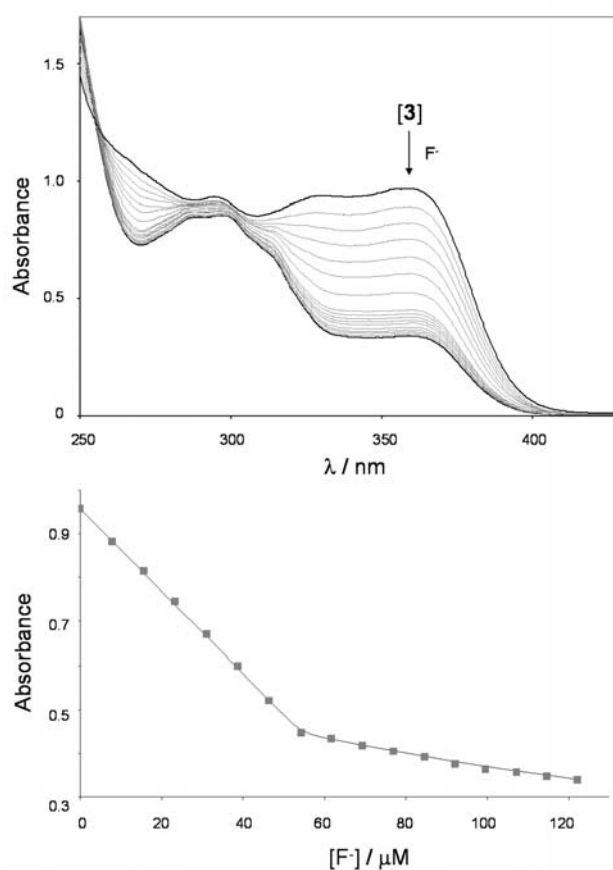


Figure 104. Top: Changes in the UV-vis absorption spectra of a solution of **70** (3 mL, 5.5×10^{-5} M in THF) upon addition of a TBAF solution (4.7×10^{-3} M in THF). Bottom; Binding isotherm obtained by monitoring the absorbance at 360 nm.

5.8 Comparative studies*

Having established that compound **70** complexes fluoride, we decided to compare its fluoride affinity to that of **68** and **69**. Because the fluoride binding constants measured in THF are too elevated to be accurately compared, we decided to carry out these studies in CHCl_3 which, we have shown,⁹⁵ is a more competitive medium. Spectrophotometric titrations carried out in this solvent indicate that the fluoride binding constants of **68**, **69** and **70** are respectively equal to $5.0 (\pm 0.2) \times 10^5 \text{ M}^{-1}$, $1.0 (\pm 0.2) \times 10^3 \text{ M}^{-1}$ and $1.7 (\pm 0.1) \times 10^3 \text{ M}^{-1}$ (Figure 105, Figure 106, Figure 107). These results show that diboranes do have a higher fluoride affinity than heteronuclear B/Hg compounds such as **69** and **70**. It is also interesting to note that the fluoride binding constants of **69** and **70** are slightly lower than that measured for **64** in the same solvent ($2.1(\pm 0.2) \times 10^4 \text{ M}^{-1}$).⁹⁵ This latter observation indicates that electron-withdrawing pentafluorophenyl group of **64** effectively increased the fluoride affinity of this type of receptors.

* Comparative studies done in collaboration with Dr. Todd W. Hudnall and Nicole R. Honesty

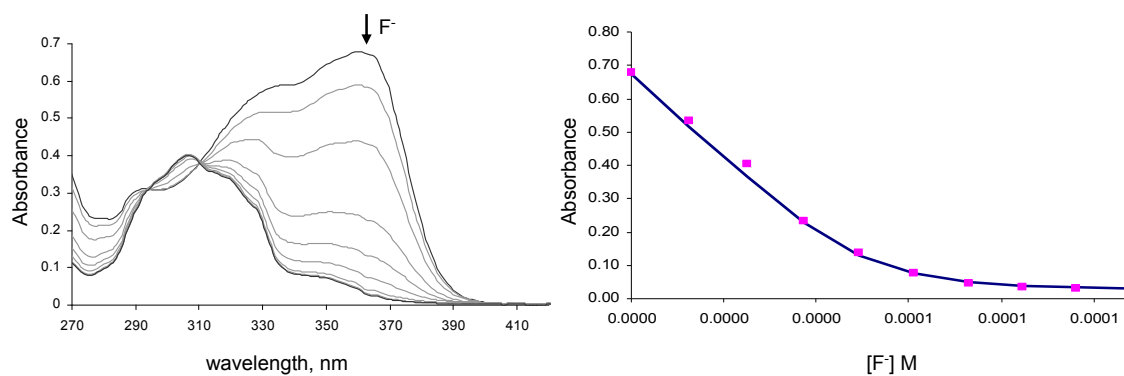


Figure 105. (left): Changes in the UV-vis absorption spectrum of **68** (3.0 mL, 5.1896×10^{-5} M, in chloroform) upon addition of a TBAF solution (1.90×10^{-2} M, in chloroform). (right): 1:1 binding isotherm for the formation of $[68-\mu_2-F]$.

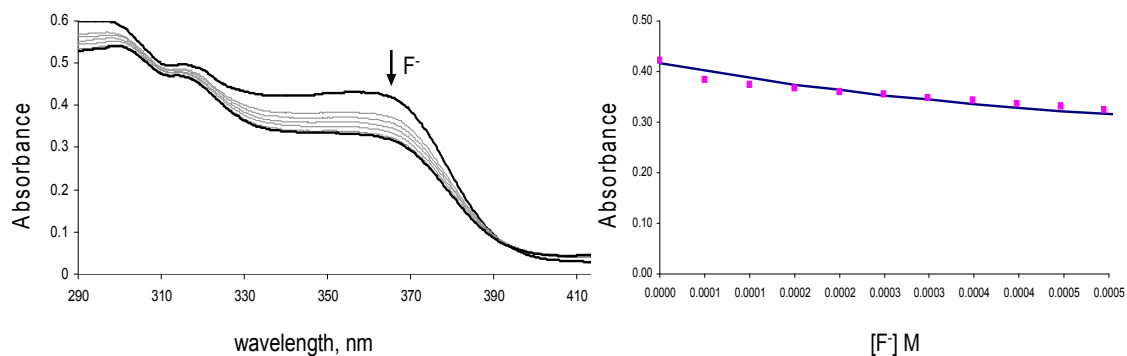


Figure 106. (left): Changes in the UV-vis absorption spectrum of **69** (3.0 mL, 5.00×10^{-5} M, in chloroform) upon addition of a TBAF solution (3.02×10^{-2} M, in chloroform). (right): 1:1 binding isotherm for the formation of $[69-\mu_2-F]$.

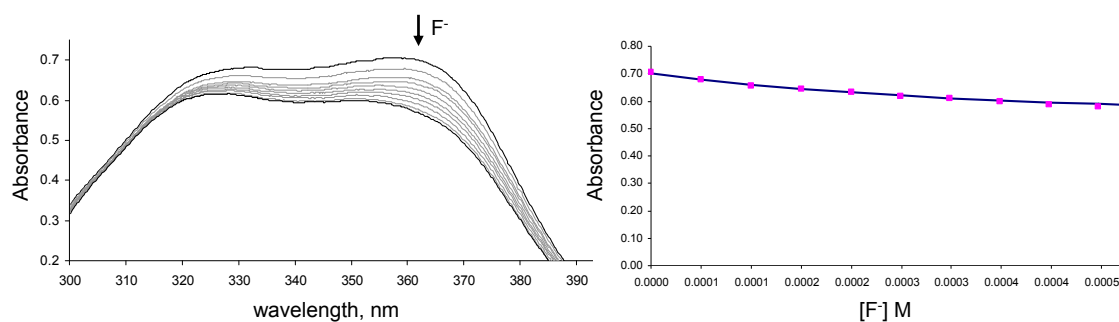


Figure 107. (left): Changes in the UV-vis absorption spectrum of **70** (3.0 mL, 2.525×10^{-5} M, in chloroform) upon addition of a TBAF solution (3.02×10^{-2} M, in chloroform). (right): 1:1 binding isotherm for the formation of $[\mathbf{70}\text{-}\mu_2\text{-F}]$.

In order to further rationalize these results, we decided to investigate the structures of the fluoride complexes. We were able to obtain single crystals of $[\text{S}(\text{NMe}_2)_3][\mathbf{68}\text{-}\mu_2\text{-F}]$ and $[\text{S}(\text{NMe}_2)_3][\mathbf{70}\text{-}\mu_2\text{-F}]$. The salt $[\text{S}(\text{NMe}_2)_3][\mathbf{68}\text{-}\mu_2\text{-F}]$ crystallizes in the $P2_1/c$ monoclinic space group with four molecules in the unit cell (Figure 108, **Table 20**). The fluorine atom F(1) is bound to both boron centers via B-F bonds of 1.596(5) (B(1)-F(1)) and 1.604(7) Å (B(2)-F(1)). These bonds are comparable to or slightly shorter than those measured in the fluoride adduct of 1-(dimesitylboryl)-8-(10'-bora-9'-oxanthryl)naphthalene (av. 1.63 Å)⁸⁵ and 1-(dimesitylboryl)-8-(10'-bora-9'-thiaanthryl)naphthalene (av. 1.61 Å)³ which may result from the lower steric requirement of the dimethylboryl moiety present in **68**. It remains that these bonds are longer than those formed in the fluoride adduct of $[\text{C}_6\text{F}_4\text{-1,2-}[(\text{BF}_2)_2]]$ which possesses more Lewis acidic and accessible difluoroboryl moieties.⁸¹ They are also longer than those in triarylfluoroborate anions (~ 1.48 Å)⁹⁵⁻⁹⁷ as expected from the bridging location

of the fluorine atom. The cooperative binding of the fluoride anion leads to pyramidalization of both boron centers as indicated by the sum of the C-B-C angles ($\Sigma_{C-B1-C} = 345.2^\circ$; $\Sigma_{C-B2-C} = 344.8^\circ$).

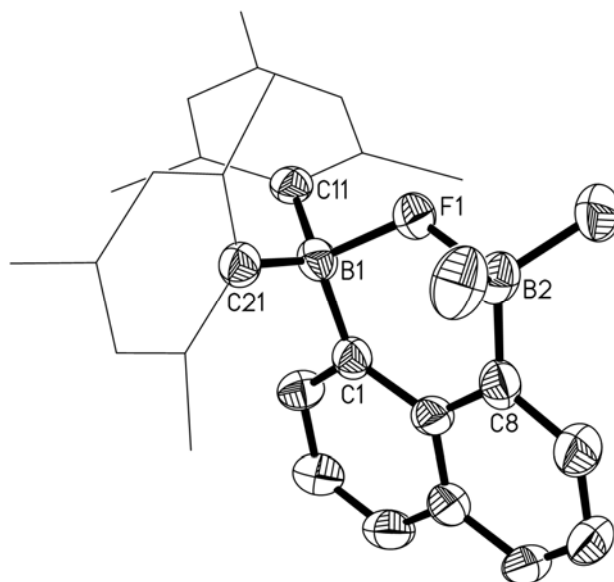


Figure 108. ORTEP view of $[68-\mu_2-F]^-$ in $[S(NMe_2)_3][68-\mu_2-F]$ (50% ellipsoid). H atoms are omitted and the mesityl groups are represented by thin lines. Selected distances [\AA] and angles [deg]: B(1)-F(1) 1.596(5), B(2)-F(1) 1.604(5), B(1)-C(1) 1.612(6), B(1)-C(11) 1.633(6), B(1)-C(21) 1.663(6), B(1)-B(2) 2.922(7), B(2)-C(8) 1.614(7), B(2)-C(31) 1.598(7), B(2)-C(32) 1.602(7); B(1)-F(1)-B(2) 126.0(3), C(1)-B(1)-F(1) 103.8(3), C(8)-B(2)-F(1) 105.2(3), C(1)-B(1)-C(11) 110.1(3), C(1)-B(1)-C(21) 117.4(3), C(11)-B(1)-C(21) 117.7(3), C(8)-B(2)-C(31) 112.1(4), C(8)-B(1)-C(32) 113.4(4), C(31)-B(2)-C(32) 114.2(4).

Table 20. Crystal Data, Data Collection, and Structure Refinement for [S(NMe₂)₃][**68**-μ₂-F].

Crystal data	[S(NMe ₂) ₃][68 -μ ₂ -F]
Formula	C ₃₆ H ₅₂ B ₂ FN ₃ S
M _r	599.49
crystal size (mm ³)	0.23 × 0.20 × 0.20
crystal system	Monoclinic
space group	P2 ₁ /c
a (Å)	10.5814(15)
b (Å)	17.441(2)
c (Å)	20.6449(19)
α (°)	90.0000
β (°)	114.742(5)
γ (°)	90.0000
V (Å ³)	3460.3(7)
Z	4
ρ _{calc} (g cm ⁻³)	1.151
μ (mm ⁻¹)	0.127
F(000)	1296
Data Collection	
T (K)	110(2)
scan mode	ω
hkl range	-9 → +1, -19 → +19, -23 → +17
measd reflns	15743
unique reflns [R _{int}]	5424 [0.0460]
reflns used for refinement	5424
Refinement	
refined parameters	388
Goof	1.008
R1, ^a wR2 ^b all data	0.1297, 0.2433
ρ _{fin} (max/min) (e Å ⁻³)	0.842, -0.405

Salt $[\text{S}(\text{NMe}_2)_3][\mathbf{70}\text{-}\mu_2\text{-F}]$ belongs to the monoclinic Cc space group with four molecules in the unit cell (Figure 109, Table 21). The fluorine atom F(1) bridges the mercury center (Hg1) and one of the two boron centers (B1). The resulting B(1)-F(1) bond length of 1.487(10) Å is close to those found in **65** (1.483(4) Å)⁸⁷ and **67** (av. 1.48 Å)⁸⁸ and does not appear lengthened when compared to that found in simple triarylfluoroborates.⁹⁵⁻⁹⁷ As in **65** and **67** which possess Hg-F bond lengths in the 2.59-2.63 Å range, the Hg(1)-F(1) bond of 2.576(4) Å measured in $[\mathbf{70}\text{-}\mu_2\text{-F}]^-$ is well within the sum of the van der Waals radii of mercury (1.75 Å)⁹⁸ and fluorine (1.30-1.38 Å) thus indicating the presence of a strong secondary interaction.^{56,99,100} Coordination of the fluoride results in a pyramidalization of the boron centers ($\Sigma_{(\text{C-B}(1)\text{-C})} = 338.9^\circ$) but does not noticeably affect the C(1)-Hg(1)-C(31) angle which is equal to 169.0(4)°. The coordination geometry of the remaining boron center B(2) is not affected by the chelation of a fluoride ion. It remains trigonal planar and the B(2)-Hg(1) distance of 3.445(10) Å is essentially identical to that observed in **70**.

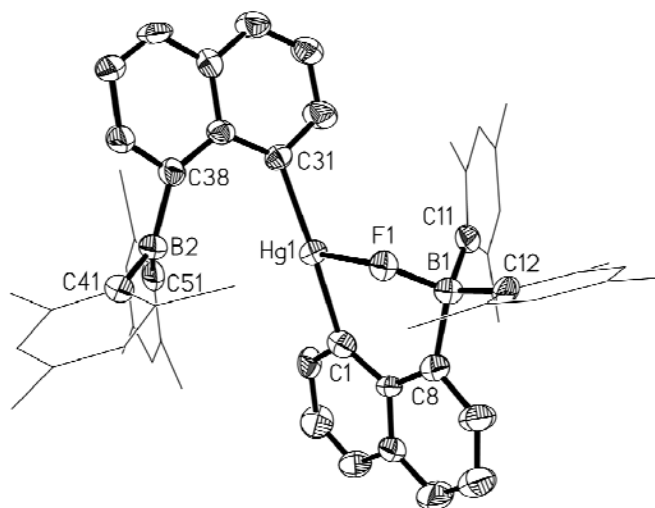


Figure 109. ORTEP view of $[70-\mu_2-F]^-$ in $[S(NMe_2)_3][70-\mu_2-F]$ (50% ellipsoid). H atoms are omitted and the mesityl groups are represented by thin lines. Selected distances [\AA] and angles [deg]: Hg(1)-C(1) 2.079(14), Hg(1)-C(31) 2.119(12), Hg(1)-F(1) 2.576(4), B(1)-F(1) 1.487(10), B(1)-C(11) 1.672(14), B(1)-C(8) 1.655(12), B(1)-C(21) 1.685(16), B(2)-C(41) 1.567(14), B(2)-C(38) 1.592(13), B(2)-C(51) 1.576(16), C(1)-Hg(1)-C(31) 169.0(4), C(1)-Hg(1)-F(1) 86.4(3), C(31)-Hg(1)-F(1) 104.3(3), F(1)-B(1)-C(11) 104.8(6), F(1)-B(1)-C(8) 106.4(6), C(11)-B(1)-C(8) 116.1(7), F(1)-B(1)-C(21) 105.7(7), C(11)-B(1)-C(21) 113.2(8), C(8)-B(1)-C(21) 109.6(7), C(41)-B(2)-C(38) 116.6(9), C(41)-B(2)-C(51) 119.5(9), C(38)-B(2)-C(51) 122.9(8), B(1)-F(1)-Hg(1) 104.7(4).

Table 21. Crystal Data, Data Collection, and Structure Refinement for [S(NMe₂)₃][**70**- μ_2 -F].

Crystal data	[S(NMe ₂) ₃][70 - μ_2 -F]
Formula	C ₆₂ H ₇₄ B ₂ FHgN ₃ S
M _r	1134.51
crystal size (mm ³)	0.23 × 0.20 × 0.20
crystal system	.014 x .01 x .01
space group	Cc
a (Å)	11.9011(9)
b (Å)	19.2576(14)
c (Å)	23.5739(17)
α (°)	90.0000
β (°)	95.015(2)
γ (°)	90.0000
V (Å ³)	5382.1(7)
Z	4
ρ_{calc} (g cm ⁻³)	1.400
μ (mm ⁻¹)	2.944
F(000)	2328
Data Collection	
T (K)	110(2)
scan mode	ω
hkl range	-13 → +13, -22 → +22, -26 → +26
measd reflns	26547
unique reflns [R _{int}]	8402 [0.0476]
reflns used for refinement	8402
Refinement	
refined parameters	638
Goof	1.035
R1, ^a wR2 ^b all data	0.0483, 0.0952
ρ_{fin} (max/min) (e Å ⁻³)	1.705, -0.544

Based on these structural features, we propose that the high fluoride binding constant measured for **68** results from the higher fluorophilicity of boron when compared to mercury. This greater fluorophilicity leads to a more efficient chelation of the fluoride anion as indicated by the formation of two almost equal B-F bonds in $[\mathbf{68}\text{-}\mu_2\text{-F}]^-$. In order to provide additional support for this interpretation, we computed the fluoride ion affinity (FIA) of the boranes based on a method that we have described earlier.⁸⁵ According to these calculations, the FIA of **68** (75.1 kcal/mol) is greater than that of **69** (68.1 kcal/mol) and **70** (71.5 kcal/mol) which suggest that the higher fluoride binding constant observed for **68** is, at least partly, of enthalpic origin. The FIAs of **69** and **70** are greater than that computed for BPhMes₂ (64.18 kcal/mol)⁸⁵ which indicates that the mercury atom of these heteronuclear Lewis acids is non-innocent and effectively increases their fluoride affinity by interacting with the fluoride anion. In agreement with this view, simple triaryl boranes such as BMe₃ do not bind fluoride in CHCl₃.⁹⁵

5.9 Conclusion

The results presented further document the affinity of naphthalene-based multidendate Lewis acids for fluoride anions. The trinuclear Lewis acid **70** is able to bind two fluoride anions. However, binding of the second fluoride anion is much less favorable than that of the first because of unfavorable Coulombic and steric effects. The comparison of **68**, **69** and **70** indicates that the fluoride binding constant of **70** is comparable to that of simple B/Hg bidentate Lewis acids such as **69** but significantly lower than that of bidentate diboranes such as **68**. From an analytical perspective, this

work indicates that the electrochemical properties of heteronuclear B/Hg derivatives such as **69** and **70** can also be used to signal fluoride binding.

5.10 Experimental

General: Extra care was taken at all times to avoid contact with solid, solution, and airborne particulate mercury compounds. Compounds **68**, **69** and $[\text{Li}(\text{THF})_4][1,8\text{-}\mu\text{-(Mes}_2\text{B)C}_{10}\text{H}_6]$ were prepared according to the reported procedures. $[\text{S}(\text{NMe}_2)_3][\text{Me}_3\text{SiF}_2]$ (TASF) was purchased from Aldrich and used as provided. Chloroform was distilled over CaH_2 ; THF over Na/K amalgam. Air-sensitive compounds were handled under N_2 atmosphere using standard Schlenk and glovebox techniques. UV-vis spectra were recorded on a HP8453 or Ocean Optics USB2000 spectrophotometer. Elemental analyses were performed at Atlantic Microlab (Norcross, GA). NMR spectra were recorded on Inova-400 FT NMR (broadband) (399.63 MHz for ^1H , 376.03 MHz for ^{19}F , 128.22 MHz for ^{11}B , 100.50 MHz for ^{13}C , 75.52 for ^{199}Hg) by using internal deuterium lock. Chemical shifts δ are given in ppm. Spectra are internally referenced to Me_4Si (^1H , ^{13}C , $\delta = 0$ ppm), and externally referenced to $\text{BF}_3\cdot\text{OEt}_2$ (^{11}B , $\delta = 0$ ppm), CFCl_3 (^{19}F , $\delta = 0$ ppm) and HgCl_2 in DMSO (^{199}Hg , $\delta = -1501.6$ ppm).

Crystallography: Single crystals of **70**-0.5(CHCl_3) and **4**-(C_6H_6) were obtained from chloroform and benzene, respectively, upon slow evaporation of the solvent. Colorless single crystals of $[\text{S}(\text{NMe}_2)_3][\text{68-}\mu_2\text{-F}]$ were obtained by vapor diffusion of hexane into a concentrated chloroform solution containing an equimolar amount of **68** and TASF. Single crystals of $[\text{S}(\text{NMe}_2)_3][\text{3-}\mu_2\text{-F}]$ were obtained from a THF solution containing an

equimolar amount of **70** and TASF upon slow evaporation of the solvent. The crystallographic measurements were performed using a Bruker SMART-CCD (for **4** and [S(NMe₂)₃][**1**- μ_2 -F]) or a Bruker APEX-II CCD (for [S(NMe₂)₃][**70**- μ_2 -F]) area detector diffractometer with a graphite-monochromated Mo K α radiation ($\lambda = 0.71073 \text{ \AA}$). The crystallographic measurement for **70**-0.5(CHCl₃) were performed using a Bruker AXS GADDS MWPC area detector diffractometer with a graphite-monochromated Cu K α radiation ($\lambda = 1.54178 \text{ \AA}$). In each case, the crystal was mounted onto a nylon loop with Apiezon grease. The structure was solved by direct methods, which successfully located most of the non-hydrogen atoms. Subsequent refinement on F^2 with the SHELXTL/PC package (version 5.1) allowed location of the remaining non-hydrogen atoms.

Electrochemistry: Electrochemical experiments were performed with an electrochemical analyzer from CH Instruments (Model 610A) with a glassy carbon working electrode and a platinum auxiliary electrode. The reference electrode was built from a silver wire inserted a small glass tube fitted with a porous vycor frit at the tip and filled with a THF solution containing (*n*-Bu)₄NPF₆ (0.1 M) and AgNO₃ (0.005 M). All three electrodes were immersed in a THF solution (2 mL) containing (*n*-Bu)₄NPF₆ (0.3 M) as a supporting electrolyte and the analyte. The electrolyte was dried under vacuum prior to use. In all cases, ferrocene was used as an internal standard, and all reduction potentials are reported with respect to the $E_{1/2}$ of the Fc/Fc⁺ redox couple. The differential pulsed voltammograms of **69** and **70** were recorded in THF (2.5 ml) with a nBu₄NPF₆ (0.3 M) as a supporting electrolyte. For **69**, 2.5 ml of the borane was titrated 5 μ l, 10 μ l, 15 μ l, 20 μ l, 25 μ l, respectively, of a 0.32 M solution of TBAF in THF. For

70, 2.5 ml of the borane was titrated 15 μ l, 30 μ l, 45 μ l, 60 μ l, 75 μ l, 90 μ l, 100 μ l, 125 μ l, 135 μ l respectively, of a 0.14 M solution of TBAF in THF.

Theoretical calculations: DFT calculations (full geometry optimization) were carried out with Gaussian 03¹⁰¹ using the B3LYP functional with the following basis sets: 6-31g for all carbon and hydrogen atoms,¹⁰² 6-31+g(d') for the boron and nitrogen atoms,¹⁰³⁻¹⁰⁵ and Stuttgart RSC 1997 ECP for the mercury centers.¹⁰⁶ Frequency calculations, which were carried out on the optimized structure of each compound, confirmed the absence of imaginary frequencies. Frontier orbitals were obtained from the optimized geometry. In order to calculate the fluoride ion affinity of the boranes, the optimized geometries of the boranes and fluoroborates were subjected to a single point energy calculation using the gradient-corrected B3LYP functional and the 6-311+g(2d,p) basis set for all atoms^{107,108} except for mercury for which the Stuttgart RSC 1997 ECP was used. The fluoride ion affinities were calculated as per equations 1 and 2 (Figure 110).⁸⁵ The reaction enthalpies ΔH were derived from the energy of each molecule (from the single point calculation) and corrected to enthalpy by the “thermal correction to enthalpy term” obtained in the frequency calculations.

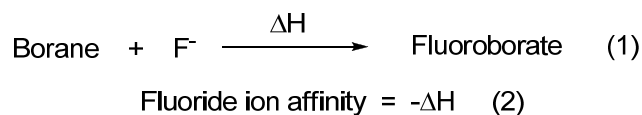


Figure 110. Equations depicting how fluoride ion affinities were calculated.

Synthesis of [1,1'-(Hg)-[8-(Mes₂B)C₁₀H₆]₂] (70): To a solution of [Li(THF)₄][1,8- μ -(Mes₂B)C₁₀H₆] (294 mg, 0.44 mmol) in THF (3 mL) was added a solution of mercury dichloride (60 mg, 0.22 mmol) in THF (2 mL) at -40 °C. The resulting mixture was stirred at room temperature for 18 hrs. During this time, the compound precipitated. It was isolated by filtration after cooling the reaction mixture in an ice bath. Further washing with two 1 mL portions of ice cold THF followed by drying dried in vacuo afforded compound in a 70% yield (146 mg). m.p.305°C (dec.). This compound could be further purified by recrystallization from a concentrated chloroform solution from which it crystallizes with half a molecule of interstitial chloroform. Elemental analysis of a dry sample indicated partial loss of the interstitial solvent. Anal. (found) for C₅₆H₅₆B₂Hg·0.22(CHCl₃): C, 69.08 (69.08); H, 5.80 (5.75). ¹H NMR (CDCl₃): δ 0.90-1.85 (sh 1.10) (br s, 24H, *o*-CH₃), 2.26 (s, 12H, *p*-CH₃), 6.42 (br s, 2H, naph-C(2)-H), 6.60 (br s, 8H, Mes-C-H), 7.26-7.35 (m, 4H, naph-C(3,6)-H), 7.43 (d, 2H, naph-C(4/5/7)-H), 7.69 (d, 2H, naph-C(4/5/7)-H), 7.89 (d, 2H, naph-C(4/5/7)-H). ¹¹B (CDCl₃): δ 72. ¹⁹⁹Hg (CDCl₃): δ -800.

CHAPTER VI

SUMMARY

6.1 Synthesis of compounds displaying unusual bonding

The first part of this dissertation focused on the study of compounds featuring unusual bridging interactions. More specifically, we set out to determine if fluorosilane Lewis acids could form σ -complexes with alkanes. In order to probe this possibility, we have synthesized the cationic fluorosilane **[26]**⁺ as a tetrafluoroborate salt and converted it into **27** by reaction with NaBH₄ (Figure 111, Figure 112). Both **[26]**[BF₄] and **27** have been fully characterized. Examination of the structure of **27** indicates the presence of an interaction involving the C-H bond at the 9-position of the xanthene unit and the silicon atom. This interaction, which is characterized by a Si-H separation of 2.32(2) Å and a F-Si-H angle of 177.0(5)°, leads the silicon atom to adopt a distorted trigonal bipyramidal geometry. The nature of this interaction has been investigated experimentally by NMR and IR spectroscopy as well as computationally using density functional calculations, Atom In Molecules and Natural Bond Order analyses. These combined experimental and computational results suggest that the short Si-H contact in **27** corresponds to an agostic C-H→Si interaction.

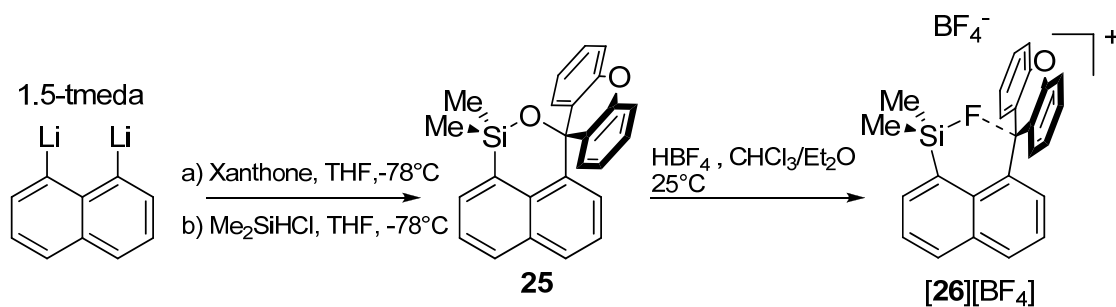


Figure 111. Synthesis of **[26][BF₄]**

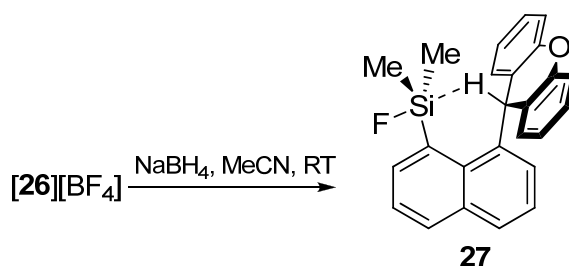


Figure 112. Synthesis of **27**

When fluoride is added to an acetonitrile solution of **[26][BF₄]**, presumably Me_2SiF_2 is liberated affording **30** as the main product (Figure 113). Though the solid state structure of this compound has not been determined, the formation of a peri-bridged naphthalene species is consistent with the ^1H NMR splitting pattern and the instability of **30** towards moisture and air. This instability indicates that **30** might also be useful for the synthesis of other unsymmetrical derivatives.

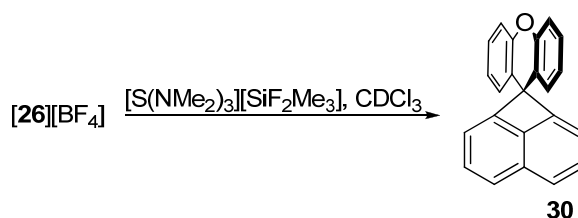


Figure 113. Synthesis of **30**.

6.2 Fluoride anion complexation by a B₂/Hg heteronuclear tridentate Lewis acid

The reaction of $[Li(THF)_4][1,8-\mu-(Mes_2B)C_{10}H_6]$ with $HgCl_2$ affords $[1,1'-(Hg)-[8-(Mes_2B)C_{10}H_6]_2]$ (**70**). This new compound has been fully characterized. The cyclic voltammogram of **70** in THF shows two distinct waves observed at $E_{1/2}$ -2.31 V and -2.61 V, corresponding to the sequential reductions of the two boron centers. Fluoride titration experiments monitored by electrochemistry suggest that **70** binds tightly to one fluoride anion and more loosely to a second one (Figure 114). These conclusions have been confirmed by a UV-vis titration experiment which indicates that the first fluoride binding constant (K_1) is greater than $10^8 M^{-1}$ while the second (K_2) equals $5.2 (0.4) 10^3 M^{-1}$. The fluoride binding properties of **70** have been compared to those of **68** and **69**. Both experimental and computational results indicate that its affinity for fluoride anions is comparable to that of **69** but significantly lower than that of the diborane **68**. In particular, the fluoride binding constants of **68**, **69** and **70** in chloroform are respectively equal to $5.0 (\pm 0.2) \times 10^5 M^{-1}$, $1.0 (\pm 0.2) \times 10^3 M^{-1}$ and $1.7 (\pm 0.1) \times 10^3 M^{-1}$. Determination of the crystal structures of the fluoride adducts $[S(NMe_2)_3][68-\mu_2-F]$ and $[S(NMe_2)_3][3-\mu_2-F]$ along with computational results indicate that higher fluoride

binding constant of **68** arises from a strong chelate effect involving two fluorophilic boron centers.

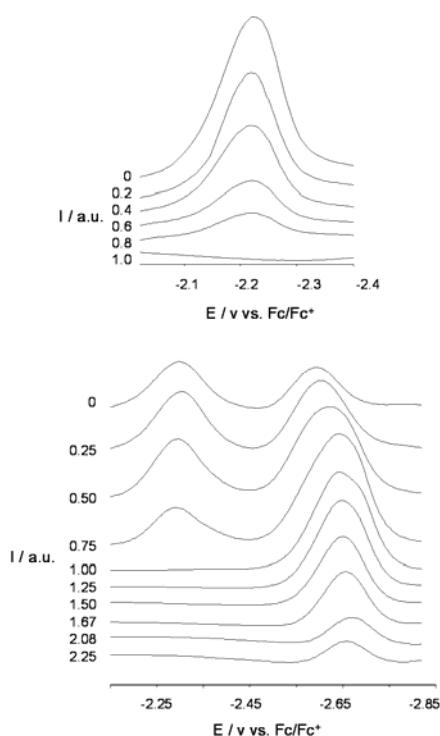


Figure 114. Changes in the differential pulsed voltammogram of **69** (top) and **70** (bottom) observed upon the addition of $n\text{Bu}_4\text{NF}$ to a THF solution (0.3 M).

6.3 Synthesis and redox properties of borata-alkenes

Reaction of 4-(lithiophenyl)dimesityl borane with xanthone and N-methylacridone affords salts **[39]** $[\text{BF}_4]$ and **[40]** $[\text{BF}_4]$ respectively. These salts have been fully characterized. Comparison of the first reduction potentials of these cationic boranes ($E_{1/2} = -0.386$ V for **[39]** $^+$ in CH_2Cl_2 and -0.99 V for **[40]** $^+$ in THF) with those of their

non-borylated counterparts ($E_{1/2} = -0.47$ V for phenylxanthenium and -0.86 V for phenylacridinium) reveals that the boryl substituent has little effect. In agreement with this view, calculations and EPR measurements carried out on **39'** show that there is little delocalization of the radical on the extended phenylene linker and onto the boron center. This can be attributed to the inability of the carbocationic moiety to become co-planar with the phenylene ring and effect conjugation throughout the system.

6.4 Synthesis and redox properties of α -phosphonio and α -phosphonyl carbocations

In an effort to further explore the redox properties of phosphorus ylids, the dicationic $[50]^{2+}$, $[51]^{2+}$ and $[52]^{2+}$ were synthesized. Reduction of $[50]^{2+}$ with one equivalent of Na/Hg produces a dark green solution of $[50]^{+\bullet}$ which is stable for extended periods of time. EPR of this solution shows a predominately acridine based radical with 18 G coupling to the ^{31}P center (Figure 115).

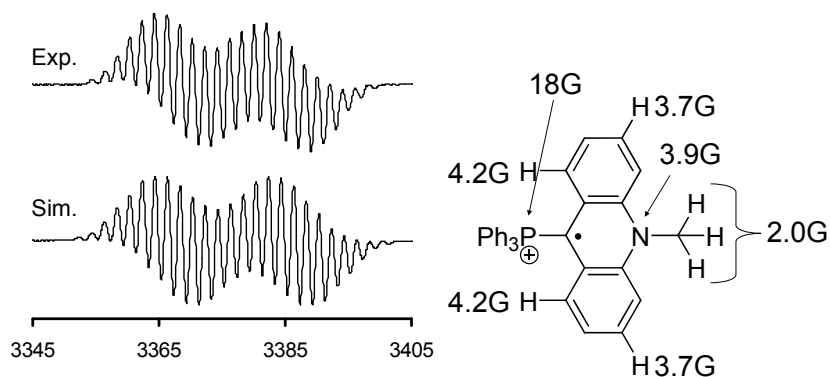


Figure 115. Experimental and simulated EPR spectra of $[50]^{2+}$ (left) and hyperfine coupling parameters (right)

Furthermore, ligand exchange reactions of dication $[50]^{2+}$ with neutral pyridines affords the new dications $[53]^{2+}$ and $[54]^{2+}$ suggesting that they can be viewed as a ligand stabilized carbocations (Figure 116).

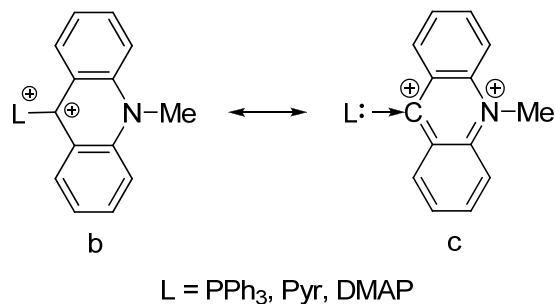


Figure 116. Representations of forms **b** and **c** of ligand stabilized carbocations

Additionally, the α -phosphonyl carbocation $[56]^+$ has been synthesized and fully characterized. The solid state structure reveals a planar acridinium moiety with a pendant diethylphosphonic ester functionality. Reduction of $[56]^+$ with Mg in a CH₃CN/hexane biphasic mixture produces a dark red hexane solution of **56'** which is persistent for several days. EPR spectroscopy of the resulting hexane solution again reveals an acridine based radical with 19.7 G coupling to the phosphorus center (Figure 117).

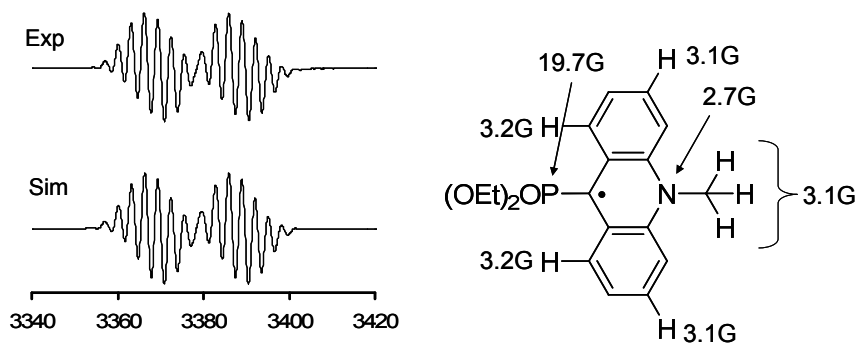


Figure 117. Experimental and simulated EPR spectra of [56]⁺ (left) and hyperfine coupling parameters (right)

6.5 Conclusion

The research presented in this dissertation primarily focused on the synthesis, characterization, structures and electrochemistry of electron deficient neutral and cationic hybrid Lewis acid systems. Synthesis and structural characterization of the first example of a $R_3C-H \rightarrow SiFR_3$ agostic interaction has been reported. Following anion binding by main group Lewis acids through the use of electrochemical methods has been achieved. Finally, the first examples of systems which can be regarded as ligand stabilized carbocations have been fully characterized, and new boron and phosphorus containing radical systems have been shown to be stable and persistent. In the future, it could be of great interest to study the reaction of **[26]** $[BF_4]$ with fluoride and isolate the putative species **30**. If the proposed structure of this product is correct, it could prove very useful in synthesizing hybrid species which prove to be elusive using the current methods.

Also, the surface has only been scratched with regard to phosphorus containing radicals. By changing the carbon side of the molecule, it might be possible to stabilize the ylid and therefore isolate the entire series of redox states to gain a better understanding of the structural changes of these derivatives in different redox states.

REFERENCES

1. Katz, H. E. *J. Org. Chem.* **1985**, *50*, 5027-5032.
2. Katz, H. E. *J. Am. Chem. Soc.* **1986**, *108*, 7640-7645.
3. Solé, S.; Gabbaï, F. P. *Chem. Commun.* **2004**, 1284-1285.
4. Gabbaï, F. P. *Angew. Chem. Int. Ed.* **2003**, *42*, 2218-2221.
5. Hoefelmeyer, J. D.; Schulte, M.; Tschinkl, M.; Gabbaï, F. P. *Coord. Chem. Rev.* **2002**, *235*, 93-103.
6. Wang, H.; Webster, C. E.; Perez, L. M.; Hall, M. B.; Gabbaï, F. P. *J. Am. Chem. Soc.* **2004**, *126*, 8189-8196.
7. McMurry, J. E.; Lectka, T. *Acc. Chem. Res.* **1992**, *25*, 47-53.
8. McMurry, J. E.; Lectka, T.; Hodge, C. N. *J. Am. Chem. Soc.* **1989**, *111*, 8867-8872.
9. Kawai, H.; Nagasu, T.; Takeda, T.; Fujiwara, K.; Tsuji, T.; Ohkita, M.; Nishida, J.-i.; Suzuki, T. *Tetrahedron Lett.* **2004**, *45*, 4553-4558.
10. Kawai, H.; Takeda, T.; Fujiwara, K.; Suzuki, T. *J. Am. Chem. Soc.* **2005**, *127*, 12172-12173.
11. Wang, H.; Sole, S.; Gabbaï, F. P. *ACS Symp. Ser.* **2006**, *917*, 208-220.
12. Panisch, R.; Bolte, M.; Müller, T. *J. Am. Chem. Soc.* **2006**, *128*, 9676-9682.
13. Melaïmi, M.; Solé, S.; Chiu, C.-W.; Wang, H.; Gabbaï, F. P. *Inorg. Chem.* **2006**, *in press*.
14. Power, P. P. *Chem. Rev.* **2003**, *103*, 789-809.
15. Krause, E.; Polack, H. *Berichte Der Deutschen Chemischen Gesellschaft* **1926**, *59*, 777-785.
16. Chu, T. L.; Weissmann, T. J. *J. Am. Chem. Soc.* **1956**, *78*, 23-26.
17. Weissman, S. I.; van Willigen, H. *J. Am. Chem. Soc.* **1965**, *87*, 2285-2286.

18. Leffler, J. E.; Watts, G. B.; Tanigaki, T.; Dolan, E.; Miller, D. S. *J. Am. Chem. Soc.* **1970**, *92*, 6825-6830.
19. Olmstead, M. M.; Power, P. P. *J. Am. Chem. Soc.* **1986**, *108*, 4235-4236.
20. Eisch, J. J.; Dluzniewski, T.; Behrooz, M. *Heteroat. Chem* **1993**, *4*, 235-241.
21. Kwaan, R. J.; Harlan, C. J.; Norton, J. R. *Organometallics* **2001**, *20*, 3818-3820.
22. Cummings, S. A.; Iimura, M.; Harlan, C. J.; Kwaan, R. J.; Trieu, I. V.; Norton, J. R.; Bridgewater, B. M.; Jäkle, F.; Sundararaman, A.; Tilset, M. *Organometallics* **2006**, *25*, 1565-1568.
23. Venkatasubbaiah, K.; Zakharov, L. N.; Kassel, W. S.; Rheingold, A. L.; Jäkle, F. *Angew. Chem. Int. Ed.* **2005**, *44*, 5428-5433.
24. Mueller, P.; Huck, S.; Koepfel, H.; Pritzkow, H.; Siebert, W. *Zeitschrift fuer Naturforschung, B: Chemical Sciences* **1995**, *50*, 1476-84.
25. Brown, H. C.; Dodson, V. H. *J. Am. Chem. Soc.* **1957**, *79*, 2302-2306.
26. Elschenbroich, C.; Kuehlkamp, P.; Behrendt, A.; Harms, K. *Chem. Ber.* **1996**, *129*, 859-869.
27. Klusik, H.; Berndt, A.; Huenig, S. *Angew. Chem. Int. Ed.* **1981**, *20*, 870-871.
28. Grigsby, W. J.; Power, P. *Chem. Eur. J.* **1997**, *3*, 368-375.
29. Grigsby, W. J.; Power, P. P. *Chem. Commun.* **1996**, 2235-2236.
30. Moezzi, A.; Olmstead, M. M.; Power, P. P. *J. Am. Chem. Soc.* **1992**, *114*, 2715-17.
31. Hoefelmeyer, J. D.; Gabbai, F. P. *J. Am. Chem. Soc.* **2000**, *122*, 9054-9055.
32. Hoefelmeyer, J. D.; Solé, S.; Gabbai, F. P. *Dalton Trans.* **2004**, 1254-1258.
33. Chiu, C.-W.; Gabbai, F. P. *Angew. Chem. Int. Ed.* **2007**, *46*, 1723-1725.
34. Chiu, C.-W.; Gabbai, F. P. *Angew. Chem. Int. Ed.* **2007**, *46*, 6878-6881.
35. Wienk, M. M.; Janssen, R. A. J. *J. Am. Chem. Soc.* **1997**, *119*, 5398-5403.

36. Van Dijk, J. M. F.; Pennings, J. F. M.; Buck, H. M. *J. Am. Chem. Soc.* **1975**, *97*, 4836-9.
37. Buck, H. M.; Huizer, A. H.; Oldenburg, S. J.; Schipper, P. *Phosphorus and the Related Group V Elements* **1971**, *1*, 97-9.
38. Buck, H. M.; Huizer, A. H.; Oldenburg, S. J.; Schipper, P. *Recl. Trav. Chim. Pays-Bas* **1970**, *89*, 1085-8.
39. Tumanskii, B.; Sheberla, D.; Molev, G.; Apeloig, Y. *Angew. Chem. Int. Ed.* **2007**, *46*, 7408-7411.
40. Chiu, C.-W.; Gabbai, F. P. *Angew. Chem. Int. Ed.* **2007**, *46*, 6878-6881.
41. Power, P. P. *Inorg. Chim. Acta* **1992**, *198-200*, 443-7.
42. Porter, W. W., III; Vaid, T. P. *J. Org. Chem.* **2005**, *70*, 5028-5035.
43. Rathore, R.; Lindeman, S. V.; Kumar, A. S.; Kochi, J. K. *J. Am. Chem. Soc.* **1998**, *120*, 6931-6939.
44. Takeda, T.; Kawai, H.; Fujiwara, K.; Suzuki, T. *Chem. Eur. J.* **2007**, *13*, 7915-7925.
45. Khalimon, A. Y.; Lin, Z. H.; Simionescu, R.; Vyboishchikov, S. F.; Nikonov, G. I. *Angew. Chem. Int. Ed.* **2007**, *46*, 4530-4533.
46. Ebata, K.; Inada, T.; Kabuto, C.; Sakurai, H. *J. Am. Chem. Soc.* **1994**, *116*, 3595-3596.
47. Tamao, K.; Hayashi, T.; Ito, Y.; Shiro, M. *Organometallics* **1992**, *11*, 2099-114.
48. Tamao, K.; Hayashi, T.; Ito, Y. *J. Organomet. Chem.* **1996**, *506*, 85-91.
49. Katz, H. E. *Organometallics* **1986**, *5*, 2308-2311.
50. Kawachi, A.; Zaima, M.; Yamamoto, Y. *Organometallics* **2008**, *27*, 4691-4696.
51. Kawachi, A.; Tani, A.; Shimada, J.; Yamamoto, Y. *J. Am. Chem. Soc.* **2008**, *130*, 4222-4223.
52. Letsinger, R. L.; Gilpin, J. A.; Vullo, W. J. *J. Org. Chem.* **1962**, *27*, 672-4.
53. Chiu, C.-W.; Gabbai, F. P. *J. Am. Chem. Soc.* **2006**, *128*, 14248-14249.

54. Neugebauer, W.; Clark, T.; Schleyer, P. v. R. *Chem. Ber.* **1983**, *116*, 3283-92.
55. Akkari-El Ahdab, A.; Rima, G.; Gornitzka, H.; Barrau, J. *J. Organomet. Chem.* **2001**, *636*, 96-107.
56. Nyburg, S. C.; Faerman, C. H. *Acta Crystallograph., Sect. B* **1985**, *B41*, 274-9.
57. Caillet, J.; Claverie, P. *Acta Crystallograph., Sect. A* **1975**, *31*, 448-461.
58. Grobe, J.; Martin, R.; Krebs, B.; Henkel, G. *Z. Anorg. Allg. Chem.* **1992**, *607*, 131-138.
59. Breliere, C.; Corriu, R. J. P.; Royo, G.; Zwecker, J. *Organometallics* **1989**, *8*, 1834-1836.
60. Gountchev, T. I.; Tilley, T. D. *J. Am. Chem. Soc.* **1997**, *119*, 12831-12841.
61. Kim, K.-C.; Reed, C. A.; Elliott, D. W.; Mueller, L. J.; Tham, F.; Lin, L.; Lambert, J. B. *Science* **2002**, *297*, 825-827.
62. Hoffmann, S. P.; Kato, T.; Tham, F. S.; Reed, C. A. *Chem. Commun.* **2006**, 767-769.
63. Sekiguchi, A.; Murakami, Y.; Fukaya, N.; Kabe, Y. *Chem. Lett.* **2004**, *33*, 530-531.
64. Müller, T. *Angew. Chem. Int. Ed.* **2001**, *40*, 3033-3036.
65. Nikonov, G. I.; Kuzmina, L. G.; Lemenovskii, D. A.; Kotov, V. V. *J. Am. Chem. Soc.* **1995**, *117*, 10133-10134.
66. Schubert, U.; Ackermann, K.; Woerle, B. *J. Am. Chem. Soc.* **1982**, *104*, 7378-7380.
67. Nikonov, G. I. *Adv. Organomet. Chem.* **2005**, *53*, 217-309.
68. Xie, Z.; Bau, R.; Benesi, A.; Reed, C. A. *Organometallics* **1995**, *14*, 3933-41.
69. Scherer, W.; McGrady, G. S. *Angew. Chem. Int. Ed.* **2004**, *43*, 1782-1806.
70. Vorobyov, I.; Yappert, M. C.; DuPre, D. B. *J. Phys. Chem. A* **2002**, *106*, 668-679.
71. Adam, F. C.; Weissman, S. I. *J. Am. Chem. Soc.* **1958**, *80*, 2057-2059.

72. Martin, K.; George, K. F. *J. Chem. Phys.* **1961**, *35*, 1312-1323.
73. Kaim, W.; Schulz, A. *Angew. Chem. Int. Ed.* **1984**, *23*, 615-616.
74. Bartlett, R. A.; Power, P. P. *Organometallics* **1986**, *5*, 1916-17.
75. Olmstead, M. M.; Power, P. P.; Weese, K. J.; Doedens, R. J. *J. Am. Chem. Soc.* **1987**, *109*, 2541-2.
76. Chiu, C.-W.; Gabbai, F. P. *Angew. Chem. Int. Ed.* **2007**, *46*, 1723-1725.
77. Kaim, W.; Lechner-Knoblauch, U.; Haenel, P.; Bock, H. *J. Org. Chem.* **1983**, *48*, 4206-9.
78. Salvador Conejero, M. S. D. M. Y. C. M. S. G. B. *Chemistry - An Asian Journal* **2006**, *1*, 155-160.
79. Ahlberg, E.; Hammerich, O.; Parker, V. D. *J. Am. Chem. Soc.* **1981**, *103*, 844-9.
80. Katz, H. E. *J. Am. Chem. Soc.* **1985**, *107*, 1420-1421.
81. Chase, P. A.; Henderson, L. D.; Piers, W. E.; Parvez, M.; Clegg, W.; Elsegood, M. R. *J. Organometallics* **2006**, *25*, 349-357.
82. Lewis, S. P.; Taylor, N. J.; Piers, W. E.; Collins, S. *J. Am. Chem. Soc.* **2003**, *125*, 14686-14687.
83. Chai, J.; Lewis, S. P.; Collins, S.; Sciarone, T. J. J.; Henderson, L. D.; Chase, P. A.; Irvine, G. J.; Piers, W. E.; Elsegood, M. R. J.; Clegg, W. *Organometallics* **2007**, *26*, 5667-5679.
84. Henderson, L. D.; Piers, W. E.; Irvine, G. J.; McDonald, R. *Organometallics* **2002**, *21*, 340-345.
85. Melaïmi, M.; Sole, S.; Chiu, C.-W.; Wang, H.; Gabbai, F. P. *Inorg. Chem.* **2006**, *45*, 8136-8143.
86. Haneline, M. R.; Tsunoda, M.; Gabbai, F. P. *J. Am. Chem. Soc.* **2002**, *124*, 3737-3742.
87. Melaïmi, M.; Gabbai, F. P. *J. Am. Chem. Soc.* **2005**, *127*, 9680-9681.
88. Lee, M. H.; Gabbai, F. P. *Inorg. Chem.* **2007**, *46*, 8132-8138.

89. Hoefelmeyer, J. D.; Gabbai, F. P. *Organometallics* **2002**, *21*, 982-985.
90. Gabbai, F. P.; Schier, A.; Riede, J. *Chem. Commun.* **1996**, 1121-1122.
91. Kennedy, J. D.; McFarlane, W. *J. Chem. Soc., Far. Trans. 2: Molecular and Chemical Physics* **1976**, *72*, 1653-60.
92. Haneline, M. R.; Taylor, R. E.; Gabbai, F. P. *Chemistry - A European Journal* **2003**, *9*, 5189-5193.
93. Taylor, T. J.; Burrell, C. N.; Gabbai, F. P. *Organometallics* **2007**, *26*, 5252-5263.
94. Mulliken, R. S. *Chem. Rev.* **1947**, *41*, 207-17.
95. Lee, M. H.; Agou, T.; Kobayashi, J.; Kawashima, T.; Gabbai, F. P. *Chem. Commun.* **2007**, 1133-1135.
96. Yamaguchi, S.; Akiyama, S.; Tamao, K. *J. Am. Chem. Soc.* **2001**, *123*, 11372-11375.
97. Hudnall, T. W.; Gabbai, F. P. *J. Am. Chem. Soc.* **2007**, *129*, 11978-11986.
98. Pyykkö, P.; Straka, M. *PCCP* **2000**, *2*, 2489-2493.
99. Bayer, M. J.; Jalilati, S. S.; Smart, B.; Herzog, A.; Knobler, C. B.; Hawthorne, M. F. *Angew. Chem. Int. Ed.* **2004**, *43*, 1854-1857.
100. Viets, D.; Lork, E.; Watson, P. G.; Mews, R. *Angew. Chem. Int. Ed.* **1997**, *36*, 623-624.

101. Gaussian 03, Revision C.02, M. J. Frisch, G. W. Trucks, H. B. Schlegel, G. E. Scuseria, M. A. Robb, J. R. Cheeseman, J. A. Montgomery, Jr., T. Vreven, K. N. Kudin, J. C. Burant, J. M. Millam, S. S. Iyengar, J. Tomasi, V. Barone, B. Mennucci, M. Cossi, G. Scalmani, N. Rega, G. A. Petersson, H. Nakatsuji, M. Hada, M. Ehara, K. Toyota, R. Fukuda, J. Hasegawa, M. Ishida, T. Nakajima, Y. Honda, O. Kitao, H. Nakai, M. Klene, X. Li, J. E. Knox, H. P. Hratchian, J. B. Cross, V. Bakken, C. Adamo, J. Jaramillo, R. Gomperts, R. E. Stratmann, O. Yazyev, A. J. Austin, R. Cammi, C. Pomelli, J. W. Ochterski, P. Y. Ayala, K. Morokuma, G. A. Voth, P. Salvador, J. J. Dannenberg, V. G. Zakrzewski, S. Dapprich, A. D. Daniels, M. C. Strain, O. Farkas, D. K. Malick, A. D. Rabuck, K. Raghavachari, J. B. Foresman, J. V. Ortiz, Q. Cui, A. G. Baboul, S. Clifford, J. Cioslowski, B. B. Stefanov, G. Liu, A. Liashenko, P. Piskorz, I. Komaromi, R. L. Martin, D. J. Fox, T. Keith, M. A. Al-Laham, C. Y. Peng, A. Nanayakkara, M. Challacombe, P. M. W. Gill, B. Johnson, W. Chen, M. W. Wong, C. Gonzalez, and J. A. Pople, Gaussian, Inc., Wallingford CT, 2004.
102. Hehre, W. J.; Ditchfield, R.; Pople, J. A. *J. Chem. Phys.* **1972**, *56*, 2257-2261.
103. Clark, T.; Chandrasekhar, J.; Spitznagel, G. W.; Schleyer, P. v. R. *J. Comput. Chem.* **1983**, *4*, 294-301.
104. Krishnan, R.; Binkley, J. S.; Seeger, R.; Pople, J. A. *J. Chem. Phys.* **1980**, *72*, 650-654.
105. Gill, P. M. W.; Johnson, B. G.; Pople, J. A.; Frisch, M. J. *Chem. Phys. Lett.* **1992**, *197*, 499-505.
106. Dunning, T. H. J.; Hay, P. J. *Modern Theoretical Chemistry*; Plenum: New York 1976; Vol. 3.
107. Krishnan, R.; Binkley, J. S.; Seeger, R.; Pople, J. A. *J. Chem. Phys.* **1980**, *72*, 650-4.
108. Spitznagel, G. W.; Clark, T.; Schleyer, P. v. R.; Hehre, W. J. *J. Comput. Chem.* **1987**, *8*, 1109-16.

VITA

Christopher Lane Dorsey
Born in Houston, Texas

c/o Prof. François Gabbai
Department of Chemistry
Texas A&M University
College Station, Texas 77843-3255

Education:

Ph.D. in Chemistry from Texas A&M University; Graduated: May 2009
B.S. in Chemistry from Texas Lutheran University; Graduated: May 2004

Awards:

Martin Corera Travel Award, Texas A&M University, August 2007
A. E. Martell Travel Award, Texas A&M University, March 2008

Publications:

Dorsey, C. L., Gabbai, F. P., "A $R_3C-H \rightarrow SiFR_3$ Agostic Interaction," *Organometallics*, **2008**, *27*, 3065-3069.

Dorsey, C. L.; Jewula, P.; Hudnall, T. W.; Hoefelmeyer, J. D.; Taylor, T. J.; Honesy, N.; Chiu, C-W.; Schulte, M.; Gabbai, F. P., "Fluoride Ion Complexation by a B_2/Hg Heteronuclear Tridentate Lewis Acid – A Structural and Electrochemical Investigation," *Dalton Trans.*, **2008**, *33*, 4442-4450.